University of Central Florida

STARS

Electronic Theses and Dissertations, 2004-2019

2011

Process-dependent Microstructure And Severe Plastic Deformation In Sicp?? Reinforced Aluminum Metal Matrix Composites

Catalina Uribe-Restrepo

University of Central Florida

Part of the Materials Science and Engineering Commons

Find similar works at: https://stars.library.ucf.edu/etd

University of Central Florida Libraries http://library.ucf.edu

This Masters Thesis (Open Access) is brought to you for free and open access by STARS. It has been accepted for inclusion in Electronic Theses and Dissertations, 2004-2019 by an authorized administrator of STARS. For more information, please contact STARS@ucf.edu.

STARS Citation

Uribe-Restrepo, Catalina, "Process-dependent Microstructure And Severe Plastic Deformation In Sicp?? Reinforced Aluminum Metal Matrix Composites" (2011). *Electronic Theses and Dissertations, 2004-2019*. 1719.

https://stars.library.ucf.edu/etd/1719

PROCESS-DEPENDENT MICROSTRUCTURE AND SEVERE PLASTIC DEFORMATION IN SIC$_P$ REINFORCED ALUMINUM METAL MATRIX COMPOSITES

by

CATALINA URIBE-RESTREPO
B.S., National University of Colombia, 2006

A thesis submitted in partial fulfillment of the requirements
for the degree of Master of Science
in the Department of Mechanical, Materials and Aerospace Engineering
in the College of Engineering and Computer Science
at the University of Central Florida
Orlando, FL

Fall Term
2011

© 2011 Catalina Uribe-Restrepo

ABSTRACT

Discontinuously reinforced MMCs with optimized microstructure are sought after for exceptional high strain rate behavior. The microstructure evolution of a stir-cast A359 aluminum composite reinforced with 30 vol.% SiC_p after isothermal anneal, successive hot-rolling, and high strain rate deformation has been investigated. Quantitative microstructural analysis was carried out for the as-cast, annealed (470°C, 538°C and 570°C) and successively hot rolled specimens (64, 75, 88, and 96% rolling reductions). Selected composites were also examined after high strain rate deformation. X-ray diffraction, optical microscopy, scanning electron microscopy and transmission electron microscopy were employed for microstructural characterization.

The strength and ductility of the A359 Al alloys, and the composite, were greatly influenced by the brittle eutectic silicon phase and its morphology. Lamellar eutectic silicon spheroidized with isothermal anneal and successive hot rolling with a corresponding decrease in hardness. The hot rolling process also considerably decreased the SiC particle size (approximately 20% after 96% reduction) by breaking-up the hard SiC particles. However, this break-up of particles increased the homogeneity of SiC_p size distribution. Successive hot rolling also healed voids due to solidification shrinkage, incomplete infiltration of molten Al and defects originating from fractured particles.

Four selected specimens of composites were examined after high strain rate deformation. Fractography and metallographic analysis for the craters, voids, and relevant regions affected by the high velocity impact were carried out. The deposition of impact residuals was frequently

observed on the exposed fracture surfaces. These residuals were typically observed as "molten-and-solidified" as a consequence of excessive heat generated during and after the damage. Particularly in regions of entry and exit of impact, intermixing of residuals and composite constituents were observed, demonstrating that the Al matrix of the composite also had melted.

In all samples examined, cracks were observed to propagate through the eutectic Si network while a small number of broken reinforcement particles were observed. A slight variation in failure mechanisms was observed (e.g., radial, fragmentation, petalling) corresponding to the variation in ductility against high strain rate deformation. In selected specimens, parallel sub-cracks at the exit were observed at 45° and 30°. These sub-cracks were again filled with intermixed constituents from projectile residuals and composites. This observation suggests that the melting of composite constituents that leads to intermixing occured after the crack propagation and other damage.

I dedicate this dissertation to my family and the people that in some way or another inspired me and gave me the courage to complete this journey. To my husband, Dr. Oscar Martinez, for all his love, patience, and words of encouragement. Finally to my advisor, Dr. Yong-ho Sohn who gave me the opportunity of being part of his team.

ACKNOWLEDGMENTS

I would like to express my gratitude to my advisor, Dr. Yong-ho Sohn for his technical support, assistance and patience. I must acknowledge many friends and colleagues who assisted, advised and supported my research. Especially, I need to express my gratitude and deep appreciation to Travis Patterson whose advice and knowledge have supported this effort. Finally, I want to acknowledge the support provided by U.S. Army Research Laboratory and MC-21 Inc.

TABLE OF CONTENTS

LIST OF FIGURES

LIST OF TABLES

LIST OF ABBREVIATIONS

Al_2O_{3p}	Aluminum Oxide Particle
EDS/EDX	Energy Dispersive X-Ray Spectroscopy
fcc	Faced Center Cubic
FIB	Focused Ion Beam
HV	Vickers Hardness
ID	Specimen Identification
MMC	Metallic Matrix Composite
MMCp	Particulate Metallic Matrix Composite
SEM	Scanning Electron Microscope
SiCp	Silicon Carbide Particle
STEM	Scanning Transmission Electron Microscope
TEM	Transmission electron microscopy
XEDS	X-ray energy dispersive spectroscopy
XRD	X-ray diffraction

CHAPTER 1: INTRODUCTION

Ceramic particulate reinforced metal matrix composites (MMCs) have been developed and applied in numerous industrial applications. MMCs have been used in applications where high strain rate impact properties, high specific strength, high stiffness, high resistance to impacts, and superior fatigue resistance are required with reduced weight. Due to improvement in wear resistance, strength, stiffness, hardness, and chemical compatibility with aluminum, SiCp is considered an ideal reinforcement candidate.

A significant reduction of the ductility and fracture toughness of the MMCs due to the incorporation of the ceramic SiCp has been reported by Samuel (1993). This reduction in toughness is attributed (Samuel, 1993 and Wang, 1996) to the inhomogeneous distribution of the SiC particles, presence of voids after solidification and weak interfacial bonding between the ceramic particles and aluminium matrix. Thermomechanical processing and heat treatments could be applied after casting in order to improve strength and ductility.

Thermomechanical processing, such as hot rolling, enhance void closure and welding; at high rolling temperatures, the voids complete closure quickly. The explanation given by Wang, A. *et al.* (1996) to the faster closure of voids is that temperature increases the diffusion rates and decreases the flow stress of the metal matrix, making the contact of the surface of the voids more effective. Consequently there is a higher diffusional flux between the contacting surfaces. Due to this faster diffusion, it is possible to have a collapse and closure of the voids followed by a welding of the surface of the voids. Unwelded voids behave like sharp cracks, which is detrimental to the performance of the material. On the other hand, particle break up could be present after rolling (Taha *et al*, 2003). Application of successive hot rolling results in a more uniform particle size distribution and homogeneity within the aluminum matrix. Taha *et al* (2003) reported how after particles break up, the ductile aluminium matrix is able to flow between the particles, redistributing the SiCp in a more homogeneous configuration. The evolution of SiC particles size and distribution, as well as the voids closure must be understood to optimize the processing parameters that yield the properties suitable for various applications.

Additionally, since mechanical properties of Al-Si alloys present a linear dependence on the volume fraction of silicon (Warmuzek, 2004) and a dependence on its morphology, it is important to understand the mechanisms of eutectic Si formation and its evolution with hot rolling, annealing, and high strain rate deformation.

The objective of this research was to examine and characterize the composition, process-dependent microstructure, and severe plastic deformation caused by high velocity impacts, that resulted in complete and partial damage to SiC_p or Al_2O_{3p} reinforced Al MMCs. Tools of materials characterization included optical microscopy, scanning electron microscopy (SEM), transmission electron microscopy (TEM) and scanning TEM (STEM) along with relevant spectroscopic analyses. Efforts in microstructure and spectroscopy analysis ranged from visual to sub-nanometer scale. Results from this study include size, shape and constituents of matrix and precipitate phases, SiC_p or Al_2O_{3p} size and distribution, and relevant interfacial features as a function of successive hot-rolling. Furthermore, failure characteristics due to severe plastic deformation caused by projectiles were characterized. Findings from this study will help design composites (e.g., composition, process, and microstructure) with superior deformation resistance against high strain rate and ease of fabrication.

CHAPTER 2: LITERATURE REVIEW

2.1. Metallic Matrix Composites

MMCs are designed materials composed of ceramic reinforcement (discrete constituent) distributed in a metallic matrix (continuous phase). These constituents have significantly different chemical, physical, and mechanical properties. MMCs derive their unique characteristics from the properties of their main components and from their interfaces.

Properties of the MMCs can be customized by changing the properties of the main components and their volume fraction. Composition, size, shape, distribution of the reinforcement, and volume fraction are key factors contributing to the final characteristics of the MMCs. These characteristics can be designed in the material and tailored depending on the specific application.

The reinforcement in MMCs have different objectives depending on the desired properties. The reinforcement for light metallic alloys such as aluminum yields to the applications where the first priority is weight reduction.

Figure 1 shows the properties of the MMCs obtained by combination of metal and ceramic properties.

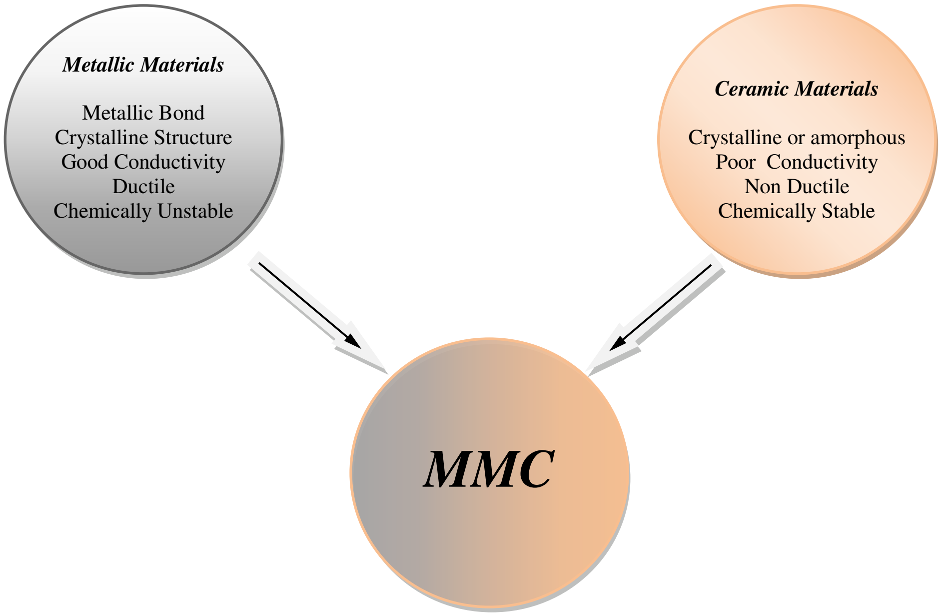

Figure 1. Properties of the composed materials.

The advantages of using metallic matrix composite materials compared to unreinforced materials are:

- Greater strength: Increased yield strength and tensile strength.
- Improved high temperature properties, creep resistance and fatigue strength at higher temperatures.
- Improved stiffness.
- Reduced density(weight).
- Controlled thermal expansion coefficient.
- Improved electrical performance.
- Improved thermal resistance properties.
- Improved wear and abrasion resistance.
- Improved corrosion resistance.

MMCs with different types of reinforcements such as whiskers, particles, short fibers, and continuous fibers are produced by different manufacturing techniques including solid and liquid state processing.

2.1.1. Applications of Metallic Matrix Composites (MMCs)

By using selective reinforcements and composite manufacturing techniques, MMCs offer economically practical solutions for a number of commercial applications, including:

1. Transportation Sector: the most important aspects of using MMCs in this application is to lower fuel consumption, noise and emissions. MMCs have being used to manufacture fiber reinforced pistons and aluminum crank cases in addition to particle strengthened brake discs.
2. Military Applications: MMCs are good candidate materials for high temperature aircraft engines and structures, missile structures, military communication satellite, as well as structural applications such as armor, and armament.
3. Medical Technology: MMCs are used where mechanical properties such as extreme corrosion resistance, low degradation, and biocompatibility are required.

2.1.2. Effect of Ceramic Reinforcements on the Behavior of Aluminium Matrix Composites

The presence of a ceramic reinforcement with a volume fraction of more than 10% has a significant effect on how aluminium matrix composites behave during manufacturing and their following performance in service. Some of the most outstanding effects include microstructural variations, heat treatment characteristics, tribological properties, thermal stresses, machinability and weldability.

On the other hand, the presence of ceramic reinforcement can modify the solidification behavior of the aluminium matrix. Ceramic reinforcement may be a barrier to components diffusion and heat transfer, promotes the heterogeneous nucleation, and restricts fluid convection. Kainer (2006), reported that the matrix grain size is reduced by the heterogeneous nucleation of aluminium on the surface of the ceramic reinforcement.

Aluminium matrix composites are exposed to fabrication temperatures higher than 500°C, and consequently, a large amount of thermal residual stresses during cooling are generated. The extent of these thermal residual stresses depends on many factors such as reinforcement type, volume fraction, diameter, and aspect ratio. The mechanical behavior of MMCs is highly affected by thermal residual stresses reducing the fatigue and creep behavior.

However, wear resistance is significantly improved by introducing ceramic reinforcement in the aluminum alloys. This effect has been successfully used in MMC brake discs. The incorporation of this ceramic reinforcement also modifies the age hardening characteristics.

The effects of reinforcement on the final properties are influenced by morphology, composition, size, and volume fraction of the reinforcement as well as on the fabrication method of the composite. According to Surappa (2003), a change on the age hardening of aluminium matrix characteristics due to the enhanced dislocation density results after the incorporation of ceramic particles. The increment in dislocation density is a consequence of the large mismatch in the coefficients of thermal expansion between the ceramic particles and the aluminium matrix .

2.1.3. Particle Reinforced Metallic Matrix Composites (MMCp)

Ceramic particle reinforcements are generally oxides, carbides, or borides (Al_2O_3 or SiC or TiB_2) with a volume fraction lower than 30%, for wear resistance and structural applications.

Although, reinforcement with volume fraction as high as 70% has been used in electronic packaging applications.

Kainer (2006) reported lower mechanical properties for particle reinforced MMCs, compared to whisker, short fiber and continuous fiber reinforced MMCs, yet superior compared to monolithic alloys. These composites are isotropic and because of their nature can be subjected to secondary forming operations including extrusion, rolling and forging.

Generally, MMCs are made via solid state or liquid state processing including stir casting, infiltration and other in-situ processes. The liquid state processing is more cost efficient and is relevant to this thesis.

The process variables include the temperature at which the particles are introduced, temperature and time of heat treatment for the particles, feed rate of the particulate, particles size and shape, volume percent of the dispersoids and melt degassing. These variables affect the dispersion of the ceramic particles, and consequently the final mechanical properties. The stability between aluminium and ceramic particles, and the differences in their thermal properties, such as coefficients of thermal expansion and thermal conductivity, are some of the key factors in determining the compatibility of the materials constituents.

MMCp have effectively been used in automotive, aerospace, gas turbine engine, recreation, computer and thermal managing technologies. Some examples are breaking systems of trains and cars, golf club shaft and head, skating shoes, baseball bats, horseshoes, bicycle frames, microprocessor lids, and integrated heat sinks in electronic packaging. Recently they have been used also as carrier plates and microwave housing.

2.1.4. Liquid state processing: MC-21 Rapid Mixing Process for Production of MMCs.

MC-21, Inc., has developed, patented, and proved on a commercial scale, a proprietary process improvement for MMCs. This process achieves greater efficiency in the mixing operation at lower processing cost. A schematic of mixing system is shown in Figure 2.

Some of the proven benefits of this technology are:

- ✓ Rapid mixing of ceramic particles into the molten aluminum
- ✓ Lower cost possessing
- ✓ Wider size of ceramic particles distributions to be used
- ✓ Up to 45 vol.% (50 wt.%) of ceramic included into the molten aluminium

This process is appropriate for the mixing of ceramic reinforcement particles, such as SiC, B_4C, and Al_2O_3. This innovative process has been developed by MC-21, Inc, located in Carson City, NV, USA.

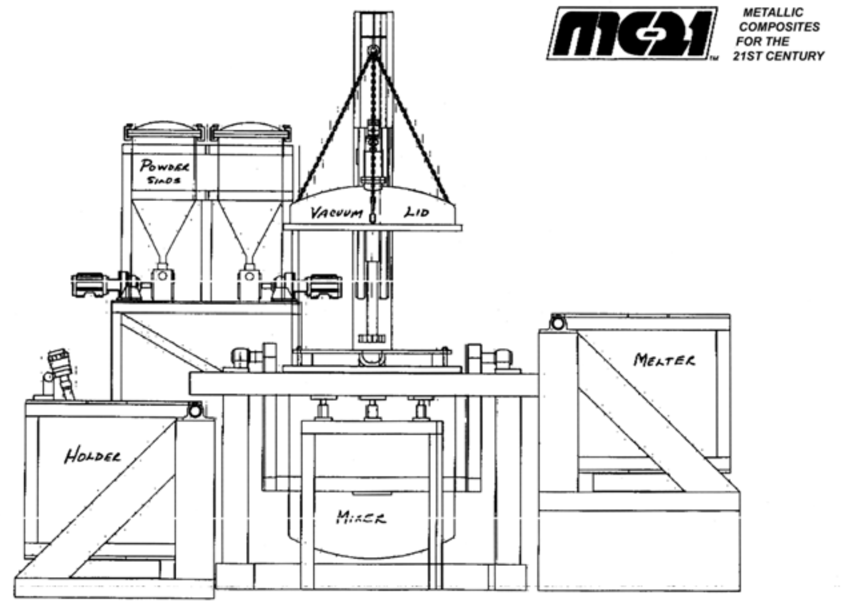

Figure 2. MC-21 liquid state modular mixing system. Herling *et al*, (2001).

This design started as an improvement of the conventional stir casting process for MMCs, known as Duralcan. The technology developed by MC21 reduces the reinforcement incorporation time to under 60 minutes. This design is based on a modular unit of production which feeds the molten composite to a casting machine. In other types of processes, remelting of the MMC ingot is necessary. The new design allows to save time, minimize overheat, and reduce energy consumption. An extensive range of reinforcement size and volume fraction are applicable under this technique. Reinforcement amounts of up to 45% of volume (50% of weight) of SiC are being produced with this technology. MC-21 has made a large effort on continues research and development on a number of matrix alloys and possible reinforcement combinations.

With this new rapid mixing process, better casting properties are obtained if compared to other techniques due to the lower levels of oxide skins and gross yield. A cleaner result is even obtained with lower cost reinforcement and high reinforcement content. The properties of this low cost MMC manufacturing process are comparable to or superior to those produced with conventional techniques with similar casting conditions.

This process permits the mixing of the aluminum and the reinforcement at atmospheric conditions, eliminating the need for complex and expensive vacuum systems. A controlled inert atmosphere (argon or nitrogen) prevents the melt from reacting with the oxygen in the air, efficiently reducing the build-up of an oxide layer. This novel approach is based on how the particulate reinforcement is introduced to the melt. With the new mixing head design, it is possible to break up agglomerations of ceramic particles, create a higher level of shear forces in the melt, and consequently, mix and distribute the reinforcement. Also the deign does not create vortex when rotated in the melt, eliminating significant surface movement and preventing pulling oxides from being pulled to the surface into the melt.

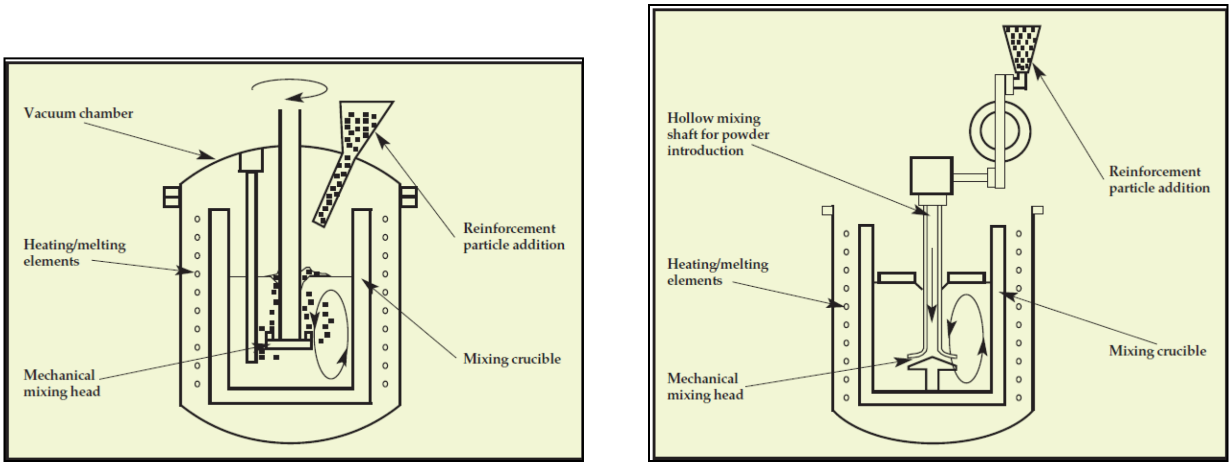

a) b)

Figure 3. a) Conventional and most common method of stir-casting setup for making aluminum MMC material. b) Rapid mixing concept and compositing chamber setup developed by MC-21. Herling *et al*, (2001).

Herling *et al*, (2001) describes the rapid mixing process as follow: the particles are introduced below the surface into the melt by means of a hollow mixing shaft, as shown in Figure 3. The mixing head promotes the breakup of particle clusters and final distribution of the reinforcement in a vertical axial movement. Higher shear forces are obtained by processing in a semi-solid state and resulting in a higher viscosity of the melt. Given that the impeller design does not create a vortex in the melt, rotating speed can be increased, enhancing the size of the shear region, efficiency of the particle's wetting, and mixing action of the particles. Additionally, the position of the shear zone is located in the most favorable location, where the particles are first introduced into the matrix as they disseminate from the hollow mixing shaft. This reduces the time required for the particles to reach the shear region, and significantly increases the fraction of particles that pass through the shear zone, leading to an increase in the rate of wetting. The modification of the mixing action in the shear zone helps to control the final process.

The short processing time, equipment simplicity, and potential to use low cost reinforcement make possible to produce MMC at less than $1/pound. This is an impressive improvement over other MMCs produced. High cost of conventional aluminum alloys discourages common industrial applications, but the problem is resolved with the new option offered by MC-21. Unique material properties at low cost and efficiency are possible with this technology.

The smallest unit produced by MC-21 is a unit of 5 kg lab scale mixer (5 kg batch size). A 60 kg, 200 Kg, and 600Kg have been also developed and constructed.

A schematic image of the 600 kg unit is shown in Figure 4 . This image shows the melting, mixer, powder silos for containing and feeding of ceramic reinforcement into the mixer, vacuum lid to seal the mixing unit, and holding units that are part of the modular unit.

Figure 4.Melter (furthest back), Mixer (middle position), and Holding furnace (front). MC-21's prototype of 600 kg modular mixing system. Herling *et al*, (2001).

The success of this MC-21 rapid mixing process is justified by the capacity to efficiently and quickly incorporate the reinforcement particles into the molten metal allowing versatile mixing conditions. Furthermore, a more efficient process and equipment can be applied in order to provide a system that is less tedious and more cost-effective.

2.2. Microstructure of Al-Si Casting Alloys and SiCp Reinforced Aluminum Metal Matrix Composites

Cast aluminum-silicon alloys are commercially used as structural materials due to their physical, chemical and mechanical properties. The main characteristic of these alloys is the relative density to high tensile strength which is a consequence of the their multiphase microstructure. The commercial silicon content in cast aluminum alloys is between 5 and 23 wt%. The properties of the aluminium alloy are accredited to the volume fraction, individual properties, and morphology of its components (aluminum solid solution and silicon precipitates).

2.2.1. Properties of Aluminum Solid Solution

In cast aluminum silicon alloys, the aluminum solid solution is the matrix which crystallizes with dendrite structure. The crystallographic lattice of the solid solution is a close packed face centered cubic (fcc) lattice ($A1$), with four atoms in the unit cell, and a coordination number of 12. Crystal structure of the aluminium solid solution is presented in the Figure 5 (a).

According to Warmuzek (2004), the main characteristics of this crystal structure and type of bonding and important features determining the physical properties, specifically the low resistance to plastic deformation, are:

- The closest packed plane and direction are {111}, and <110>, respectively.
- Metallic bonding is predominant for this alloy characterized by low bonding energy and isotropy.
- Each aluminum atom has three valence electrons.

- The existence of defects such as dislocations, point vacancies, and stacking faults are some of the causes of the aluminum's low tensile strength.
- The stacking-fault energy of aluminum is high as well as a very high density of moving dislocations. In A1 (fcc) metals, the resistance to dislocation movement (Peierls-Nabarro forces) are low.
- Plastic deformation caused by slip is relatively easy because of the 12 slip systems in the *A*1 lattice {111}, <110>. The plane {111} is an energy advantaged plane for easy slip as a result of the small distance between partial dislocations.
- The strain-hardening factor for aluminum is 0.15 to 0.25 (half of austenitic steel)
- Light specific weight is third part of steel, of 2.7 g/cm^3.
- Aluminium creates a protective coating oxide being consequently highly corrosion resistant.
- Aluminium is an excellent electricity and heat conductor.
- Aluminium is recyclable with low energy for re-melting .

2.2.2. Properties of Silicon Crystals

Silicon precipitates added to Al-alloys have a high purity level and can have a diverse morphology: primary precipitates in hypereutectic alloy or branched plates in aluminum silicon eutectic. The Silicon crystal lattice is a cubic diamond type, *A*4 . Each atom with a covalent bond with four forming a tetrahedron. Eight tetrahedrons form an elementary cell of *A*4 lattice with four additional atoms at the center of each tetrahedron as predicted in Figure 5(b).

Because of the covalent character of Si, the ions cannot move under a force unless the bonds are completely broken. Then the material becomes brittle with cracks propagating instantly with decohesion taking place on the cleavage planes. The cleavage plane, {111}, is the preferential plane for the brittle fracture due to its small surface energy.

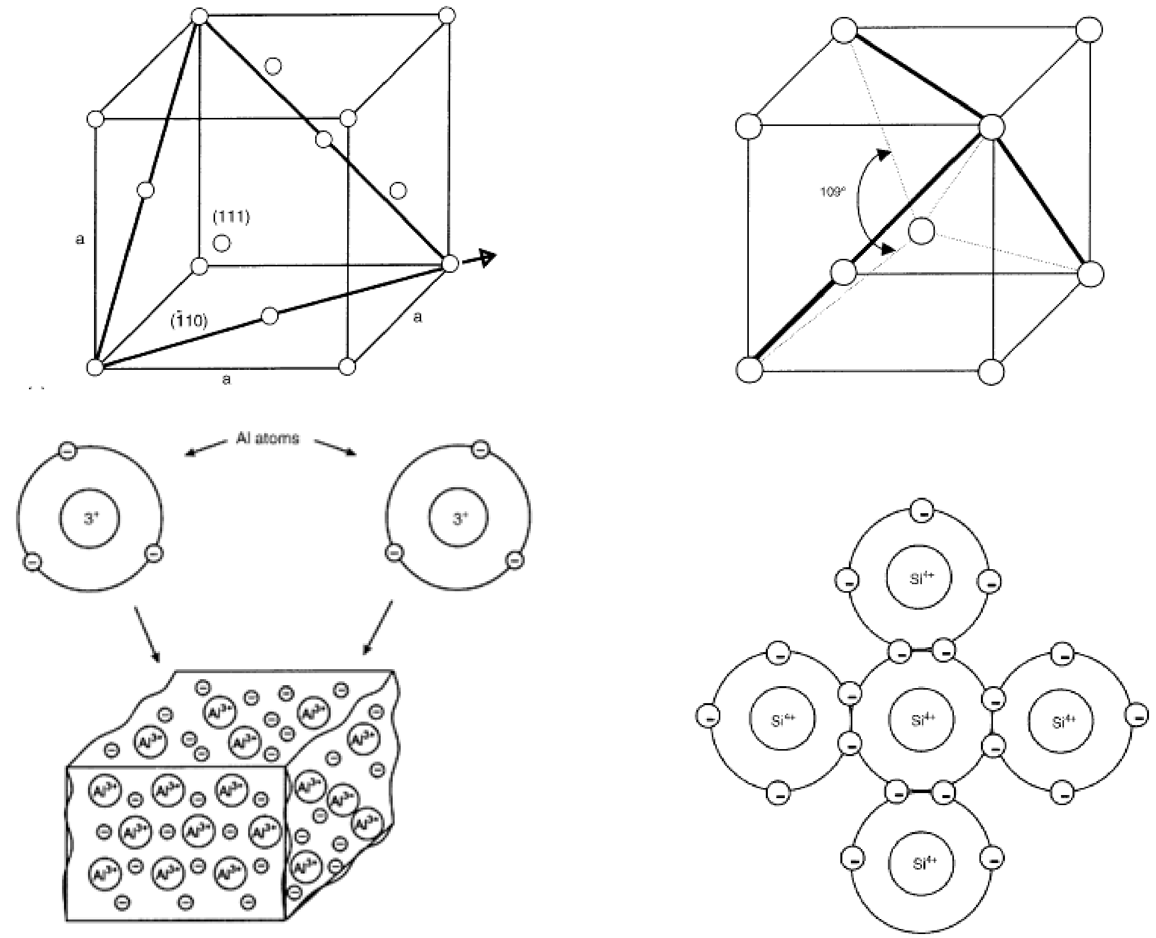

a) b)

Figure 5. (a) Unit cell of aluminium and interatomic bonds in the Aluminum lattice. b) Unit cell of the Si and interatomic bonding in silicon lattice. (Warmuzek, 2004).

2.2.3. Properties of Aluminum-Silicon Alloys

Mechanical properties of Al-Si alloys were described in detail by Warmuzek (2004). The average stress in the Al-Si alloy can be determined as a linear function of the silicon volume fraction:

$$\sigma = \sigma_{\alpha} V_{v}^{\alpha} + \sigma_{Si} V_{v}^{Si} = \sigma_{\alpha} + V_{v}^{Si} (\sigma_{Si} - \sigma_{\alpha}) \tag{1}$$

where σ_α and σ_{Si} are the stresses.

The size of the brittle Si phase particles influences the stress-intensity factor and consequently impacts the elastic and plastic properties of the metallic matrix. However, the equation does not take into account the influence of average size, morphology, and distribution of brittle particles. These parameters can make an important distinction in the properties. The Hall-Petch equation describes the influence of the grain size on the stress

$$\sigma_{pl} = \sigma_s + k_m d^{-1/2} \tag{2}$$

where σ_{pl} is the stress of the polycrystal , σ_s is the resistance of the lattice to dislocation movement, k_m is the hardening factor and d is the grain diameter.

The stress σ_s is the sum of σ_p and σ_d. The first one is independent of temperature but dependent on the lattice structure. σ_p expresses interactions among dislocations, precipitates, and other atoms. The second one is temperature dependent.

$$\sigma_{pl} = \sigma_p + \sigma_d + k_m d^{-1/2} \tag{3}$$

Warmuzek (2004) described how the microstructure effect in the Hall-Petch formula depends on the dendrite arm size λ and the size of silicon lamellas γ. The relationships between ultimate tensile strength (R_m) and secondary dendrite arm size can be expressed by:

$$R_{0.2} = k + k_5 \gamma^{-1/2} + k_6 \lambda^{-1/2} \tag{4}$$

$$R_m = k + k_2 \gamma^{-1/2} + k_3 \lambda^{-1/2} \tag{5}$$

where k, k_2, k_3, k_5, and k_6 are experimental constants, γ is the size of silicon lamellas in interdendritic eutectic regions, and λ is the secondary dendrite arm size. $R_{0.2}$ is the 0.2% off-set strength.

Using cast technology, heat treatment and thermomechanical processes, it is possible to improve the mechanical properties of cast aluminum-silicon alloys. An increase in the strength of the matrix is possible by tailoring the polycrystalline structure. Minimizing the brittle fracture behavior in the multiphase regions is also possible by increasing the degree of dispersion of the structure.

Brittle fracture can be reduced if the stress-concentration at the silicon particles is reduced, mitigating potential crack initiation regions. To break up and spheroidized the network of silicon precipitates is very important in order to reduce the brittle fracture.

Microstructures with a fine morphology have less propensity to low-energy brittle cracking. The reduction of the stress-concentration factor K_n depends on *a (* half of the length of a particle) and *b* (half the width of a particle) described as:

$$K_n = 2a/b \tag{6}$$

For silicon concentrations greater than 1.65 wt%, the two phases (Al and Si) solidify. The influence of silicon on the final mechanical properties can be described by:

$$\sigma = \sigma_\alpha V_v^\alpha + \sigma_{Si} V_v^{Si} = \sigma_\alpha + V_v^{Si}(\sigma_{Si} - \sigma_\alpha) \tag{7}$$

Figure 6 reveals the influence of morphology and distribution of silicon precipitates on the mechanical properties.

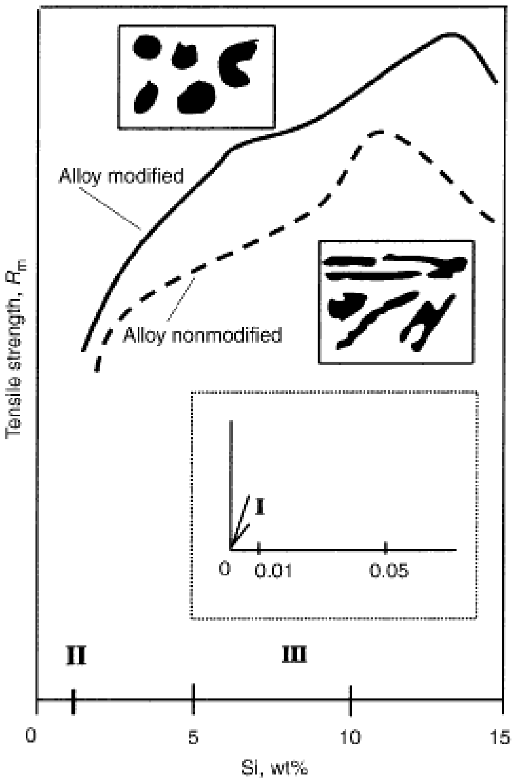

Figure 6. Tensile strength versus silicon content in Al-Si cast alloy.
(Warmuzek, 2004).

2.2.4. The Eutectic Si

The addition of silicon to aluminum reduces the melting temperature, and leads to improvement in cast fluidity, feeding and hot tear resistance. Silicon added into the aluminum by itself produces a non heat-treatable alloy. Nevertheless, silicon in combination with magnesium can produce a precipitation hardening heat-treatable alloy. In the casting industry, the addition of silicon to aluminum is a common practice. The hardness of the alloy is increased with the alloying of hard Si. Thus, ductility and machinability are reduced.

Eutectic Al-Si alloy is a common cast aluminium alloy. Modification of Si morphology has been recently studied for Ogris *et al* (2002) as an alternative for the improvement of mechanical properties, specially the low plasticity which is one of the most remarkable characteristics of this alloys. Variation in morphology, size, and distribution of Si is found after heat treatments and thermomechanical processing.

2.2.4.1. The Al-Si Eutectic

In this study, A359 is the matrix alloy examined. Silicon improves the casting characteristics of the alloy, reduces the thermal expansion coefficient, and increases wear and corrosion resistance. When the Al-Si alloy solidifies, the primary aluminum is developed in dendrites, and the silicon phase forms and grows as angular primary particles in the Al interdentritic locations. At room temperature, these hypoeutectic (8.5-9.5% Si) alloys are composed by a ductile primary aluminum phase and a brittle eutectic silicon phase.

The Al-Si eutectic differs from other conventional eutectic microstructures in that at any given temperature, aluminum has near-zero solid solubility in silicon. Thus, there is near pure silicon instead of a β (solid solution of Al in Si) phase. In the Al-Si alloys, the eutectic composition is a structure of α (Solid solution of Si in Al) + Si rather than α+β. The phase diagram in Figure 7 shows a eutectic reaction ($L \rightarrow \alpha + Si$) at a composition of 12.6 wt.% Si and a temperature of 577^{o}C (isothermal). The maximum solubility of silicon in aluminum is 1.65 at.% at the eutectic temperature.

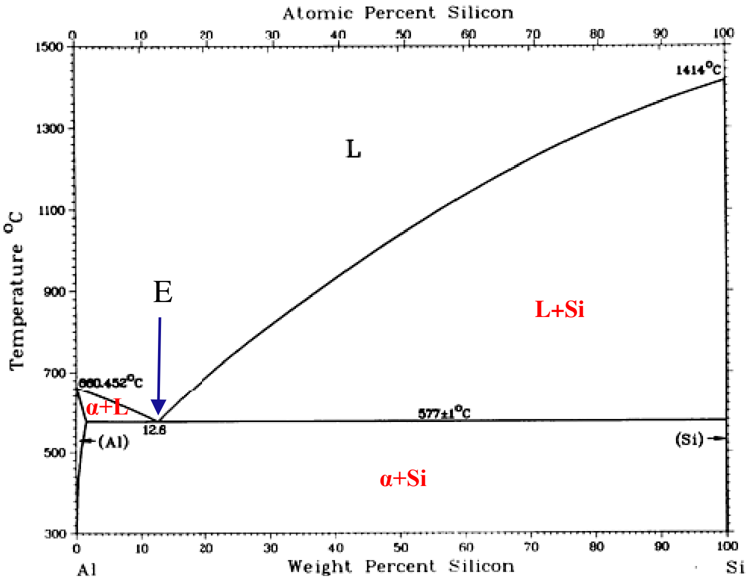

Figure 7. Binary phase diagram Al-Si. (ASM Handbook, 1992)

The microstructure of these alloys can be eutectic, hypoeutectic, and hypereutectic as presented in Figure 8. The eutectic microstructure appears as platelets interconnected three dimensionally. These sharp platelets of Si in the eutectic are responsible for brittleness. Therefore, large plates of silicon are unfavorable to the mechanical properties. An addition of a small amount of impurities or modifiers to the melt makes the nucleation of silicon more difficult. Solidification is suppressed until lower temperatures where there is larger nucleation rate. As a consequence, a refinement of the microstructure is obtained. Also, the phase diagram may change so that the eutectic point is lower in temperature and higher in silicon concentration.

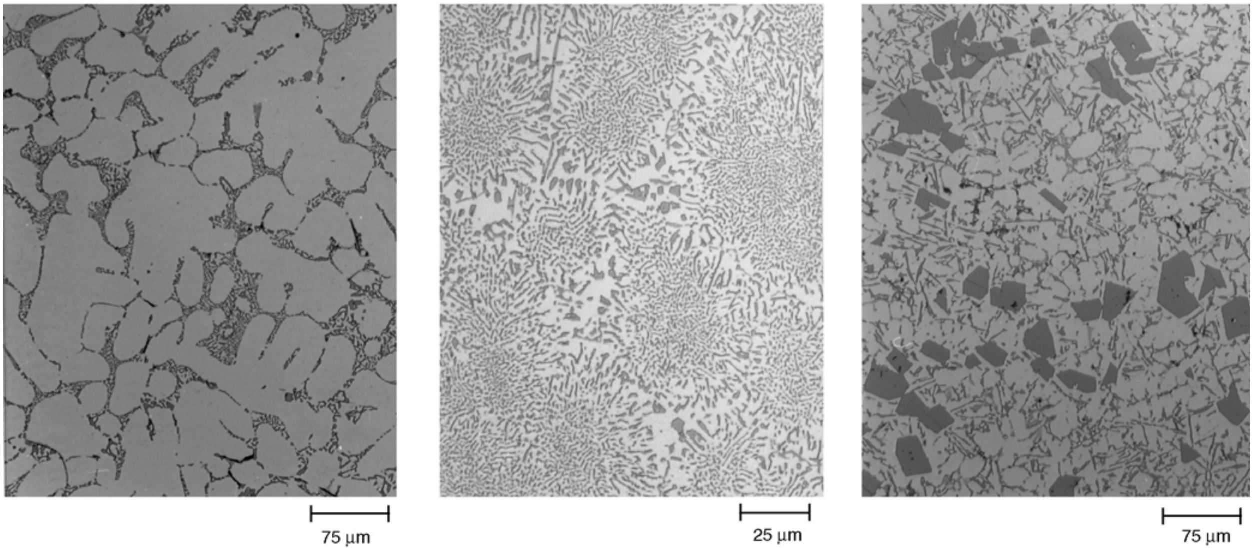

Figure 8. (Warmuzek , 2004). Commercial cast aluminum-silicon alloys microstructures. (a) Hypoeutectic alloy (1.65-12.6 wt% Si), (b) Eutectic alloy (12.6% Si), and (c) Hypereutectic alloy (>12.6% Si).

2.2.4.2. Diffusion of Silicon in Aluminum

Si can migrate at the Si-Al interface by two different mechanisms:

1. Surface self diffusion: Silicon changes its atomic location by diffusing on the Si-surface.

2. Interdiffusion: Silicon leaves the silicon lattice by migrating throughout aluminum at the Al-Si interface favored by the phase boundary's lattice defects.

Many studies have been performed in order to investigate the interdiffusion in the A1-Si system, but the results differ significantly among authors. Fujikawa *et al*, presented that the most probable mechanism is the Al-Si surface interdiffusion which has a activation energy of ~1.4 eV instead of the ~2.3 eV for surface self diffusion.

Fujikawa used the following approach in order to describe the interdiffusion coefficient at the Si-Al interface:

$$D_{inter} = D_{0,inter} \cdot \exp\left(-\frac{E_{A,inter}}{R \cdot T}\right) \tag{8}$$

where $D_{0,inter}$ is the frequency factor and $E_{A,inter}$ the activation energy for interdiffusion which is the summary of the activation energy for the atom's migration, $E_{A,m}$, and the activation energy for vacancy formation, $E_{A,v}$.

The change of volume after the casting solidification is compensated by the formation of vacancies in aluminum at the Al-Si interface. Hence, the vacancy probability at the Si-Al interface equals almost 1. Then, the activation energy of vacancy formation can be neglected. Ogris *et al* (2002) describes the diffusion coefficient, D_s, for silicon at the Si-Al interface as:

$$D_s = D_0 \cdot \exp\left(-\frac{E_{A,\text{inter}} - E_{A,v}}{R \cdot T}\right) \tag{9}$$

where, $E_{A,inter}$ describes the activation energy for interdiffusion of Si in Al and $E_{A,v}$ is the activation energy of vacancy formation in Al.

During high temperature treatments such us annealing, the sharp silicon platelets spheroidizes. This change in the morphology of the eutectic Silicon leads to an enhanced tensile strength and ductility as reported by Ogris *et al* (2002).

The evolution of this spheroidization mechanism starts with the disintegration of the silicon, follow by spheroidization and subsequent growth of the Si particles in the Aluminum matrix. This behavior is a consequence of a series of competitive mechanisms associated with the amount of discontinuities and to the Al/Si interfacial aspects. One of the most accepted mechanisms proposed by Ogris *et al* (2002) considers the driving force for spheroidization as the same force responsible for the disintegration of water jets, the minimization of surface energy under the effect of surface tension.

2.2.4.3. Theory of Ostwald ripening

Ostwald ripening theory describes the evolution of the inhomogenous distribution of Si particles throughout the time. This phenomenon was described by Wilhelm Ostwald in 1896 as schematically illustrated in Figure 9.

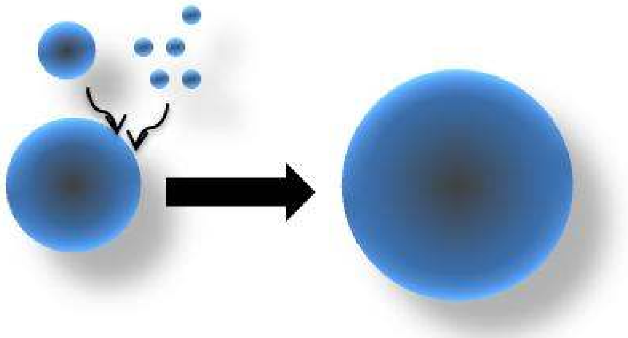

Figure 9. Evolution of isolated Si particles of different size in close proximity. They are assumed to be spherical .

When the Si precipitates within the Al-Si solid solution, energetic factors cause large precipitates to grow, consuming the smaller precipitates, which shrink and disappear. The driving force for this phenomena is to minimize the surface free energy of the individual Si particles.

This is because atoms on the Si particles' surface are energetically less stable than the atoms in the interior. With lower surface to volume ratio, large particles may result in a lower energy state caused by the lower surface energy. Therefore, larger particles continue to grow while the number of smaller particles continues to shrink.

The concentration of the atoms around the interface of smaller Si particle is larger than the average concentration in bulk solution, resulting in diffusion of individual atoms that will proceed from the smaller to larger until the former disappears entirely. The small particles give up their mass to larger clusters of Si that are growing.

2.2.4.4. Silicon Spheroidization Model

Ogris *et al* (2002) divided the morphology of eutectic silicon into two types: a non-modified plate-like shape and a fine fibrous modified cylinder-like shape. The thermal degradation of the Silicon plates starts at morphological faults on the crystal such us terminations, kinks and striations of the un-modified plates as well as voids and fissures in the plates (Werner, 1990). Disturbances are responsible for the thermal instability of these structures. A modified structure with a coral-like shape will disintegrate and spheroidize easier and faster than the unmodified sharp platelets.

Al-Si eutectic alloys consist of rods of one Si embedded in the surrounding metallic matrix of Al. The shape instability of rods was first explained by Lord Rayleigh (1878). Although his theory was established for the shape instability of jet fluids, it is a great approximation to describe the spheroidization of the rod phase in an eutectic alloy. Ogris *et al* (2002) adapted Rayleigh 's model for the disintegration of eutectic silicon corals in Al-Si alloys.

Several authors such us Stuwe and Kolednik (1988). Ogris *et al* (2002) and Ballufi *et al* (2005) theoretically presented how these structures, if thermally activated, disintegrate into small spheres under the influence of surface tension, capilarity and applied mechanical forces.

Ogris *et al* (2002) simplified the silicon corals as cylinders interconnected with infinite length and radius ρ which transforms into a row of equidistant spheres of radius *R* and spacing *l* as shown in Figure 10.

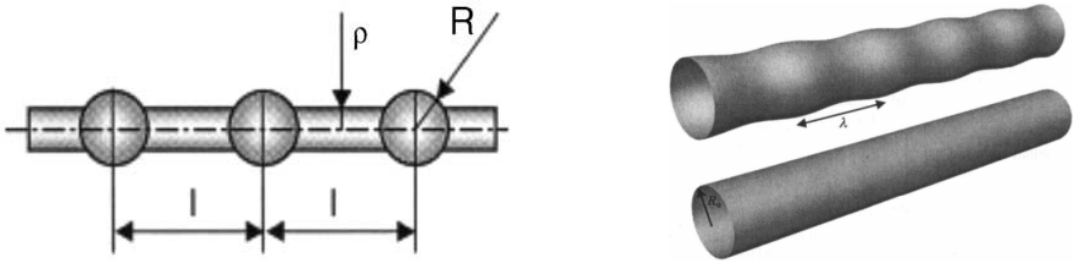

Figure 10. Silicon Cylinders (Ogris *et al* , 2002; and Ballufi *et al*, 2005)

Geometry shown in Figure 10 can be expressed as:

$$Z = \frac{l}{\rho} \qquad \text{and} \qquad a = \frac{l}{R} \tag{10}$$

The volume is constant during the shape transformation from a cylinder to a sphere:

$$a = \left(\frac{4}{3}\right)^{\frac{1}{3}} \cdot z^{\frac{2}{3}} \approx 1.1 z^{\frac{2}{3}} \tag{11}$$

From the condition that the surface of one sphere must not be larger than the lateral surface of the cylinder:

$$2\pi\rho l \geq 4\pi R^2 \tag{12}$$

Then,

$$a \geq 3 \qquad \text{and} \qquad z \geq \frac{3}{2} \tag{13}$$

The cylinder must be unstable against fluctuations of its diameter in order to disintegrate.

Fluctuations of the diameter were described by Stuwe and Kolednik (1988) as:

$$r = s + A \cdot \sin \frac{2\pi}{l} \cdot x \tag{14}$$

where r is the fluctuation of the radious, s is the mean radious of the body, A is the amplitude of the disturbance, l is the wavelenght, and x is the direction to where the cylinder is revolving.

The mean radious follows:

$$S = \rho \left(1 - \frac{A^2}{2\rho^2}\right)^{1/2} \tag{15}$$

Because the volume of the disturbed cylinder (spherical shape) is conserved during the transformation, we can calculate the new surface of the body as:

$$S = 4s\left(1 - \frac{4\pi A^2}{l^2}\right)^{1/2} E\left(\frac{1}{1 + \frac{l^2}{4\pi^2 A^2}}, \frac{\pi}{2}\right) \tag{16}$$

We assume that the cylinder is transformed to one sphere. Where $E = (m, \frac{\pi}{2})$ is the elliptical integral approximated by a polynomial function. The surface difference between the disturbed and undisturbed cylinder was calculated as:

$$S - S_0 \approx \frac{\pi}{2} \cdot A^2 \cdot \frac{4\pi^2 - z^2}{z} \tag{17}$$

where S_0 is the surface of is the surface of the undisturbed cylinder.

Rayleigh 's mode (1878) stated that the cylinder will be unstable against a longitudinal fluctuation, if its wavelength l is larger than the cylindrical circumference, or if $z \geq 2\pi$ as shown in Figure 11.

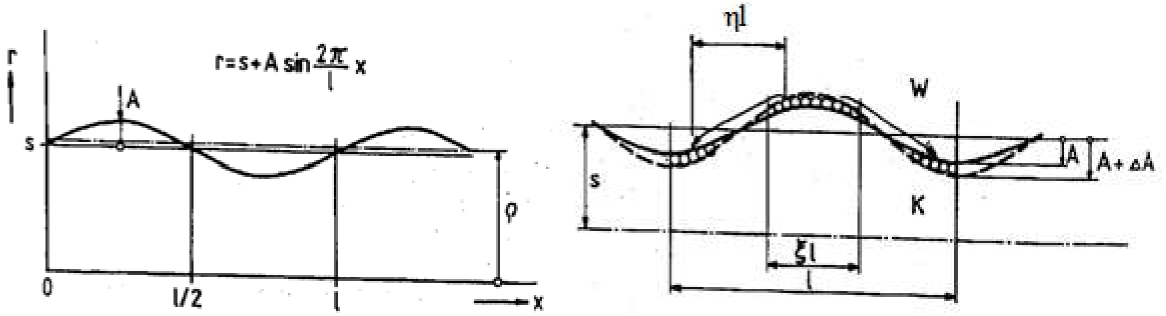

Figure 11. Shape instability of thin cylinders (Stuwe and Kolednik, 1988)

The Si cylinders may be weakly disturbed by a fluctuation with amplitude *A* and wavelength $l \geq 2\pi p$. If one layer of atoms, consisting of *N* atoms, diffuses from the adjoining necks to the bulge of the cylinder, the amplitude of the fluctuation will be increased by the atomic diameter, $\Delta A = \phi$

The gain of surface energy caused by this fluctuation will be represented by:

$$\Delta U = \Delta S\gamma = \pi \frac{z^2 - 4\pi^2}{z} A\Delta A\gamma \tag{18}$$

where γ is the specific energy of the Si-Al interface.

A constant average driving force for the diffusion of one Si atom is assumed as:

$$F = \frac{1}{N}.\frac{\Delta U}{l} \tag{19}$$

The mean velocity of the Si atoms (in x-direction) is given by the Nernst-Einstein relationship:

$$\upsilon_{Si} = F.\frac{D_s}{kT} \tag{20}$$

where T is the temperature, k is the Boltzmann‘s constant and D_s is the coefficient of surface diffusion at the Si-Al interface. If ηl denotes the mean diffusion path in x-direction, the growth rate, v_A, of the fluctuation amplitude will be

$$\upsilon_A = \frac{dA}{dT} = \frac{\phi}{\eta l}.\upsilon_{si} \tag{21}$$

The total number of diffusing atoms, N, in a cylinder fraction of length ξl is assumed as the number of atoms covering the exterior of the cylinder fraction, thus:

$$N = \frac{2\pi\rho}{\phi}.\frac{\xi l}{\phi} \tag{22}$$

Equation (21) is transformed to

$$\frac{dA}{dT} \approx \frac{1}{2\eta\xi} \cdot \frac{D_s\gamma}{kT} \cdot \left(\frac{\phi}{\rho}\right)^4 \cdot Z \cdot A \tag{23}$$

with

$$Z = \frac{z^2 - 4\pi^2}{z^4} \tag{24}$$

Integrating Equation (23), the fluctuation amplitude at a given annealing time t is:

$$A(t) = A_0 \cdot \exp\left[\frac{1}{2\eta\xi} \cdot \frac{D_s\gamma}{kT} \cdot \frac{\phi^4}{\rho} \cdot Z \cdot t\right] \tag{25}$$

assuming an amplitude A_0 of the original disturbance. The condition $A(\tau) = \rho$ provides an estimate of the disintegration time, τ, of the cylinder, as:

$$\tau = 2\eta\xi \cdot \frac{kT}{D_s\gamma} \cdot \left(\frac{\rho}{\phi}\right)^4 \cdot \frac{1}{Z} \cdot \ln\frac{\rho}{A_o} \tag{26}$$

The function Z is a measure for the driving force for the break-up of silicon. It depends on the geometry of the cylinder, and it is not influenced by the mass transport mechanisms. It describes the growth rate of the fluctuation amplitude, and has a maximum value at

$$z_{\max} = 2\pi\sqrt{2} \approx 8.8 \quad \text{or} \quad Z_{\max} = \frac{1}{16\pi^2} \approx 0.006 \tag{27}$$

Wavelengths smaller than $l = 2\pi\rho$ will be reduced very quickly because Z is then negative and large. All fluctuations with larger wavelengths grow. The original disturbance is assumed to have a wavelength of $l = z_{max} \cdot \rho$, and the smallest possible amplitude is $A_0 = \phi$, where ϕ is the atomic diameter of silicon. The factors η and ξ, determining the mean diffusion path and the number of the diffusing atoms, are roughly estimated by Ogris *et al* (2002) as 1/3. Substituting this value into Equation (26) leads to the disintegration time, τ_{max}, of a cylinder having a maximal growing fluctuation amplitude as:

$$\tau_{\max} = \frac{32\pi^2}{9} \cdot \frac{kT}{D_s \gamma} \cdot \left(\frac{\rho}{\phi} \right)^4 \cdot \ln \frac{\rho}{\phi} \tag{28}$$

From this formula, it is clear how the disintegration time is influenced by the radius, ρ, of the original cylinder and the diffusion coefficient D_s (Diffusion of Si at the Al-Si interphase).

2.2.5. SiCp- Al A359 Metallic Matrix Composites: The Effect of Main Alloying Elements.

The incorporation of SiCp to aluminium alloy improves the strength of the composite in addition to the contribution by the added strengthening precipitates such as Si. Si has been reported to have a large influence on the properties of MMCs (Warmuzek, 2004 and Ogris, *et al* , 2002). Mg_2Si, SiO_2,$MgAl_2O_4$, and Al_2O_3 phases have been postulated by Myriounis *et al.* (2008) as possible precipitates in this type of composites.

At the end of the solidification process, SiC is located at the Al-Si eutectic region, along the interdendritic arms. Additionally, Myriounis *et al.* (2008) observed that Si nucleates and grows on SiC particles. In some cases, some SiC particles are joined together in a network by the Si phase.

Magnesium is added to the Al A359 to improve the mechanical properties of this alloy via a heat treatment process. As a consequence, Mg–Si precipitates nucleate uniformly at grain boundaries and within grains. The Mg_2Si forms with a sequence as follow:

1. A supersaturated solid solution
2. GP zones
3. β'
4. β (Mg_2Si)

Myriounis *et al.* (2008) describes the GP zones as needle shaped precipitate along the aluminium matrix, the β' phase as a rod shaped along the matrix precipitate, and the equilibrium phase β as a face centered cubic precipitate which forms platelets on the matrix.

In addition to Mg_2Si, $MgAl_2O_4$ is present due to the reaction of the SiO_2 at the surface of SiC (at the interface between the metallic matrix and the ceramic reinforcement) and the aluminium alloy melt. $MgAl_2O_4$ can form as a layer and protects the SiCp from the liquid aluminium during liquid processing. This layer may promote a higher bonding strength between the particle and matrix.

The addition of silicon and the existence of Al_2O_3 inhibit the formation of Al_4C_3. If the melting temperature of the composite materials is raised above a critical value, Al_4C_3 can form. The Al_4C_3 increases the viscosity of the molten material, and a severe loss of corrosion resistance and degradation of the mechanical properties.

The principal features that contribute to the SiC-Al interphase strengthening are:

- ✓ Constraint effects provided by the SiC particles, which is harder than the aluminium matrix

- ✓ Residual stresses close to the SiC particles due to a mismatch in the coefficient of thermal expansion between ceramic particle and metallic matrix.
- ✓ Local chemistry changes due to Mg segregation and formation of spinel ($MgAl_2O_4$)
- ✓ Higher dislocation density around the SiC particles due to mismatch in the coefficient of thermal expansion
- ✓ In the case of presence of a crack in the matrix, these precipitates promote crack deflection at the interface resulting in an increase of the composite's fracture toughness.

Globular microstructure with very fine and homogeneous SiC distribution and a very low level of voids produced during the solidification process are required in order to achieve good mechanical properties. Using heat treatments and/or thermomechanical processing, mechanical properties of the composite can be strongly improved.

2.3. Thermomechanical Processing: Hot Rolling

Thermomechanical processing techniques are applied to MMCs in order to integrate heat treatment and consolidation in one single and economic process. Hot rolling processing is one of these techniques employed by MC-21 for the MMCs under study.

In the hot rolling process, cast composites pass through a pair of metallic mills at rates approaching 2,000 feet per minute (600 m/min). The process is classified as hot rolling because the composite slab is pre-heated in a furnace, reaching a temperature above its recrystallization temperature, high enough to avoid strain-hardening (work-hardening) as the metal is deformed. The metallic grains of the aluminium matrix deform during this process, but because recristallization is taking place, the equiaxed microstructure of the grains is maintained, preventing the metal from work hardening, directionality in the mechanical properties, and residual stress induced by deformation. Hot rolling is a great technique for consolidation of the composite slabs due to its low cost and high speed. However, rolling the MMCs may have significant effects on the final microstructure and consequently on the processed mechanical properties. Some of these effects have been described by several authors (*e.g.*, Wang, A.*et al*, 1996; Taha, M.A. *et al*, 2003, and Myriounis, D.P. *et al*, 2008) as summarized below.

Hot rolling has two important metallurgical effects:

1. It welds and closes voids left by the casting process, creating a denser and stronger composite.
2. It breaks up and redistributes hard precipitates of silicon which have formed at aluminium grain boundaries which transforms brittle cast alloys into ductile alloys. The disintegrated and re-distributed precipitates enhance the ductility by offering less resistance to the internal metal flow.

The reduction per pass, the directionality of the rolling, and the rolling temperature have an impact on the metallurgical characteristics of the MMCs. The rolling temperature is selected according to the final product properties to be achieved. Excessive high temperatures can weaken grain boundaries and cause boundary cracking. Therefore, the rolling temperature is kept 20 to 90°F (10 to 50°C) below the “solidus” or solidification temperature of the matrix alloy.

2.3.1. Behaviour of Al–SiCp Metal Matrix Composites after Successive Hot Rolling

The strength of particulate reinforced MMCs depends on the size of the ceramic particles, inter-particle distance, the volume fraction of the reinforcement, and the micro compositional changes. As a result, thermo-mechanical treatments can alter the composite's properties and the reinforcement characteristics.

During thermomechanical forming processes of MMCs, micro-compositional changes take place causing extensive changes in mechanical properties such as ductility, fracture toughness and stress corrosion resistance. The effect of the termomechanical processing on this factors and consequently on the mechanical properties of the composite has been reported before by Wang, A.*et al* (1996); Taha, M.A. *et al* (2003), and Myriounis, D.P. *et al* (2008).

The nature of the interface between the particulate reinforcement and metallic matrix depends on the processing of the composite. A local concentration gradients around the reinforcement particles can be a consequence of the coefficients of thermal expansion mismatch between the reinforcement and metallic matrix as well as the deformation of the matrix during processing. This concentration gradient is the driving force for the segregation and precipitation at the metallic matrix and reinforcement interface. When impurity atoms move to disordered sites such as the interfaces (grain boundaries), equilibrium segregation takes place. On the other hand, non-equilibrium segregation can occur due to an imbalance in concentration of point defect at the ceramic/metal interface throughout the non-equilibrium processing. The concentration and distribution of these precipitates affect the properties of the composite where the homogenous distribution of small precipitates promote more optimum mechanical properties.

High residual internal stresses and high dislocation densities are the most important features of the microstructure in the Al/SiC composites. Dislocations are created by the difference in coefficients of thermal expansion between the ceramic reinforcement and the metallic matrix. The interaction of these dislocations with the reinforcing particles depends on the reinforcement particle size, spacing, and density. When a particle is incorporated into a matrix, an additional barrier for dislocation movement is created. The dislocation must move by cutting through the particles or by taking a path around the obstacle.

2.3.2. The Effect of Hot Rolling Process on the Void Closure

Due to the liquid processing (shrinkage of aluminium or gas incorporation during solidification) and to the presence of the ceramic particles, heterogeneous nucleation of voids takes place at the particle - matrix interface, leading to a higher porosity when compared to the monolithic alloys (Wang, A. *et al,* 1996). A total avoidance of porosity is challenging, since the lower thermal conductivity of ceramic reinforcements which forces them to be pushed to the solidifying front of the freezing melt, causes shrinkage voids to appear around the ceramic particulate. Poor performance of the MMC in service is typically attributed to porosity remaining after processing. Tekmen *et al.* (2003) have reported how the ultimate tensile and yield strength of the MMCs decrease significantly with the porosity. Hence, it is very advantageous to use the hot rolling process to eliminate voids.

Thermomecanichal processing, such as hot rolling, enhance void closure and welding. At high rolling temperatures, the voids complete closure more quickly. The explanation given by Wang *et al.* (1996) to the faster closure of voids is the rapidly increased diffusion rates. This is a consequence of high temperatures of the metal matrix, allowing the voids' surface to make contact. Consequently, a higher diffusion flux is created between the surfaces in contact. These factors lead to a faster collapse and closure of the voids, and a welding of the surface of the voids. Unwelded voids behave like sharp cracks, which is considered detrimental to the performance.

The rolling process parameters and the position of the preexistent voids relative to the rolling surface, was reported by Wang, A. *et al.* (1996) to affect the void closure rate. It was found that the rate of closure for transverse voids was lower than the rate of closure for longitudinal voids. Closure of voids is a consequence of the hydrostatic pressure and its holding period. The degree of welding for the surface of the voids is favored by shear stresses, which increase the coefficient of friction. Increasing the shear stress and shear strain is possible by increasing the friction between rolls and work piece. When the void was situated at a location near to the rolling surface, it closes quicker and earlier.

Wang *et al.* (1996) and Tanaka *et al* (1986) used a finite element method to conclude that the time integral and the strain of the hydrostatic stress in the area of the void were the governing factors for the closure of voids during rolling. Voids started to close and weld gradually from the edge to the centre. At higher temperatures, of course, the surface of the voids welded more efficintly.

CHAPTER 3: EXPERIMENTAL PROCEDURE

3.1. Materials

The chemical compositions of the composite under study is given in Table 1. The composite materials were supplied in the form of 1.0” slabs from MC-21, Inc (Carson City, Nevada, USA).

Table 1. Matrix Composition (A359 Al 70 % of total volume)

Si	**Fe**	**Cu**	**Mn**	**Mg**	**Zn**	**Sr**	**Al**
8.5-9.5%	0.2% max	0.2% max	0.1% max	0.45-0.65% max	0.2% max	0.05% max	Bal.

For the microstructural analysis of Al-A359 / 30 vol.% SiC_P composites as a function of hot rolling, seven different plates were examined for microstructural analysis with the processing history listed in Table 2.

Table 2. Al-A359 / 30 vol.% SiC_P composites examined in this study.

Plate #	**Thickness**	**Thickness Reduction**	**Relative Reduction**	**Manufacturing Process**
1	1.0”	0%	0%	As-cast
2	0.364”	64%	64%	Hot rolled, surface bead blasted
3	0.250”	75%	31%	Hot rolled
4	0.122”A	88%	51%	Hot rolled
5	0.122”B	88%	51%	Hot rolled, different processing conditions compared to A
6	0.038”A	96%	69%	Hot rolled
7	0.038”B	96%	69%	Hot rolled, 2 directions, 90° offset

The plates were sectioned with a low speed diamond saw and specimens were identified as given in Figure 12 below for materials characterization. Figure 12 presents the geometry of the samples and the corresponding identification.

- CRP: center-rolling plane
- MRP: middle-rolling plane
- ERP: edge-rolling plane
- CL: center-longitudinal section
- ML: middle-longitudinal section
- EL: edge-longitudinal section
- CT: center-transverse section
- MT: middle-transverse section
- ET: edge-transverse section

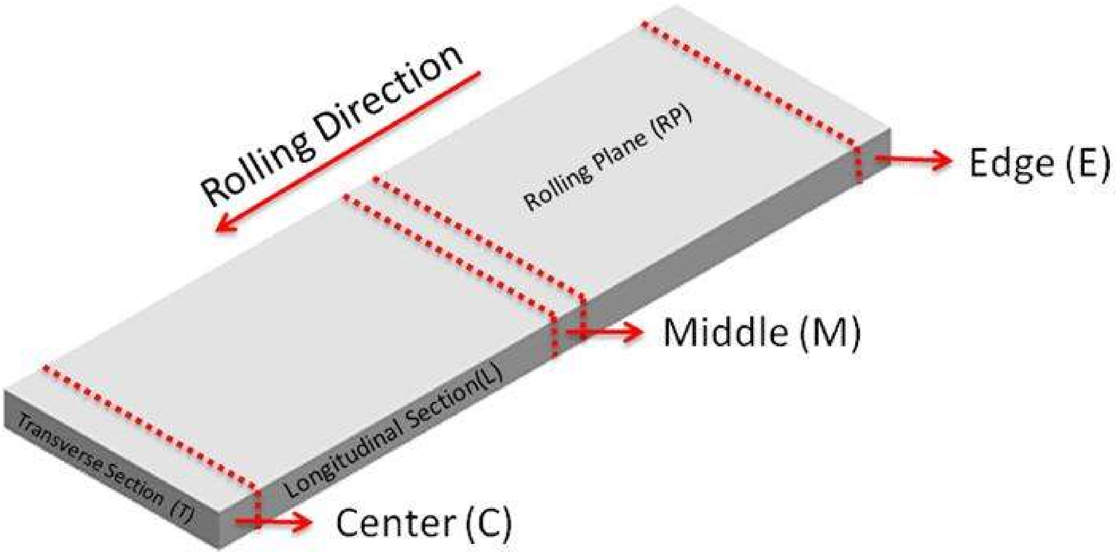

Figure 12. Sectioning and metallographic preparation of Al-A359 / 30 vol.% SiC_P composites.

To study the effect of annealing on the as-cast microstructure (i.e., spheroidization Study), thirteen as-cast samples were sectioned with 5x5x5mm dimensions.

Four different samples with different compositions identified as A, B, C, and D were examined for the high strain rate deformation of the MMCs study. These composites were tested under high strain rates at different conditions. The samples were initially sectioned with a water jet to avoid exposure to high temperature that might occur during conventional sectioning. These cuts were sub-sectioned by a low speed diamond saw with oil-based lubricant, again to minimize exposure to high temperature. The deformed area was sectioned in two parts. One side was set aside for fracture study. Simultaneously, two samples were prepared for cross-sectioned metallographic study. Several photographs taken during the sample preparation of the high strain rate damaged composites are presented in Figure 13 for clarification.

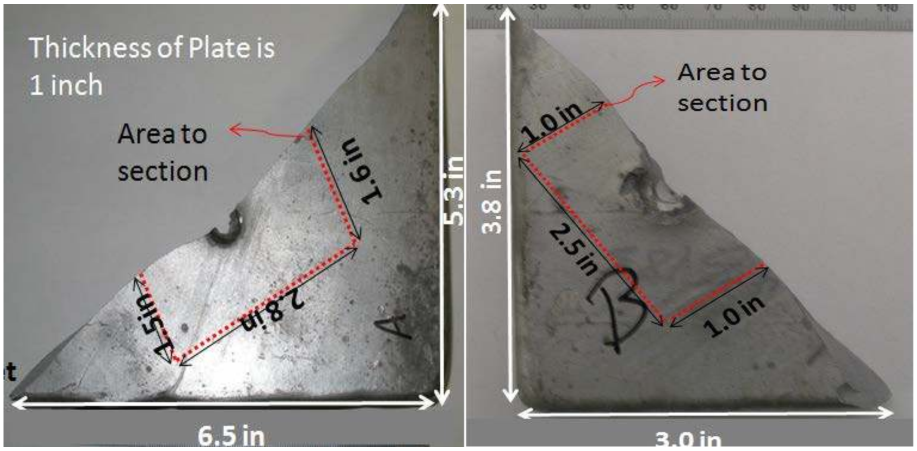

(a)

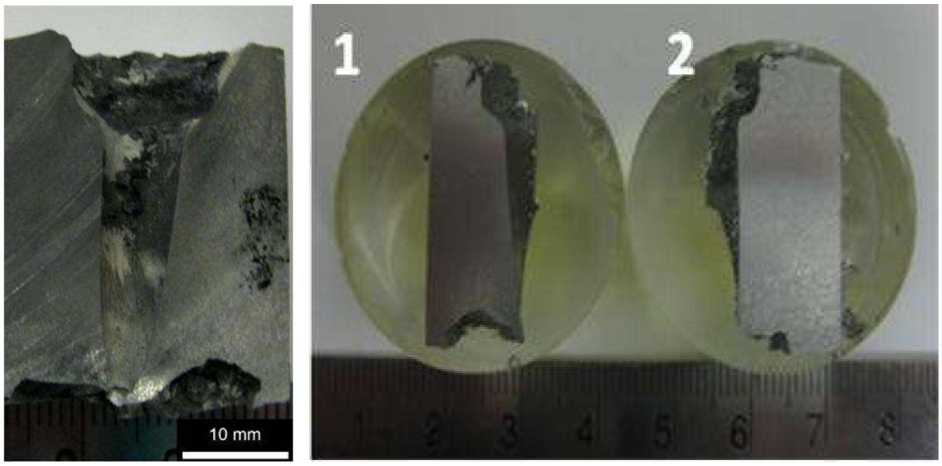

(b)

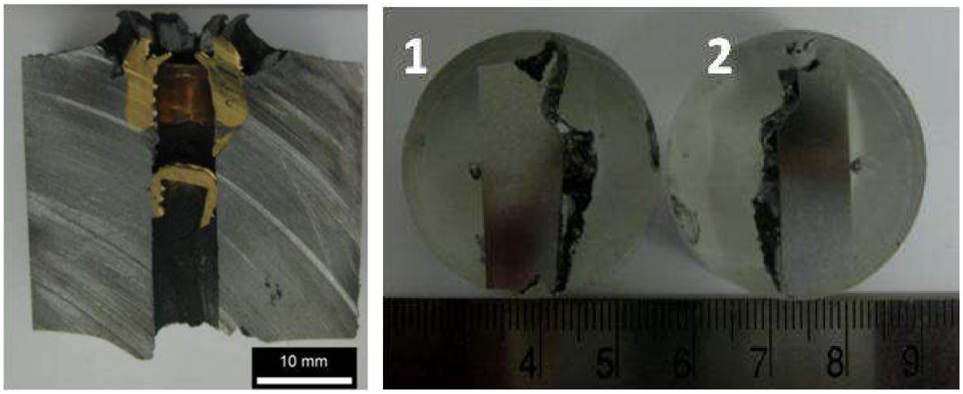

(c)

Figure 13. Photographs illustrating sample preparation for the high strain rate deformation study: (a) water-jet sectioned samples A and B; (b) sectioned, mounted and polished sample C; and (c) sectioned, mounted and polished sample D.

3.2. Heat Treatment

For the experimental investigation on microstructural changes of Al-A359 / 30 vol.% SiCp with thermal annealing, a furnace with quenching facility was used to investigate high temperature silicon morphology evolution. Small cubes of the MMC with dimensions 5x5x5mm were placed in the furnace, annealed isothermally up to 470°C, 538°C, and 570°C, and held for 15min, 30 min, 60 min, 120 min. After annealing at the different times and temperatures, the samples were finally quenched in oil.

3.3. Microstructure Analysis

3.3.1. Metallography

Samples were obtained for metallographic observation at the following conditions: as-cast , hot rolled , heat treated and failed after high strain rate.

The samples were ground and polished using the following steps:

1. Grinding the cut samples with SiC paper as follow
   - ✓ 240 grit - 2 min- 30N, 150 rpm
   - ✓ 120 grit - 2 min- 30N, 150 rpm
   - ✓ 600 grit - 2 min-30N, 150 rpm
   - ✓ 800 grit - 1 min -30 N, 150 rpm
2. Polishing the samples with diamond suspension as follow
   - ✓ 9 µm - 10 min - 35N, 150 rpm
   - ✓ 9 µm - 5 min - 30N, 150 rpm
   - ✓ 9 µm - 5 min - 25N, 150 rpm
   - ✓ 3 µm - 5 min - 20N, 150 rpm
   - ✓ 3 µm - 5 min - 20N, 150 rpm
   - ✓ 1 µm - 5 min- 10N, 150 rpm
3. Colloidal silica with water for 2 min.

A modified Kellers reagent was used to etch the samples with a composition of 2 ml HF (48%) 9ml HCL(conc) , 6 ml HNO_3(conc) and 183 ml H_2O for 35 seconds.

3.3.2. X-ray diffraction (XRD)

X-ray diffraction (XRD) studies were performed on the successive rolled samples to examine the possible development of textures during thermomechanical processing. XRD studies were also performed on the high strain rate tested sample D which showed a different MMC composition. These measurements were carry out by using a Rigaku D-Max B Diffractometer using Cu-Kα radiation. XRD patterns were indexed based on JCPDS resources using MDI Jade software.

3.3.3. Microscopy

The polished and etched samples as well as the fracture surfaces were examined using a laser confocal microscope Olympus Lext-OLS3000IR (CM). Scanning electron microscopy (SEM) micrographs and energy dispersive X-rays (EDX) analysis was also carried out using a Zeiss Ultra-55 FEG Scanning Electron Microscope (SEM) at a voltage of 20 keV. For chemical analysis with EDX of phases, selected measurements at specific points and mapping were taken.

Transmission electron microscopy (TEM) and X-ray energy dispersive spectroscopy (XEDS) images using FEI Technai F30 were taken from selected rolled samples using bright, dark field imaging (weak beam) and high angle annular dark field imaging (HAADF) as well as electron diffraction.

3.3.4. Image Analysis and Statistical Approach

In order to study the effect of successive hot rolling on the particles of SiC, nine (CRP, MRP, ERP, CL,ML, EL, CT, MT, and ET) different optical micrographs were obtained and processed with an image analysis software named, IQ-Materials. The data was analyzed with a statistical sample of more than 300 particles per plate. Particle size and inter-particle distance measurements were performed. The uniformity of SiC particle distribution was quantified by measuring the inter-particle distance and the coefficient of variation (C_V). The inter-particle distance is defined by the shortest distance between particles, and the coefficient of variation was determined by $C_V = \sigma/\mu$ where σ is the standard deviation of inter-particle distance and μ is the mean inter-particle distance. The coefficient of variation (C_V) is a normalized measure of the dispersion of the particles distribution (e.g., measure of uniformity). A higher value represents less uniformity in the distribution.

For the Si morphology evolution study, SEM pictures were taken at magnifications of 300x, 500x and 1000x, and analyzed by IQ Materials. The presented are mean values of six different fields at a constant magnification (1000x) with about 70 silicon particles each measured by image analysis .

3.4. Hardness Test

Hardness data was recorded for each rolled sample using a Leco Vickers Hardner Tester LV 700. Vicker Hardness (**HV**) was measured on the samples before metallographic preparation with the samples slightly ground. An average hardness was determined based on ten readings using 20 kgf for each sample.

CHAPTER 4: RESULTS AND DISCUSSION

4.1. Characterization of Al-A359 / 30 vol.% SiCp Composite

The MMCs examined in this study had an alloy matrix composed by aluminium, silicon, and magnesium (A359) reinforced with silicon carbide particles. The alloying composition of the A359 matrix in wt.% is (8.5-9.5) Si – 0.2 Fe – 0.2 Cu – 0.1 Mn – (0.45-0.65) Mg – 0.2 Zn – 0.05 Sr, balanced by Al. The microstructure of the composite has three main phases as presented in Figure 14. They are aluminum matrix (grey area), SiC particles (dark area), and the eutectic region of aluminum and silicon (white area).

In the as-cast microstructure, the SiC particles are located in the eutectic region presumably due to the solidification mechanism where the SiC particles are pushed to the solidification front and then segregated in the interdendritic eutectic region. Furthermore, in the as-cast microstructure, Si is segregated in the interdendritic region with eutectic morphology as presented in Figure 14 (a). However with hot-rolling, the lamellar structure of Al-Si eutectic breaks up, and Si becomes spherical in morphology as presented in Figure 14 (b). This is most likely driven by mechanical strain energy and thermal energy via interfacial diffusion.

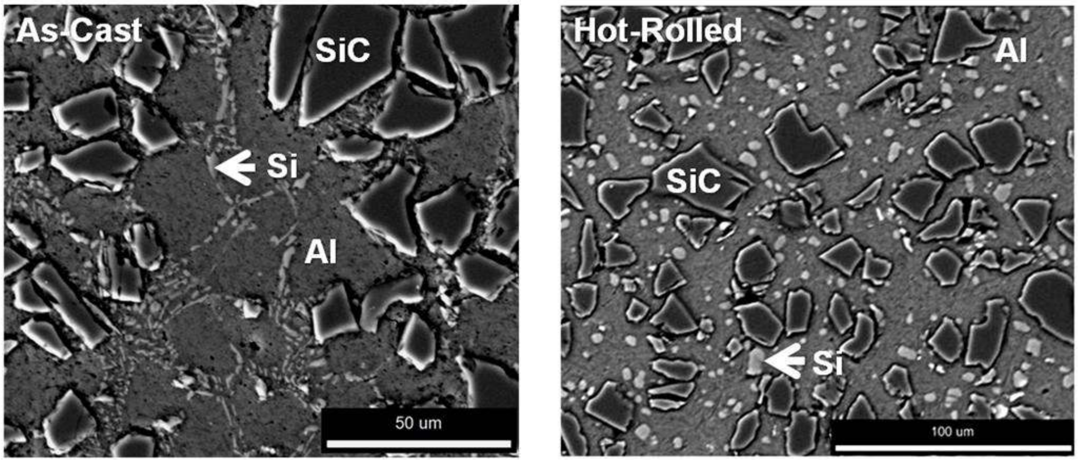

(a) (b)

Figure 14. Backscatter electron micrographs of (a) as-cast and (b) hot-rolled composites.

Aside from basic microstructure analyses, extensive XRD investigation was carried out to determine the phase constituents of the composites. Figure 15 and Figure 16 presents typical XRD patterns from composites, and they confirm the presence of fcc-Al, α-SiC and Si as the major constituents. No apparent crystallographic texture was observed with the successive hot-rolling regardless of sample, location and orientation.

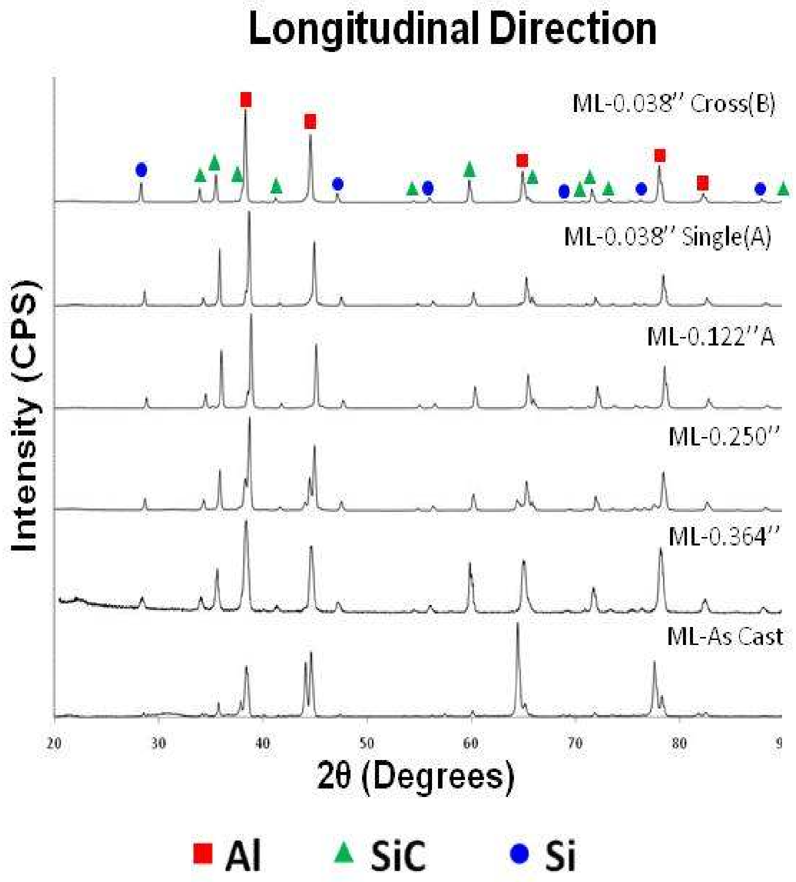

Figure 15. XRD patterns from composites examined in the longitudinal direction.

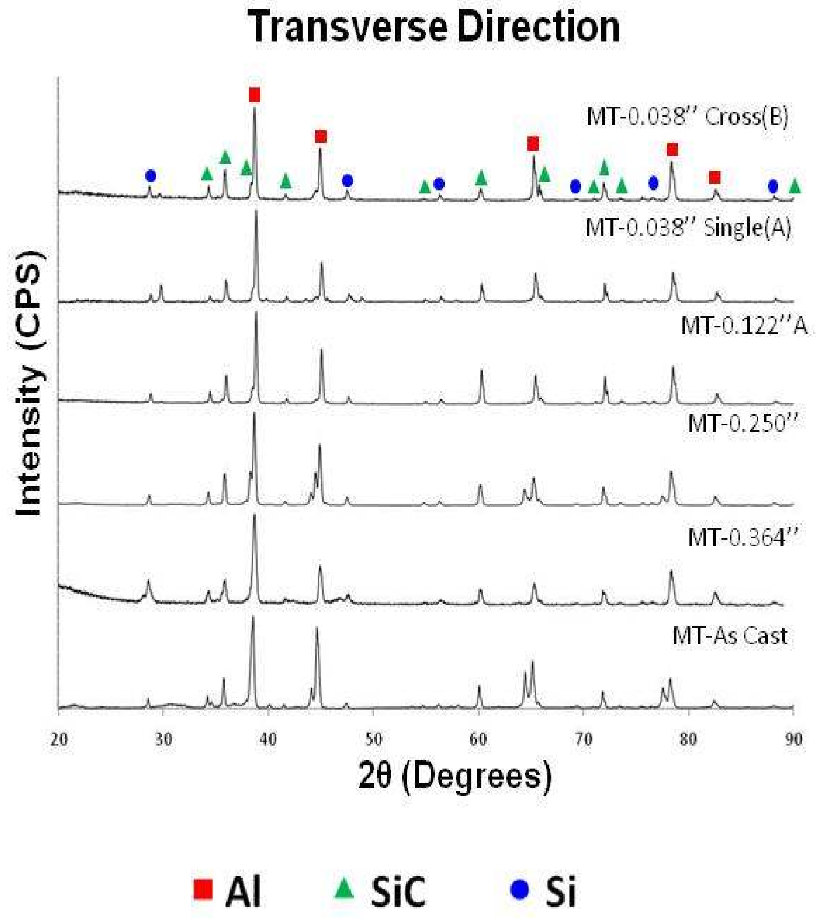

Figure 16. XRD patterns from composites examined in the transverse direction.

In general, TEM examination (HR-TEM and BF images) of composites showed excellent bonding between all phase constituents. Figure 17 (a) and Figure 17 (b) show the HR-TEM micrographs of interface between Al matrix and SiC reinforcement in the as-cast and hot-rolled composites respectively. Excellent bonding was observed without any significant segregated phases at this interface, although a small amount of Mg_2Si and $MgAl_2O_4$ was observed (See Section 4.1.1.) Figure 17 (c) shows the interface between Al and Si eutectic. This interface again was very clean although minor amounts of precipitates and dispersoids were observed at the Al-Si interfaces (See Section 4.1.1.).

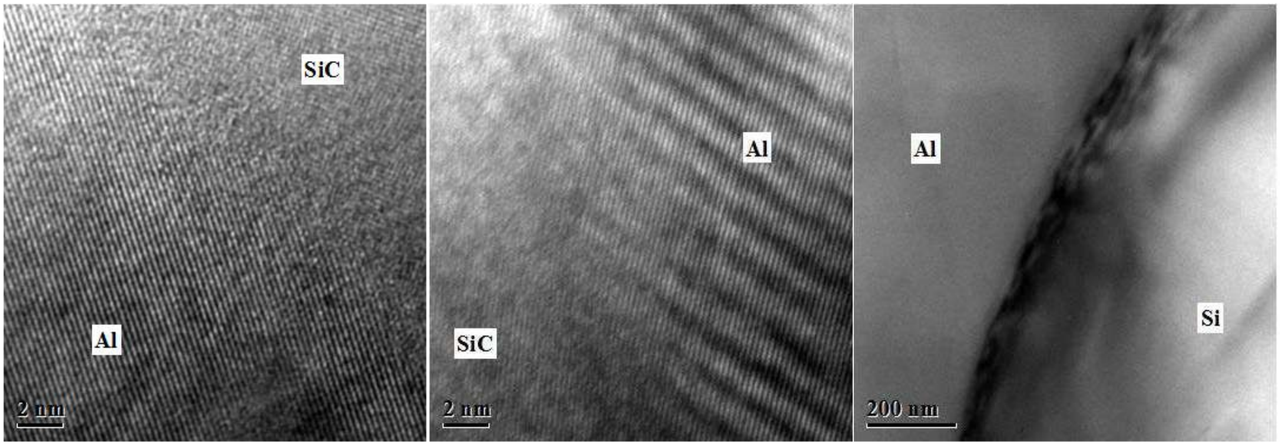

Figure 17. TEM micrographs from the interface of (a) Al-SiC in as-cast composite, (b) Al-SiC in hot-rolled composite (0.038"B), and (c) Al-Si interface in hot-rolled composite (0.122"A).

4.1.1. Minor Constituent Phases: Precipitates and Dispersoids

From microstructural analyses by SEM and TEM, several different precipitates and/or dispersoids were observed as presented in Figure 18, Figure 19, and Figure 20. They were in general rich in Mn, Mg, Cu, and Fe, and frequently located at the Al-SiC, Al-Si interfaces, although many (e.g., Mg_2Si, Al_2Cu, and $MnSi_2$, Al-Fe-Si and Fe-Mg-Al-Si) were observed within the fcc-Al matrix. Typically, Mg is added to the Al–Si alloy for age hardening through the precipitation of Mg_2Si phase.

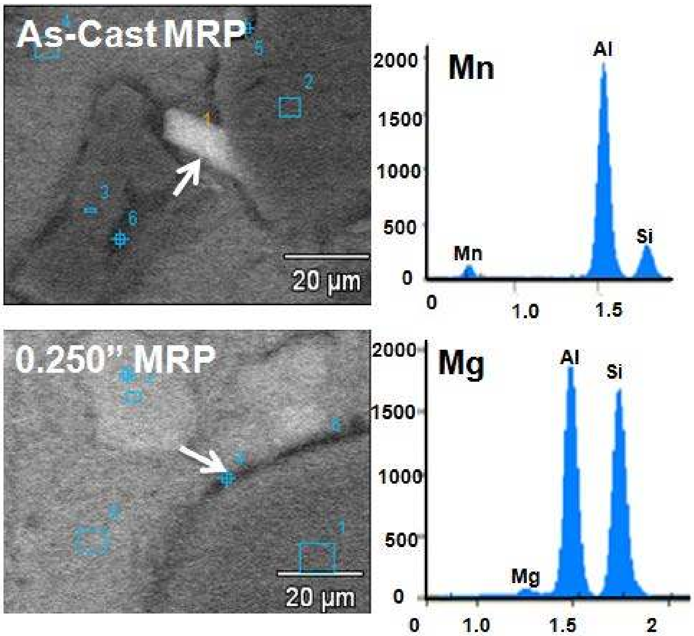

Figure 18. Typical Mn- and Mg-rich precipitates and dispersoids observed by SEM and XEDS.

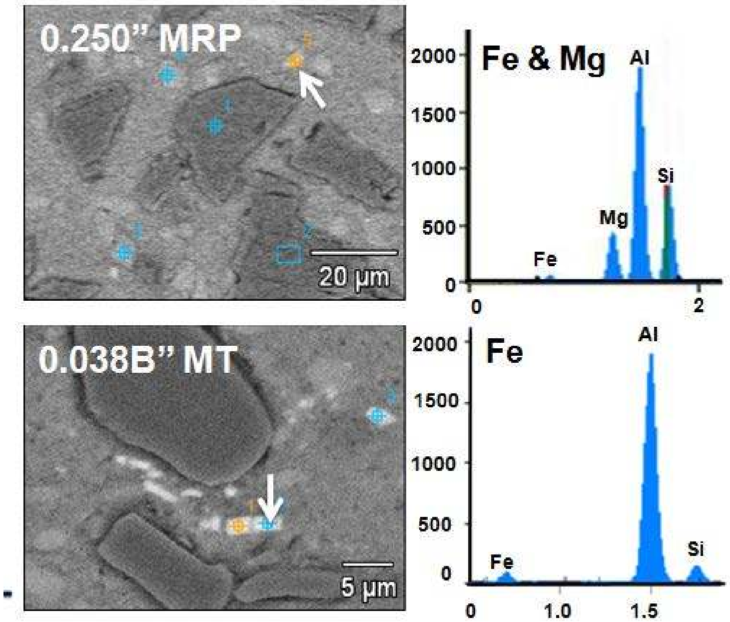

Figure 19.Typical Fe-rich precipitates and dispersoids observed by SEM and XEDS.

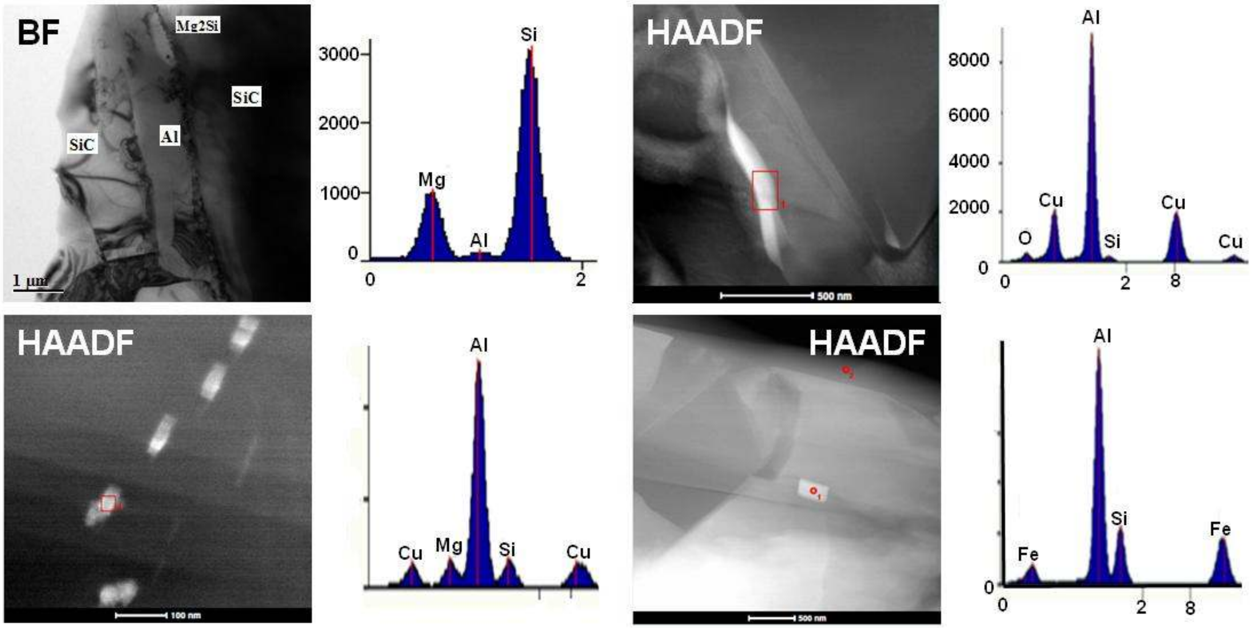

Figure 20. Typical precipitates and dispersoids observed by TEM and XEDS including Mg_2Si at the Al/SiC interface, edge-on oriented precipitates in the Al matrix, and Al_2Cu and Fe-Al-Si-rich precipitates.

Magnesium aluminate (cubic spinel), $MgAl_2O_4$, was also found at the Al-SiC interface as presented in Figure 21. The presence of $MgAl_2O_4$ is a result of the magnesium reaction with SiO_2 at the surface of SiC. The layers of $MgAl_2O_4$ can protect the SiC particles from the liquid aluminium during production and are very likely to influence the interface properties and overall composite behavior. This layer of spinel had a clean bonding with the Al and SiC_p. The presence of Al_4C_3 could not be identified by XRD, SEM and TEM.

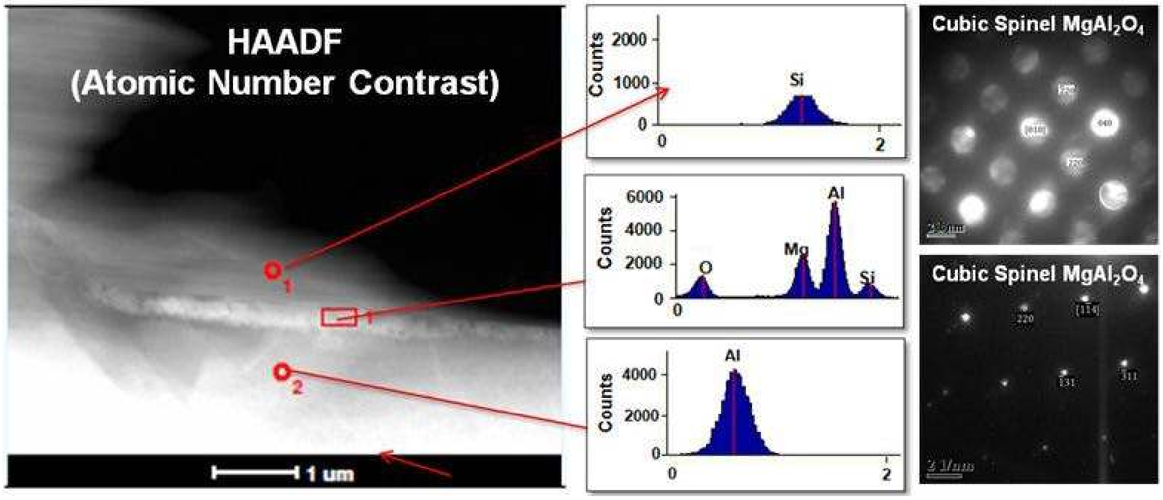

Figure 21. $MgAl_2O_4$ observed at the Al-SiC interface.

4.2. Microstructural Changes of Al-A359 / 30 vol.% SiCp With Thermal Annealing

4.2.1. Morphological Evolution of Si with Thermal Annealing at 470°C, 538°C and 570°C.

Morphological evolution of the eutectic Si during the annealing heat treatment at different times and temperature is presented in Figure 22, Figure 23 and Figure 24.

Figure 22 presents some degree of spheroidization of the silicon after 15 min and before 120 min. A complete spheroidization was not observed at 470°C. Disintegration of Si is observed after 15 min, followed by subsequent silicon particles growth and agglomeration forming large interconnected silicon nets. This is a consequence of Ostwald ripening, larger particles grow by merging with the smaller ones. Ostwald ripening is described by a correlation between diameter of the Si particles and the annealing time as:

$$D_{Si} \approx t^{\frac{1}{3}} \tag{29}$$

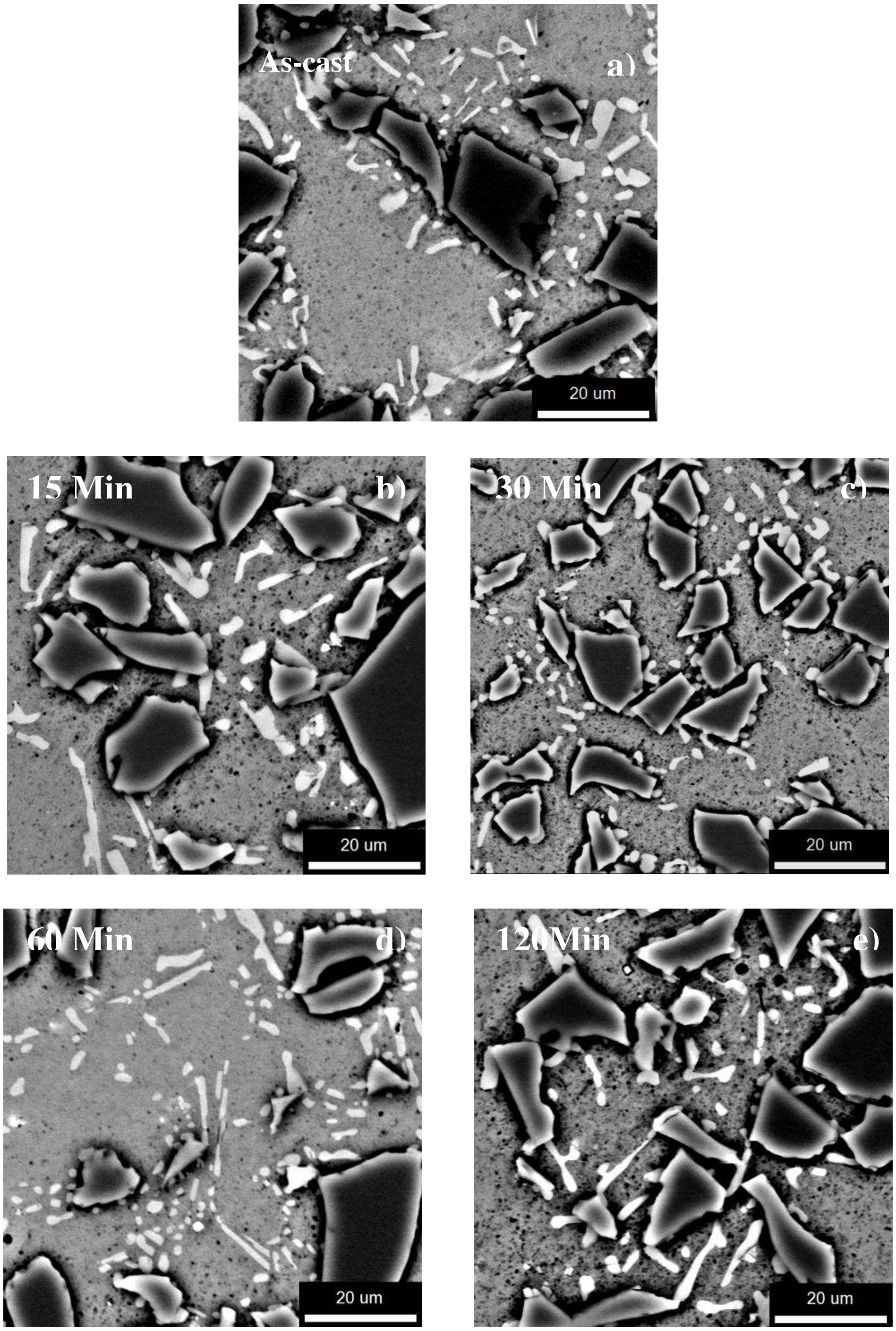

Figure 22. Evolution of eutectic Si after 15min, 30 min, 60 min and 120 min at 470°C.

Si break-up from the as-cast morphology after 15 min is evident in Figure 23, a. At 538°C, between 15 min and 30 min, some agglomeration and growth of the Si is observed. A interconnected silicon phase is observed at this stage. Spheroidization is observed between 30 min and 60 min with growth of silicon particles and Al grains. Ostwald ripening of the spheroidized Si particles was observed by microstructural analysis.

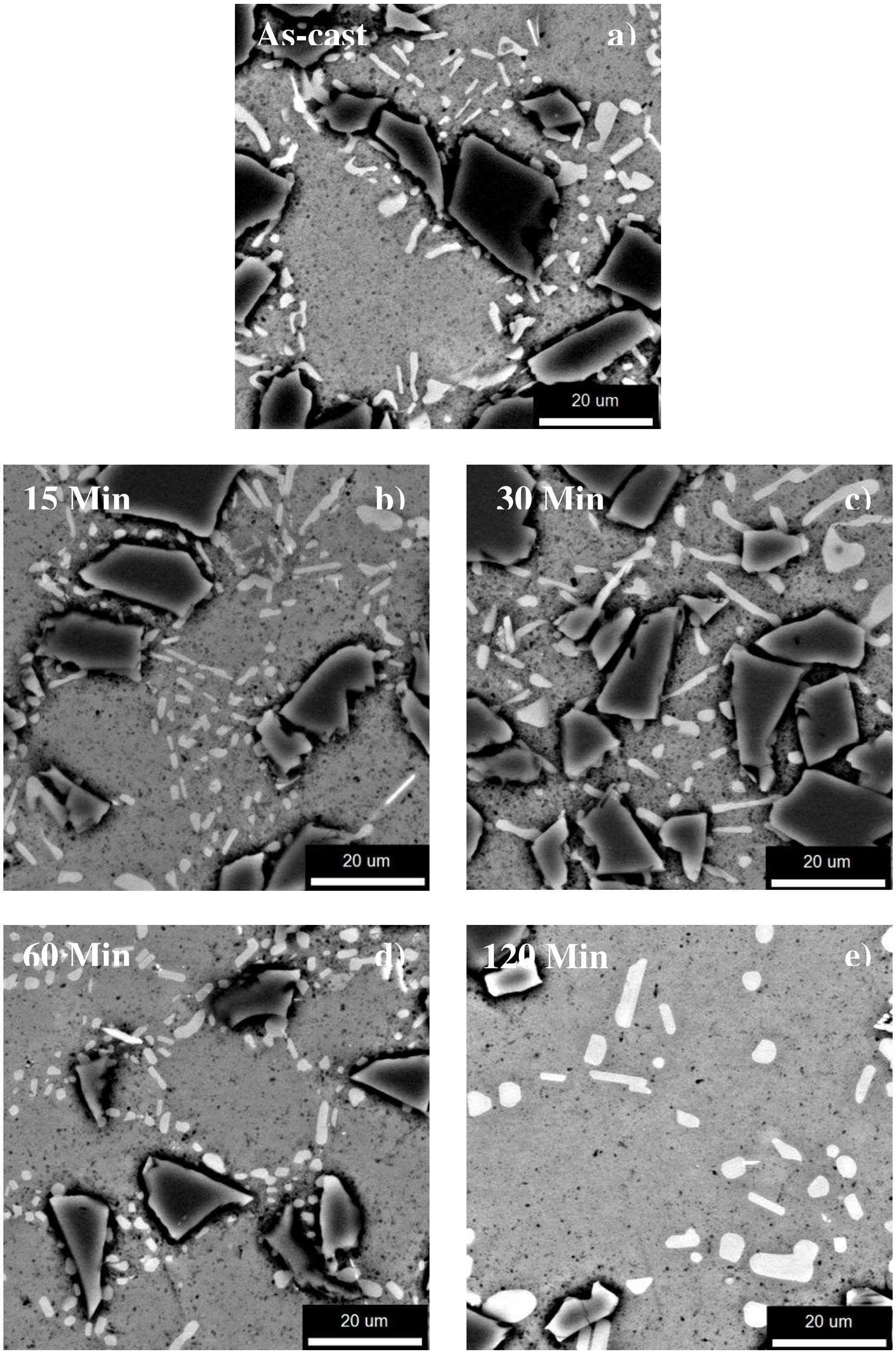

Figure 23. Evolution of eutectic Si after 15min, 30 min, 60 min and 120 min at 538°C.

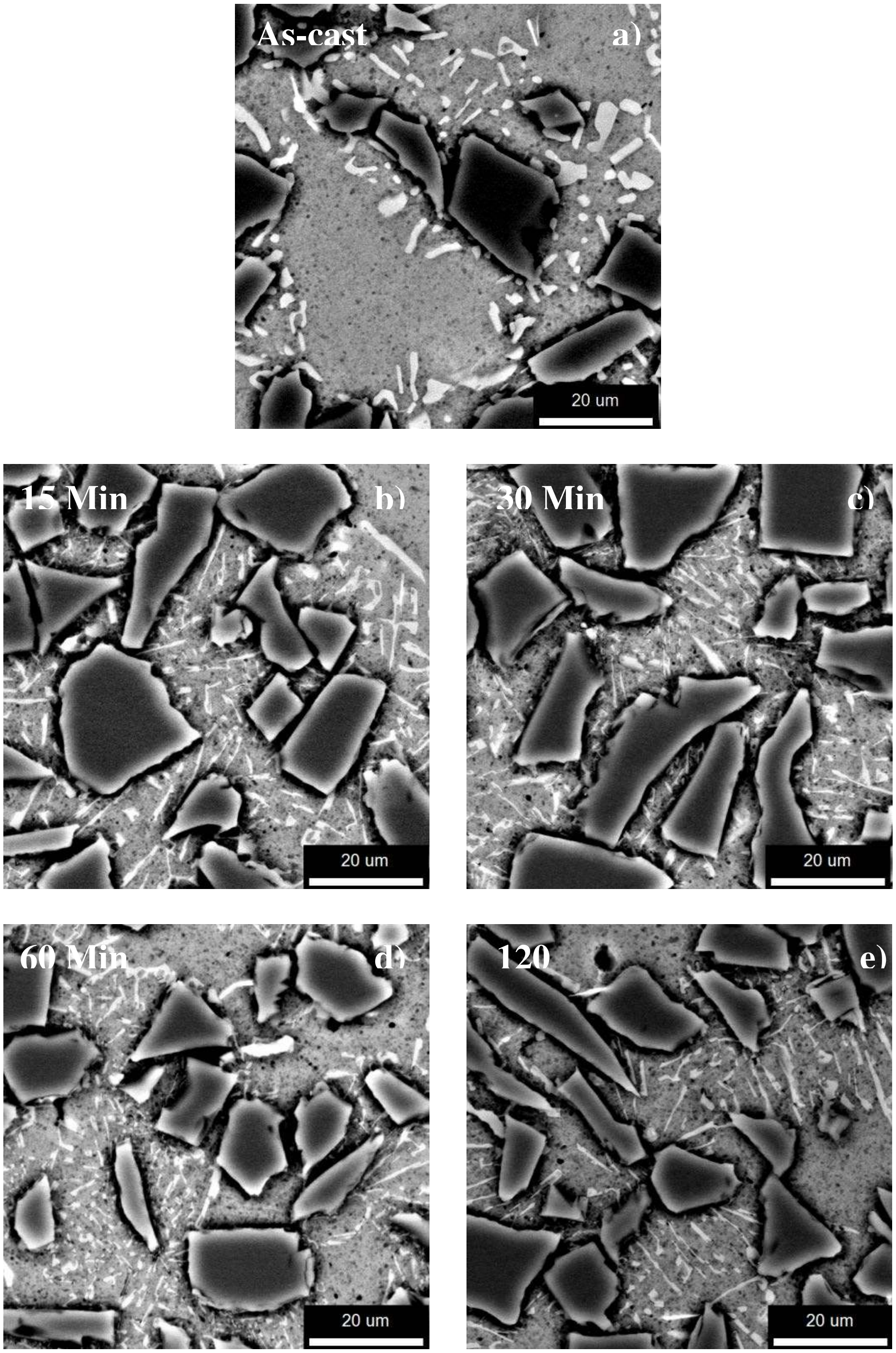

Figure 24. Evolution of eutectic Si after 15min, 30 min, 60 min and 120 min at 570°C.

At 570°C as shown in Figure 24, partial melting of the alloy was observed. Some viscoplastic behavior was evident after taking the samples out of the furnace. Silicon transformation into eutectic silicon platelets was evident after treating at this temperature. No spheroidization observed.

4.2.2. Microstructural Parameters

The following parameters were used for quantitative microstructural analysis of the silicon particles in the eutectic region. These parameters were measure for samples annealed at 470 and 538°C. Because melting was evident at 570°C, quantitative analyses were not carried out. The measurements were performed by image analysis using SEM micrographs with the software IQ materials.

Mean area of silicon particles was measured to describe the morphology as:

$$\overline{A}_{Si} = \frac{1}{n}\sum_{i=1}^{n} A_{Si} \tag{30}$$

where $\bar{A}_{Si}$ denotes the mean area of silicon particles of one measured micrograph with n as number of measured micrographs.

In Figure 25, $\bar{A}_{Si}$ decreases with time of anneal from the as-cast condition up to 60 min at 538°C. This is due to a reduction of the mean area of the particles, that is spheroidization. Faster disintegration is observed at 538°C due to an increase in the diffusion coefficient of silicon at the Si-Al interface. After 60 min at 538°C, an increase in the mean area is observed due to Ostwald ripening, larger particles grow at the expense of the smaller particles. Ostwald ripening is not observed at 470°C even after 120 min of anneal.

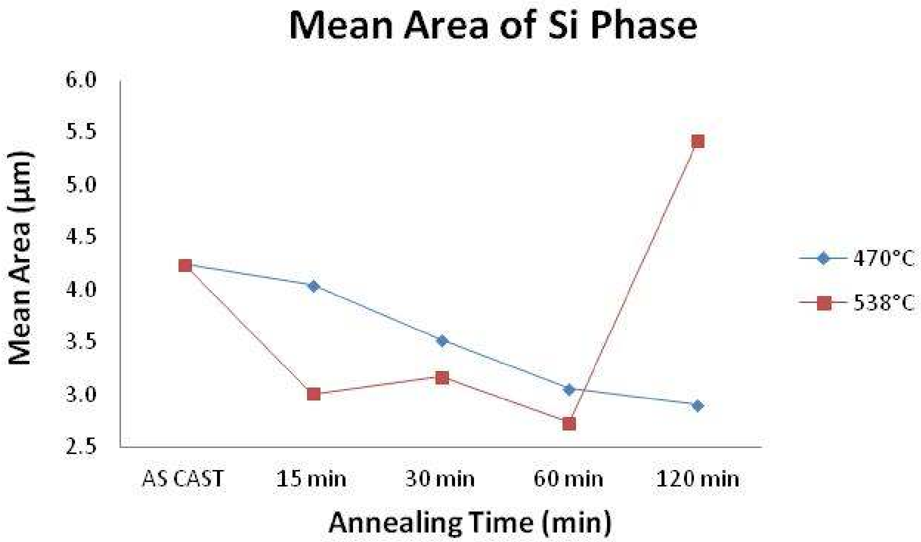

Figure 25. Change of eutectic silicon's mean area with annealing time and temperature.

Width is defined as the greatest point-to-point distance inside each particle that intersects the length line at an angle greater than 45^{o}. In Figure 26, a decrease in the mean width of the Si phase after the annealed temperature of 470°C and 538°C, is observed due to disintegration. At 538°C, an increase in the mean Si width is observed after 60 min, which is consistent with the mean trend observed for the area measurements.

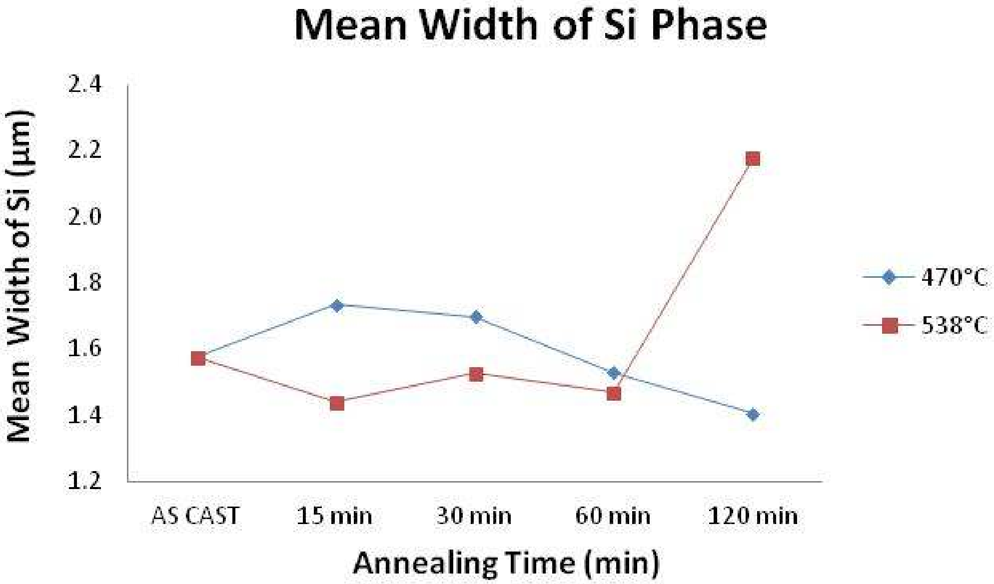

Figure 26. Change of eutectic silicon's mean width (diameter) with annealing time and temperature.

Mean interparticle distance is defined as:

$$\overline{d}_{Si} = \frac{1}{n}\sum_{i=1}^{n}\sqrt{\frac{A_{square}}{N_{Si}}} \tag{31}$$

with A_{square} as a squared value of measured area in the eutectic phase and n is the number of measured micrographs. From Figure 27, it is observed how the mean Si interparticle distance is reduced at any temperature before 30 min due to particle disintegration. At 538°C the interparticle distance fluctuates due to the growth of the particles at the expenses of the others.

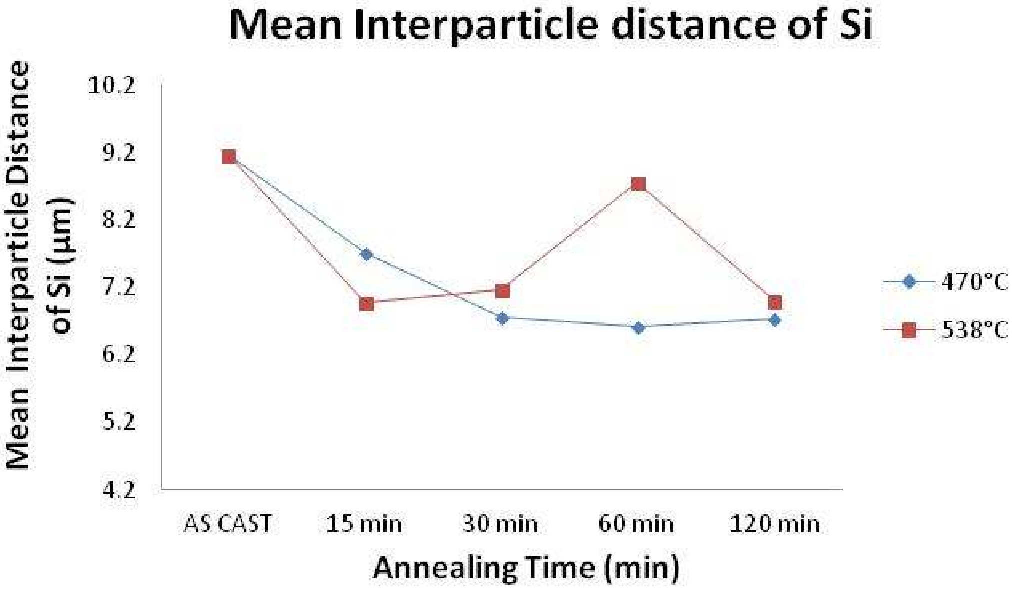

Figure 27. Change of eutectic silicon's mean interparticle distance with annealing time and temperature.

Mean spheroidization density is described as:

$$\overline{\varepsilon}_{Si} = \frac{1}{n}\sum_{i=1}^{n}\frac{N_{Si}}{A}\times 100 \tag{32}$$

where N_{Si} describes the number of silicon particles counted in a reference area, A. The number of measured pictures is n. The values of $\overline{\varepsilon}_{Si}$ are standardized for an area of 100 µm^2 in this study.

Consistent with other measurements, the mean spheroidization density increased at all times at 470°C. However at 538°C, a decrease in the spheroidization density is observed after 30 min, as presented in Figure 28.

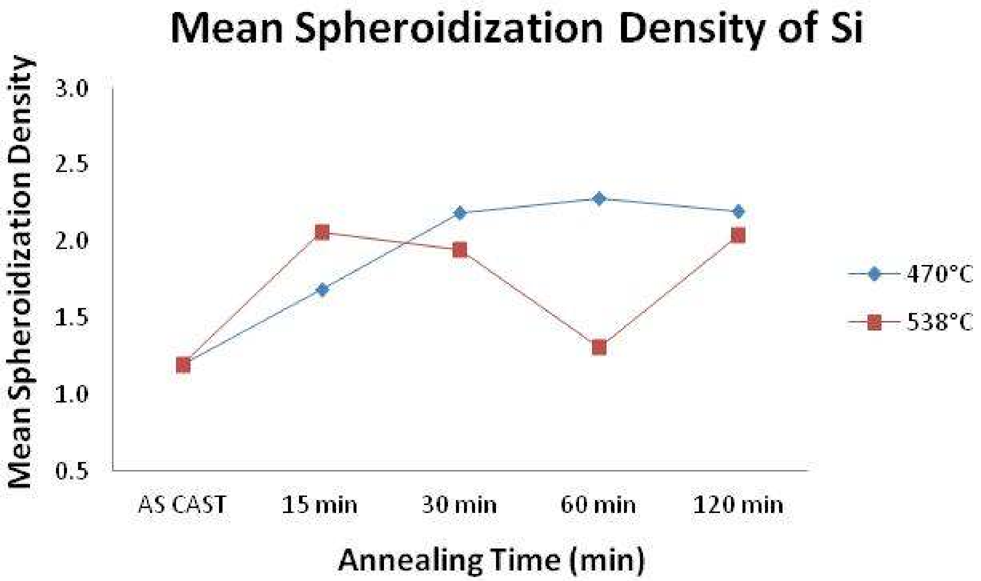

Figure 28. Change of eutectic silicon's mean spheroidization density with annealing time and temperature

The circularity of the Si particles is a parameter used to measure the extent of spheroidization. This is also known as the shape factor described by:

$$\bar{f}_{circ} = \frac{1}{n}\sum_{i=1}^{n}\frac{P_{Si}^{2}}{4\pi A_{Si}} \tag{33}$$

where P_{Si} is the perimeter of the measured Si particles. The shape factor value, $\bar{f}_{circ}$, will be 1, if the particles are circular and less than 1 if it deviates from the circular shape. Figure 29 demonstrates that the shape factors are closer to 1 for the samples annealed at 538°C. This is consistent with the microstructural observation where the spheroidization was more clearly observed in the samples annealed at 538°C. The shape factor shows the higher degree of spheroidization after 15 min, which means that the eutectic Si tends to spheroidize after 15 min.

At 538°C, the Si tends to grow after 60 min losing the spherical shape. Because slower spheroidization due to a lower diffusion coefficient is observed at lower temperatures, the maximum spheroidization is not reached even after 30 min at 470°C.

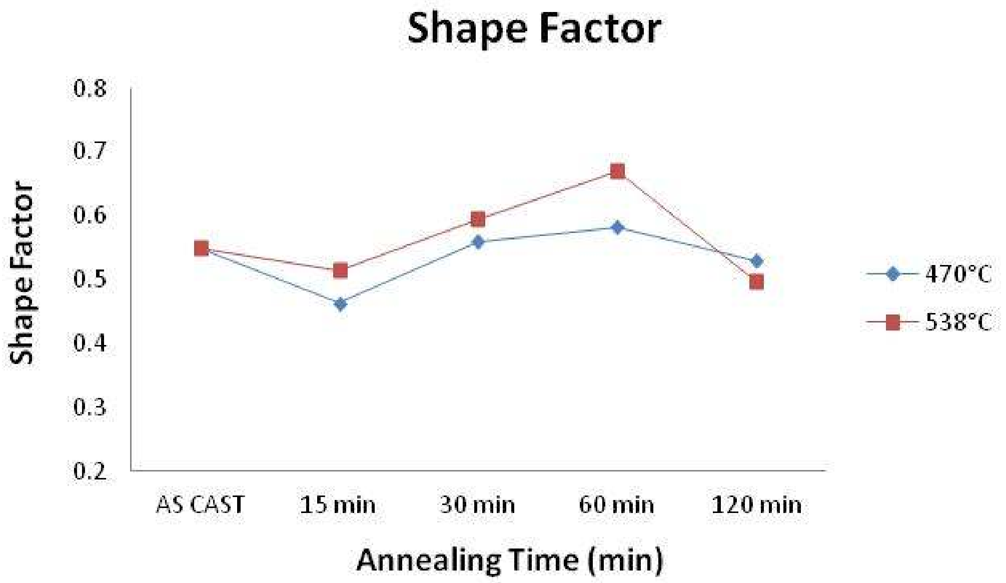

Figure 29. Change of eutectic silicon's shape factor with annealing time and temperature.

Changes of the silicon‘s morphology were observed after 15 minutes of annealing at 470°C and 538°C. The edges of the silicon were rounded and spheroidized. At higher temperatures (538°C) the disintegration, spheroidization, and growing started all at an earlier stage.

4.2.3. Results using the Model of Silicon Spheroidization (Ogris *et al*, 2002)

The original radius of the silicon in its cylindrical form in the as-cast condition have been calculated by image analysis, and is approximated to be 0.787 μm, 0.787 x 10^{-6}m. The annealing temperatures experimentally tested and presented above are 470°C (743 K), 538°C (811 K) and 570°C (843 K).

The disintegration time, $\tau_{\max}$, for a cylinder of Si from the as-cast morphology was calculated using Ogris mode. It is assumed that a maximum growth fluctuation amplitude as assumed in the model by Ogris. The activation energy for Si-Al interdiffusion, frequency factor, interfacial energy of Al-Si interface, atomic diameter of Si, and activation energy for formation of vacancies in Al have been reported previously by Fujikawa *et al* (1978) and Ogris *et al* (2002).

At 470°C:

$$D_{s@470^{\circ}C} = D_0 \cdot \exp\left(-\frac{E_{A,\mathrm{inter}} - E_{A,v}}{R \cdot T}\right) = 2.29\times10^{-4}\left(\frac{m^2}{s}\right)\cdot \exp\left(\frac{-148.6\left(\frac{KJ}{mol}\right)+74.3\left(\frac{KJ}{mol}\right)}{8.314\left(\frac{J}{mol\cdot K}\right)\cdot 743K \cdot \left(\frac{1KJ}{1000J}\right)}\right) = 1.368\times10^{-9}\,\frac{m^2}{s} \tag{34}$$

$$\tau_{\max@470^{\circ}C} = \frac{32\pi^2}{9}\cdot\frac{kT}{D_s\gamma}\cdot\left(\frac{\rho}{\phi}\right)^4\cdot\ln\frac{\rho}{\phi} = \frac{32\pi^2}{9}\cdot\frac{1.38\times10^{-23}\left(\frac{J}{K}\right)\cdot 743(K)}{1.368\times10^{-9}\left(\frac{m^2}{s}\right)\cdot 1\left(\frac{J}{m^2}\right)}\cdot\left(\frac{0.787\times10^{-6}(m)}{2.22\times10^{-10}(m)}\right)^4\cdot\ln\left(\frac{0.787\times10^{-6}(m)}{2.22\times10^{-10}(m)}\right) \tag{35}$$

$$\tau_{\max@470^{\circ}C} = 339{,}527s = 94.31hr \tag{36}$$

and 538°C:

$$D_{s@538^{\circ}C} = D_0 \cdot \exp\left(-\frac{E_{A,\mathrm{inter}} - E_{A,v}}{R \cdot T}\right) = 2.29\times10^{-4}\left(\frac{m^2}{s}\right)\cdot \exp\left(\frac{-148.6\left(\frac{KJ}{mol}\right)+74.3\left(\frac{KJ}{mol}\right)}{8.314\left(\frac{J}{mol\cdot K}\right)\cdot 811K \cdot \left(\frac{1KJ}{1000J}\right)}\right) = 3.751\times10^{-9}\,\frac{m^2}{s} \tag{37}$$

$$\tau_{\max@\,538^{\circ}C} = \frac{32\pi^2}{9}\cdot\frac{kT}{D_s\gamma}\cdot\left(\frac{\rho}{\phi}\right)^4\cdot\ln\frac{\rho}{\phi} = \frac{32\pi^2}{9}\cdot\frac{1.38\times10^{-23}\left(\frac{J}{K}\right)\cdot 811(K)}{3.751\times10^{-9}\left(\frac{m^2}{s}\right)\cdot 1\left(\frac{J}{m^2}\right)}\cdot\left(\frac{0.787\times10^{-6}(m)}{2.22\times10^{-10}(m)}\right)^4\cdot\ln\left(\frac{0.787\times10^{-6}(m)}{2.22\times10^{-10}(m)}\right) \tag{38}$$

$$\tau_{\max 538^{\circ}C} = 135{,}159s = 37.54hr \tag{39}$$

4.3. Microstructural Changes With Thermo-Mechanical Processing

A lamellae microstructure (Al-Si eutectic), observed in as-cast matrix, clearly evolves into spherical morphology with successive rolling. Obviously this is a thermodynamically driven (i.e., reduction of surface area/energy), and thermally activated during hot-rolling (interphase boundary diffusion) with additional activation provided by mechanical strain. Optical micrographs presented in Figure 30 demonstrate the evolutionary morphological changes as a function of successive hot-rolling. During hot rolling (538°C), spheroidization is occurring due to the mechanisms explained in previous sections.

In addition, while a lamellae structure of Si in Al-Si eutectic was consistently located at the Al/SiC interface, uniformly distributed spherical Si was observed after hot-rolling mostly within the fcc-Al matrix as presented in Figure 31. This observation is consistent in both SEM and TEM findings. Other microstructural features identified in the Al-Si matrix after hot rolling is the high dislocation density within the Al particularly around SiC particles shown in Figure 32 (a) and twins within the Si phase as shown in Figure 32 (b). Both should be a consequence of the plastic deformation that has occurred during successive rolling.

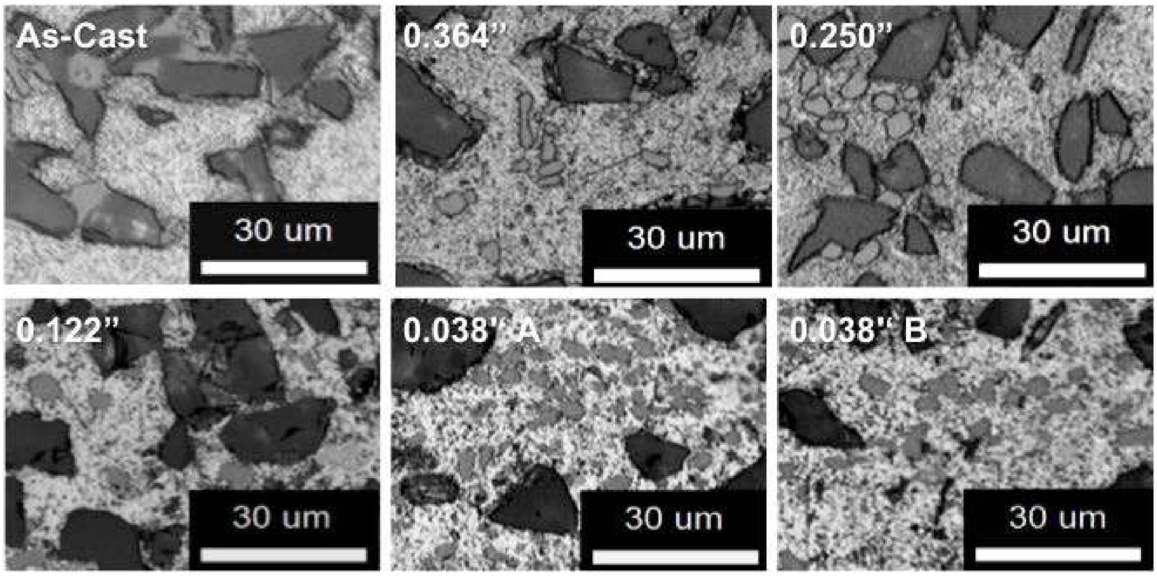

Figure 30. Evolution of Si morphology as a function of successive hot-rolling.

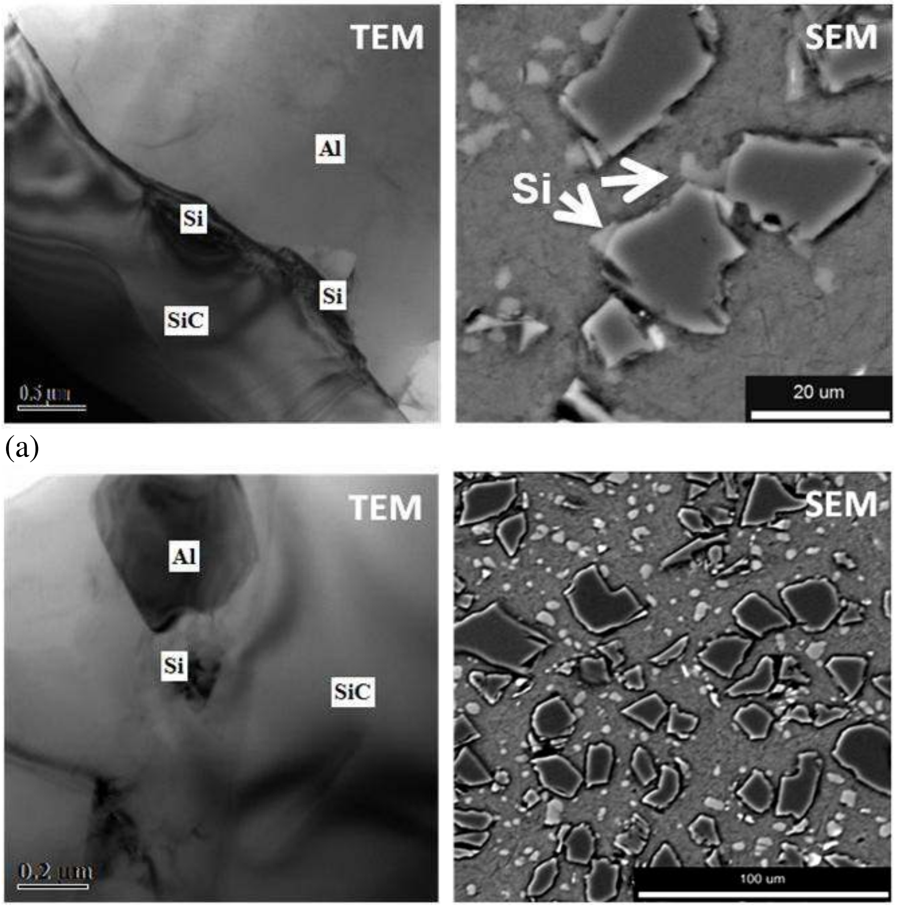

(a)

(b)

Figure 31. Morphology and location of Si phase in (a) as-cast and (b) hot-rolled composites.

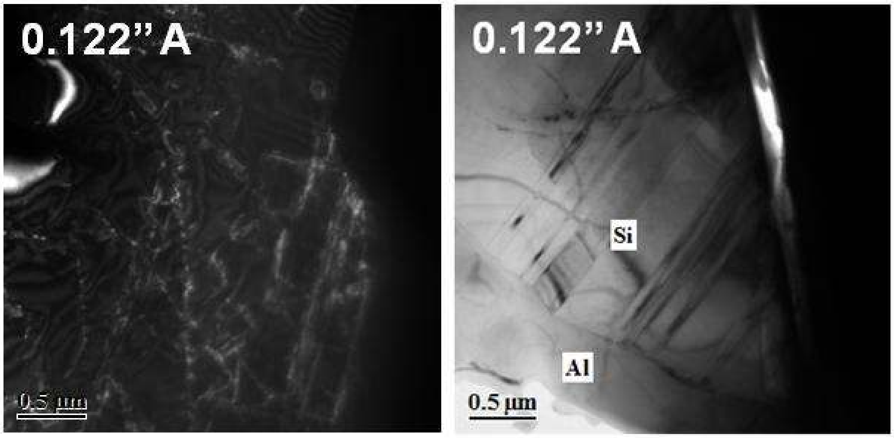

(a) (b)

Figure 32. (a) Weak beam dark field micrograph shows the high dislocation density within the Al matrix particularly around the SiC particle; (b) twins in the Si phase

4.3.1. Effects of Hot-Rolling on the SiC Particle Reinforcement

There is strong evidence that larger SiC particles can break up into smaller particles as a result of hot-rolling as presented in Figure 33. Furthermore, there is sufficient evidence that Al, during successive hot-rolling, can plastically flow into crevices of broken SiC particles as presented in Figure 34. To support these observations, extensive quantitative microscopy was carried out to determine the size and distribution of SiC particles as a function of hot-rolling using a variety of microscopic and image analysis technique. Nine samples from each plate were analyzed (CRP, MRP, ERP, CL, ML, EL, CT, MT and ET).

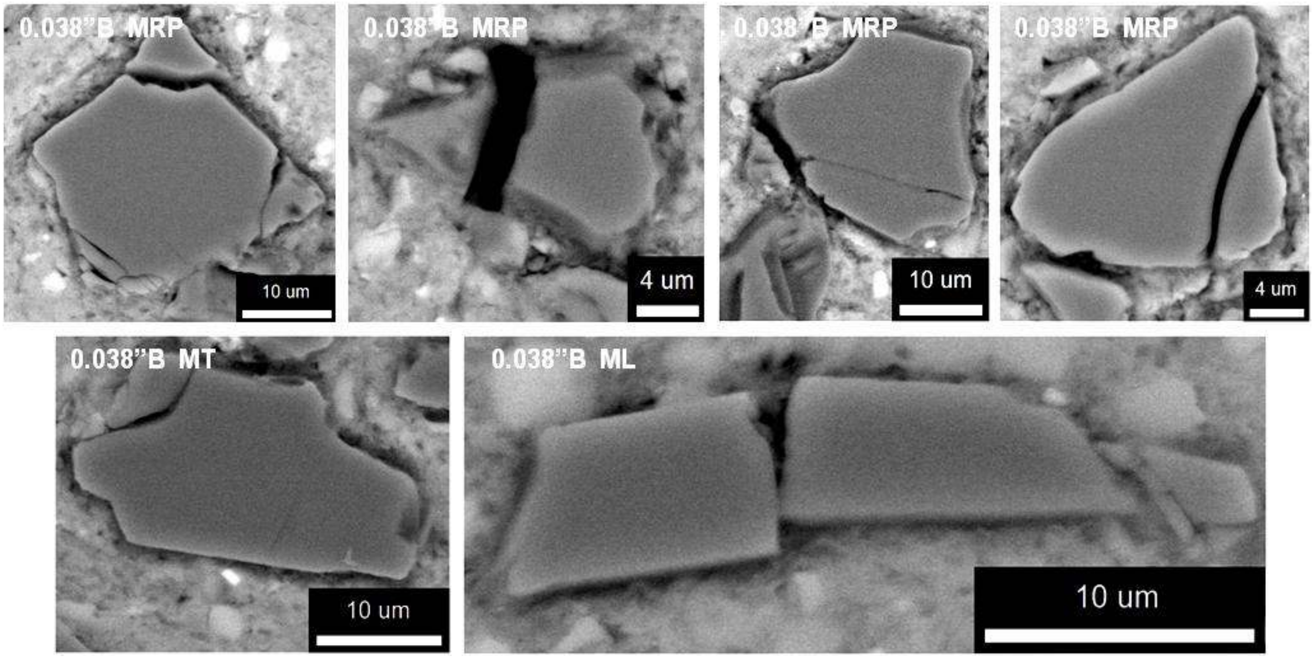

Figure 33. Evidence of SiC particle break-up observed.

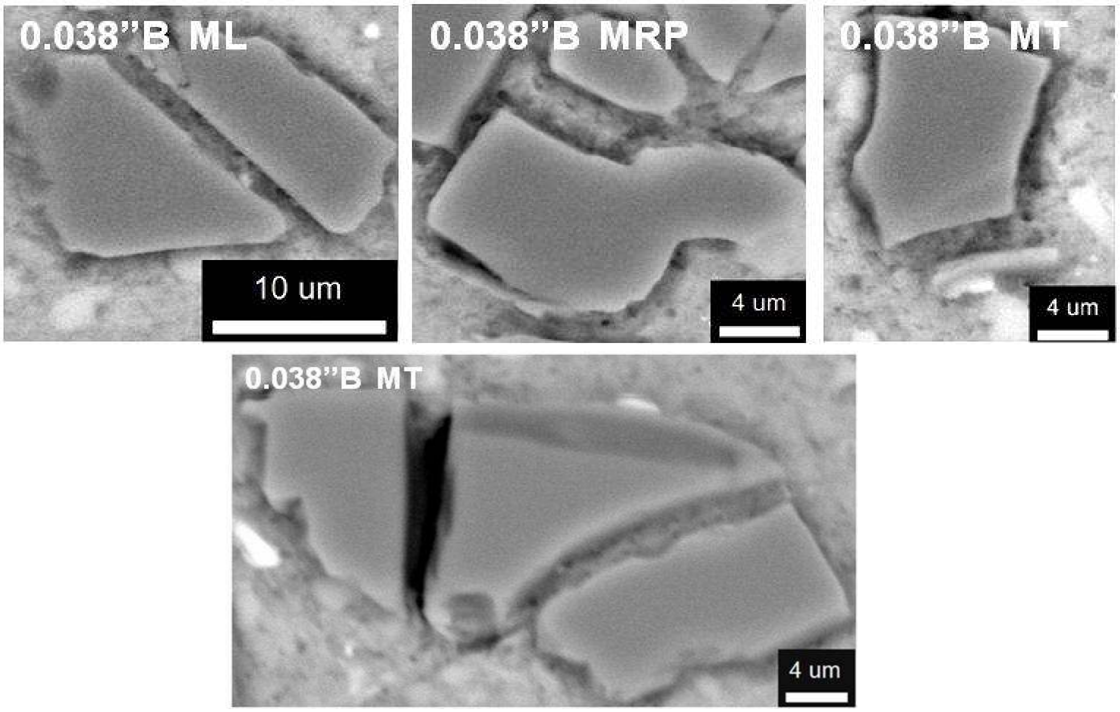

Figure 34.Evidence of Al flow into crevices of broken SiC particles.

Table 3 reports the particle size analysis results (e.g., maximum, minimum, average and standard deviation). The average SiC particle size decreases from 6.75 µm (as-cast) to 5.37 µm (0.038’’B) with hot rolling as presented in Figure 35. The standard deviation of average SiC particle diameter also decreased. Variation in particle size was not observed for different locations of the specimens (e.g., center, middle and edge of the plates). Particle size also did not vary between longitudinal, transverse and rolling planes as presented in Figure 36. Cross-rolling also did not affect the size variation.

Table 3. Evolution of SiC particle size with successive hot-rolling.

Sample ID (Particle Count)	Max. Min. Particle Diameter (µm)	Average SiC Particle Diameter (µm)	Stdev (µm)
As-cast (370)	12.38	6.75	0.27
	3.71		
0.364'' (471)	10.28	6.55	0.26
	4.09		
0.250'' (460)	10.05	6.38	0.24
	3.71		
0.122''A (692)	13.11	6.28	0.20
	3.13		
0.122''B (800)	11.4	6.02	0.21
	2.63		
0.038''A (836)	12.33	5.47	0.16
	2.47		
0.038''B (921)	10.21	5.37	0.16
	2.49		

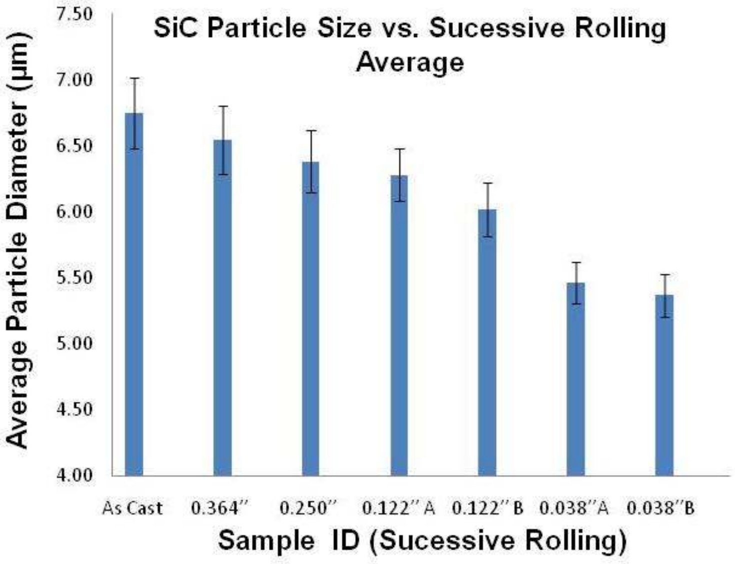

Figure 35. Changes in average SiC particle size with successive hot-rolling.

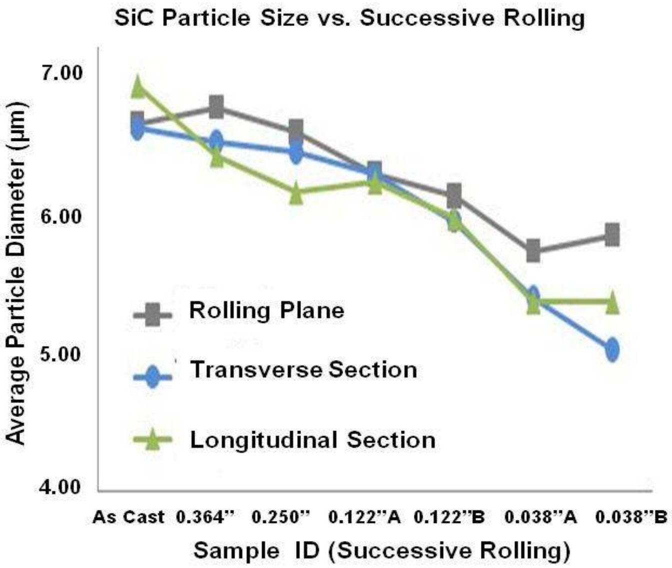

Figure 36. Changes in average SiC particle size in rolling plane, transverse and longitudinal direction with successive hot-rolling.

A small reduction in the mean inter-particle distance was observed with successive hot-rolling, from 11.84 µm for the as-cast sample to 9.2 µm for the 0.038''A sample, as presented in Figure 37. The mean inter-particle distance tends to fluctuate significantly due to the continuous particle break-up and subsequent re-arrangement. However, the smallest inter-particle distance was observed for the 0.122''A sample, and this is consistent with the observation of SiC particle break-up with successive hot-rolling. The application of the first two hot rolling passes (64% and 75% reduction) improves the uniformity in the distribution of SiC_p from the as-cast distribution as presented in Figure 38. An improvement in the uniformity of particle distribution is observed for the longitudinal section. However, in general hot-rolling does not improve the uniformity in distribution due to SiC particle break-up.

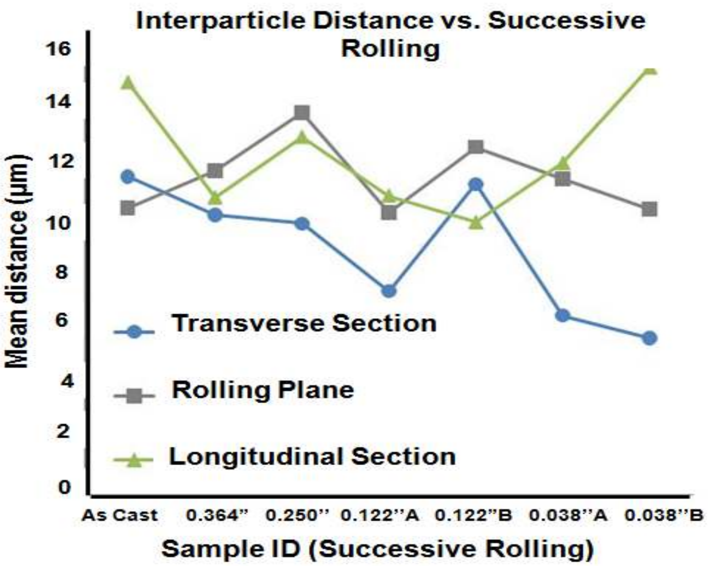

Figure 37. Evolution of mean inter-particle distance with successive hot-rolling.

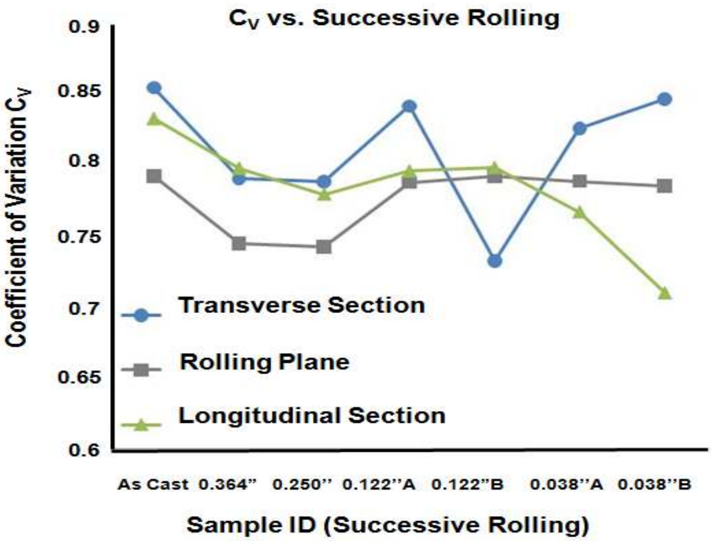

Figure 38. Evolution in coefficient of variation for inter-particle distance with successive hot-rolling.

In general, distribution of SiC particles was very uniform. However, there were regions where clustering of SiC particles were observed as presented in Figure 39 (a). Voids, most likely due to incomplete infiltration and oxide inclusions during mixing or casting, were also frequently observed in as-cast composite where a clustering of SiC particles occurred as presented in Figure 39 (b). The areal fraction of these voids has been quantified as a function of successive rolling using optical photomicrographs, and they are reported in Table 4. The maximum size of voids observed was approximately 180μm in the as-cast specimen. The average size of voids decreased with successive rolling. However, the number of voids tended to fluctuate due to break-up of SiC particles especially after the third pass (0.122''A). A significant amount of new voids appeared as a result of the particle fracture into two or more parts. This result is also consistent with measurement of inter-particle distance and coefficient of variation. Most, if not all, voids were located between the broken SiC particles after the last rolling steps.

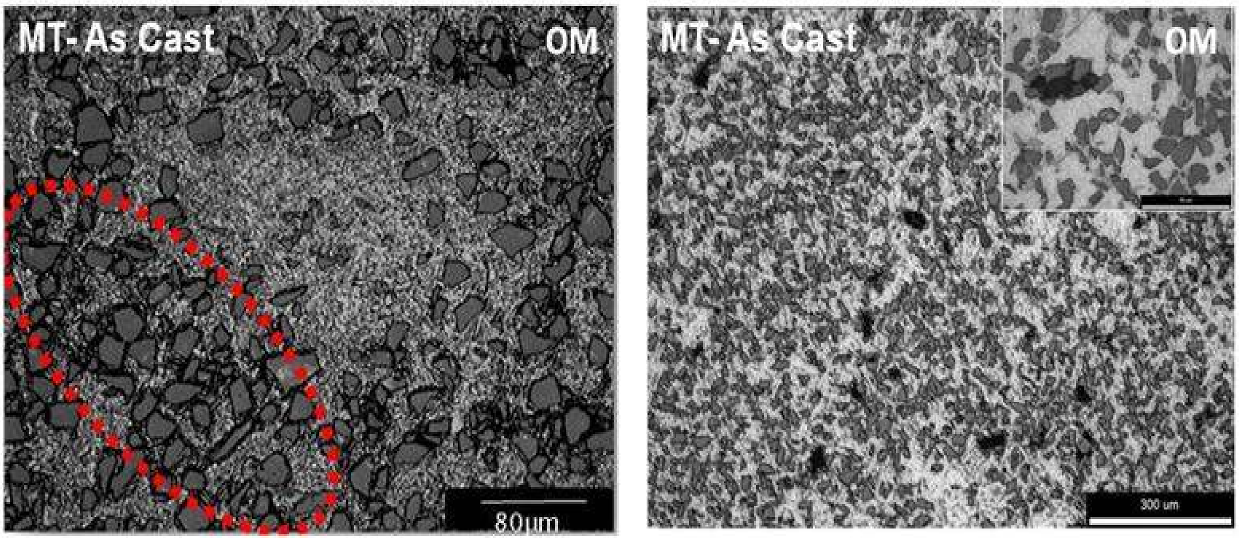

(a) (b)

Figure 39. (a) Clustering of SiC particles and (b) voids, most likely due to incomplete infiltration and oxide inclusions during mixing or casting, were observed, however seldom.

Table 4. Quantification of voids in composites.

ID Sample	**Area Fraction (%)**			**Stdev**
As-cast	Long. Trans, or RP		1.21	0.51
0.364"	Longitudinal	0.34	0.71	0.48
	Transverse	0.9		
	Rolling Plane	0.95		
0.250"	Longitudinal	0.08	0.17	0.17
	Transverse	0.12		
	Rolling Plane	0.24		
0.122"A	Longitudinal	0.11	0.36	0.23
	Transverse	0.49		

	Rolling Plane	0.48		
0.122"B	Longitudinal	0.07	0.09	0.09
	Transverse	0.12		
	Rolling Plane	0.08		
0.038" A	Longitudinal	0.00	0.08	0.12
	Transverse	0.15		
	Rolling Plane	0.18		
0.038" B	Longitudinal and/or Transverse	0.07	0.07	0.07

Given the observations of microstructural evolution with successive hot-rolling, preliminary assessment of mechanical property, e.g., hardness, was carried out. The volume fraction, shape, size and distribution of the precipitates and the reinforcement particles influence the micro deformation. Ten independent measurements were taken for each sample using Vickers. Hardness decreased for the hot rolled (74.12 ± 3 H_V) samples compared to the as-cast samples (98.4 ± 1.8 H_V) as presented in Figure 40. No significant difference was observed in the hardness among the hot rolled plates.

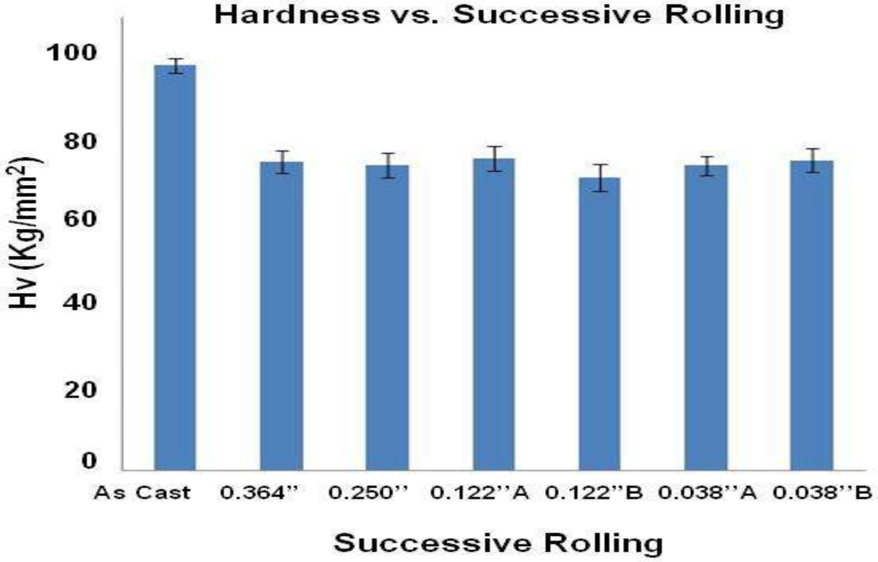

Figure 40. Hardness as a function of successive hot-rolling.

4.4. High Strain Rate Deformation of MMCs

4.4.1. Sample “A”

Figure 41 presents photographs of the sample “A.” Fragmentation failure, schematically illustrated in Figure 42, typical of thick brittle plates with high strength, was observed in the plate “A.” Limited fracture surface analysis was carried out in order to minimize debris falling from the exposed surface. Near the entrance, the fracture surface consisted of a Al-Si matrix and Pb-rich residuals without apparent presence of SiC as presented in Figure 43. Some regions were rich with Cu residuals. Through the penetration channel, Fe- and Pb-rich residuals were observed, while the fractured surface that surround the penetration channel actually exhibited some SiC particles as shown in Figure 44.

Figure 41. Photograph of the failed sample “A” after high stain impact.

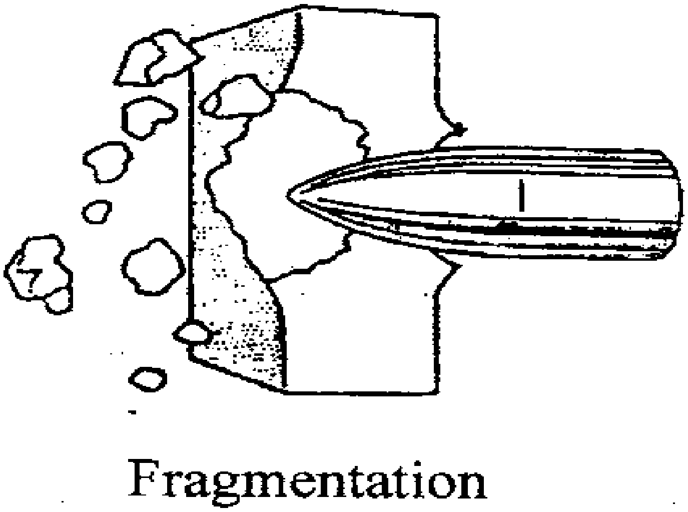

Figure 42. A schematic illustration of fragmentation failure of materials tested.

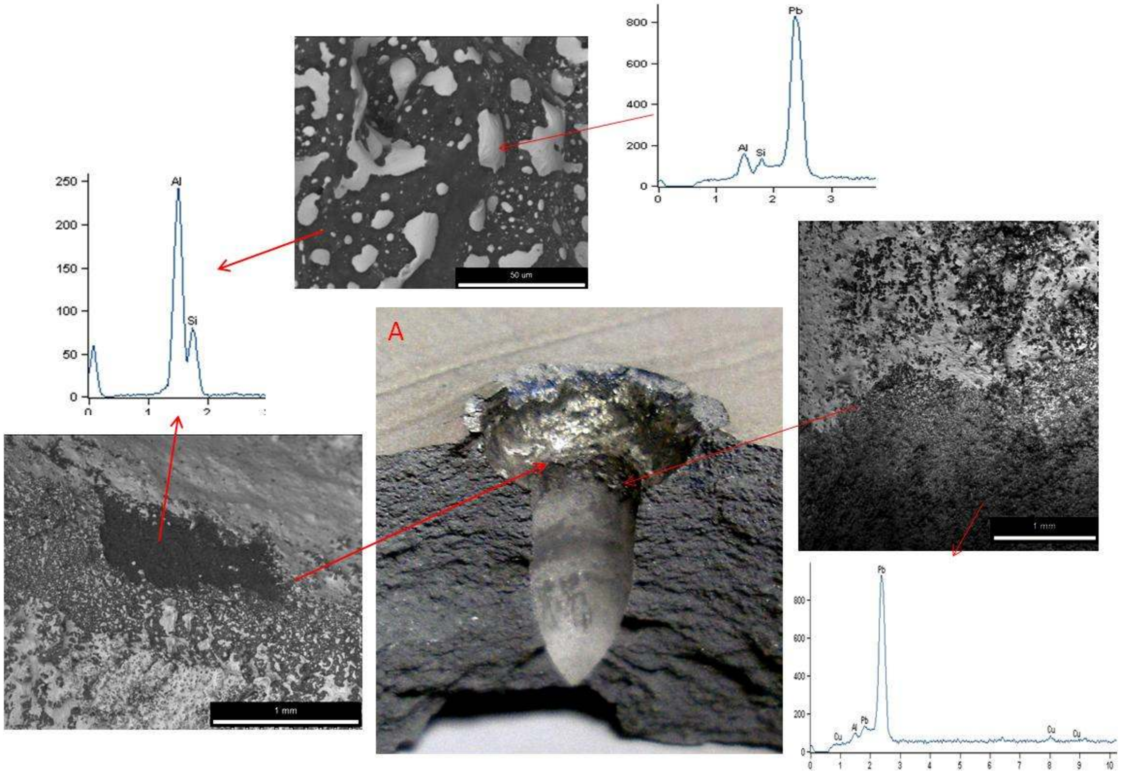

Figure 43. Highlights of SEM analyses near the entrance region on the sample “A.”

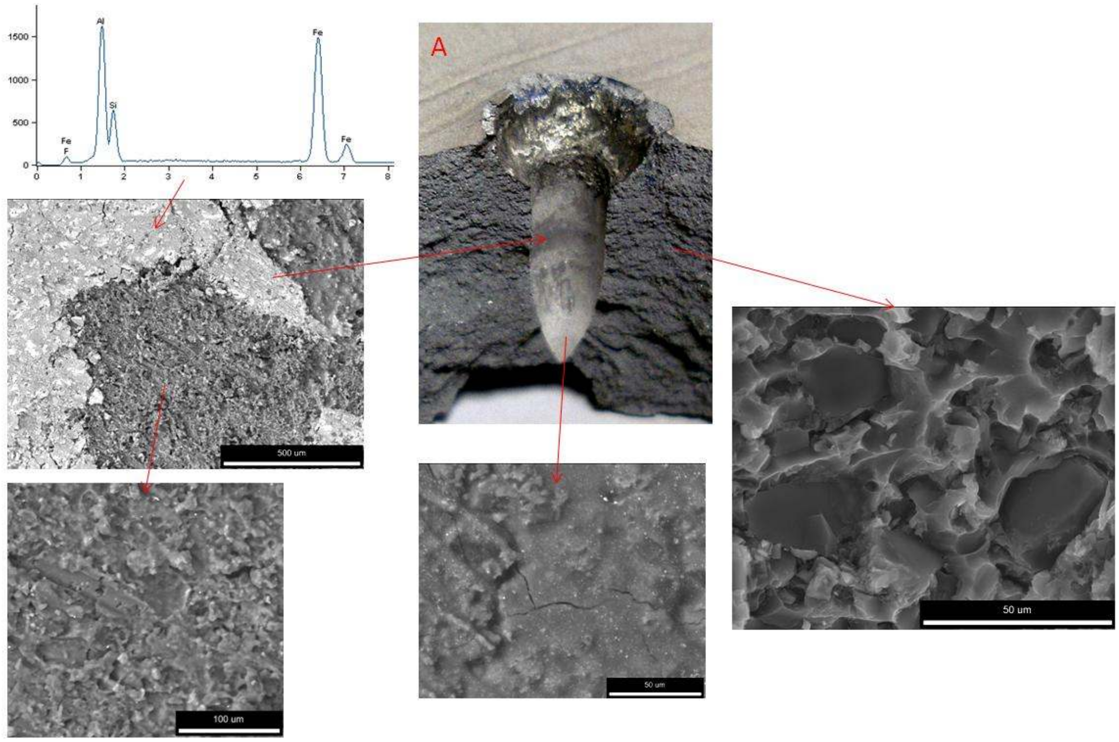

Figure 44. Highlights of SEM analyses of the penetration channel on the sample “A.”

Observations made on the exposed penetration surface were consistent when cross-sectional microstructural analyses were carried out on polished samples. Figure 45 presents backscatter electron micrographs and XEDS data from near the entrance of sample “A.” At the very beginning of the entrance, a mixture of Pb-rich residuals and Al-SiC_p composites were observed, while most of the entrance (e.g., length-wise) surface was coated with Cu-, Pb- and Fe-rich residuals intermixed with constituents of the composite. This observation strongly suggests that melting of composite has occurred.

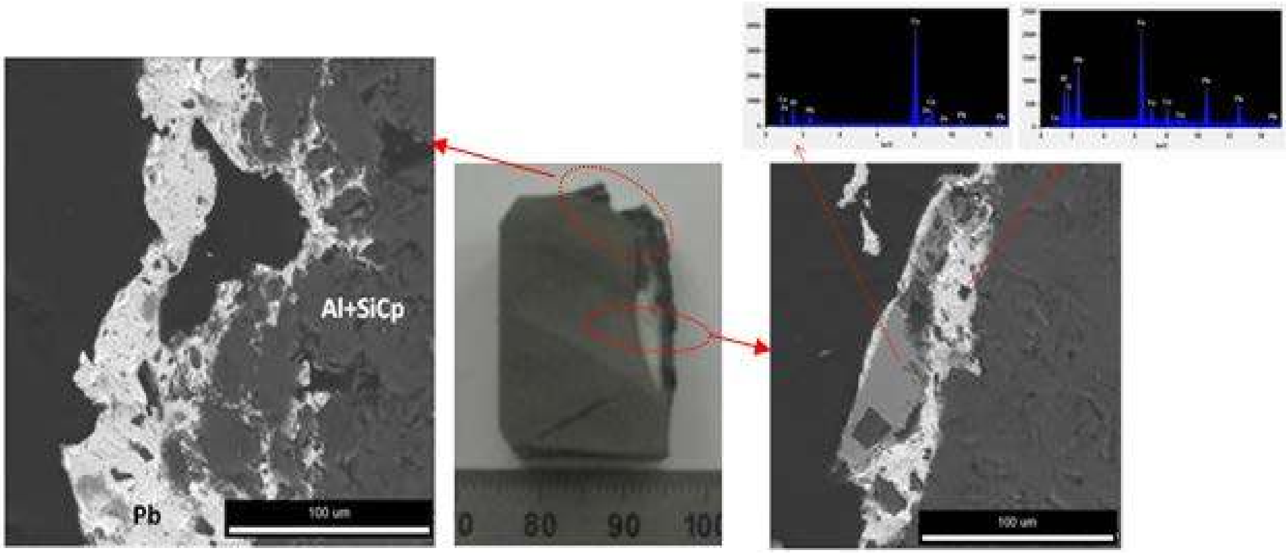

Figure 45. Cross-sectional backscatter electron micrographs and corresponding XEDS data from near the entrance of sample “A.”

A mixture of residuals and composite constituents were observed throughout the penetration channel as shown in Figure 46. Approximately 20 to 50 μm deep, the intermixed zone consisted of Al matrix, Pb-rich residuals and SiC reinforcement particles – all three constituents well dispersed as shown in Figure 46. Large pores, some as large as 60 μm in diameter were observed at the interface between the intermixed region and the composite. In regions without pores, an abrupt interface between the composite and intermixed region was observed.

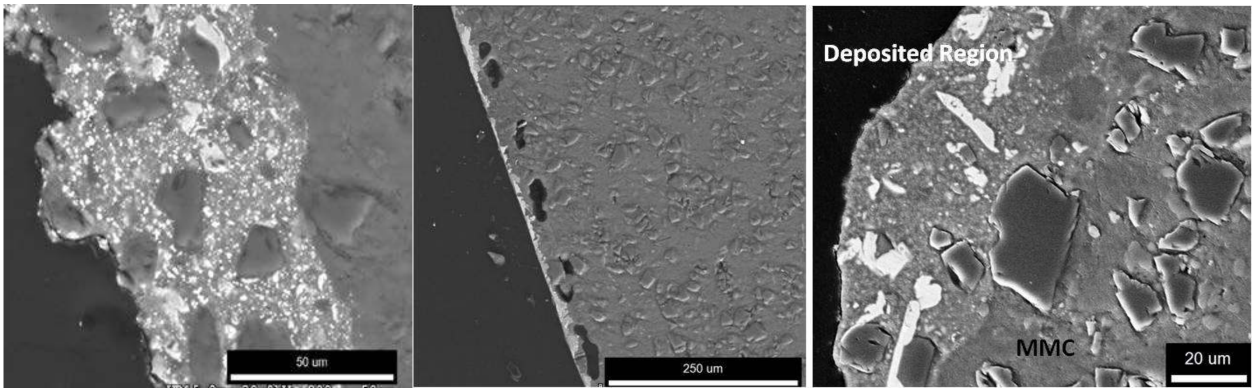

Figure 46. Cross-sectional backscatter electron micrographs from the penetration channel of sample “A.”

4.4.2. Sample “B”

Figure 47 presents photographs of the sample “B.” Radial failure, schematically illustrated in Figure 48, typical of brittle material was observed in the plate “B.” Again, limited fracture surface analysis was carried out in order to minimize debris falling from the exposed surface. Near the entrance, the fracture surface consisted of Al-Si matrix, and Pb- and Fe-rich residuals without an apparent presence of SiC as presented in Figure 49. Through the penetration channel, Fe- and Pb-rich residuals were observed as shown in Figure 50. Many cracks near the trough of penetration cavity were observed.

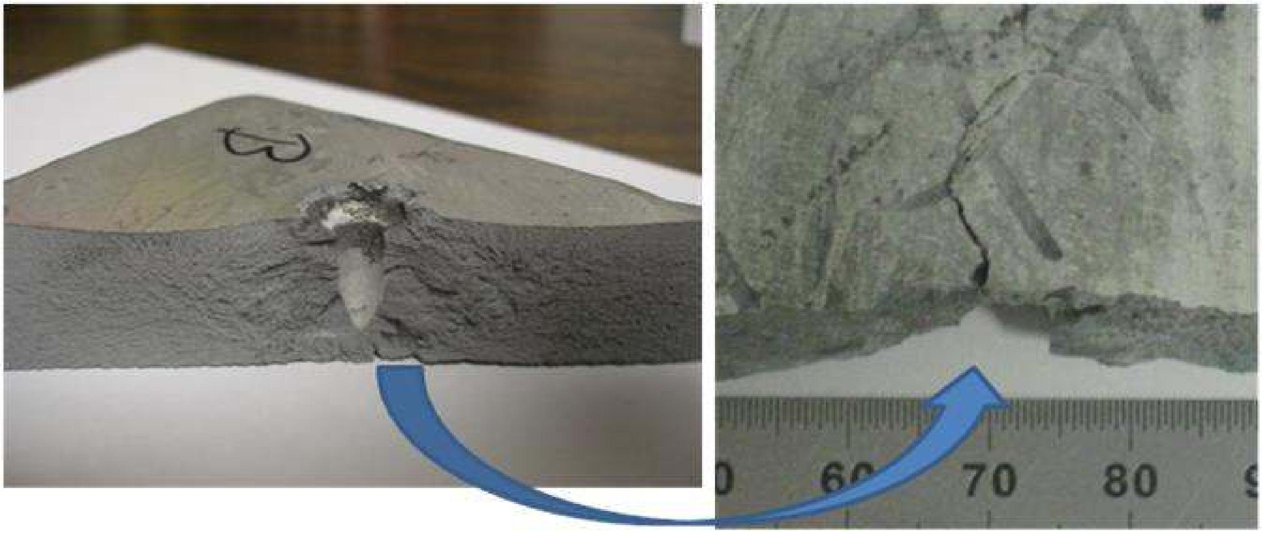

Figure 47. Photograph of the failed sample “B” after high strain rate impact.

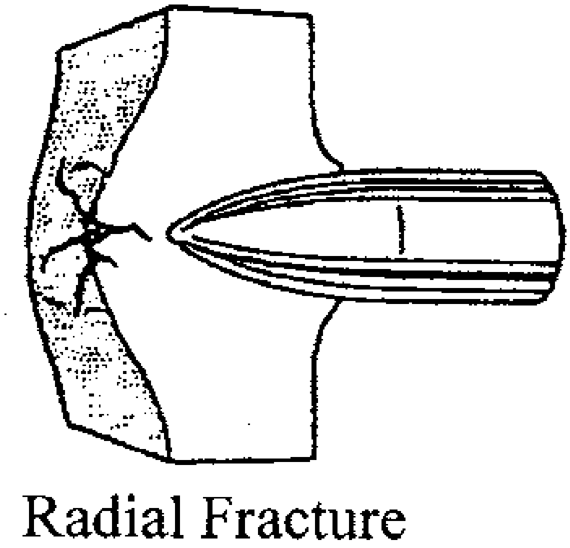

Figure 48. A schematic illustration of radial failure of materials tested.

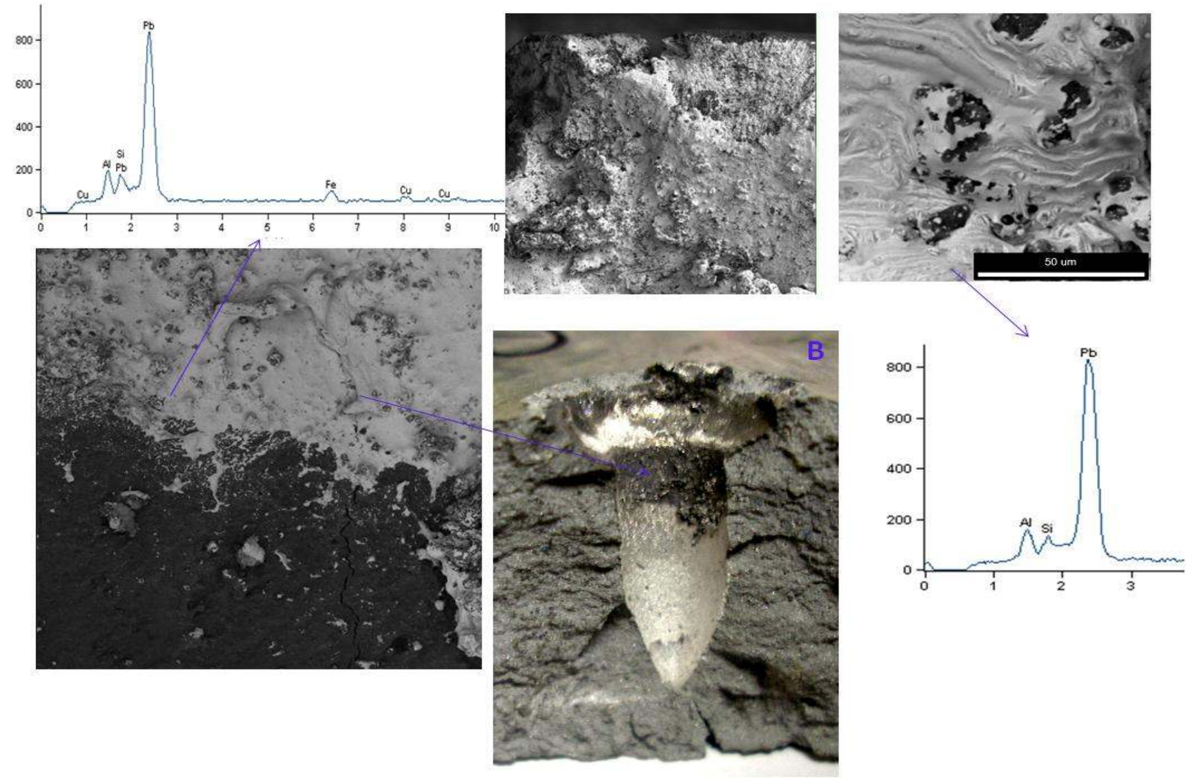

Figure 49. Highlights of SEM analyses near the entrance region on the sample “B.”

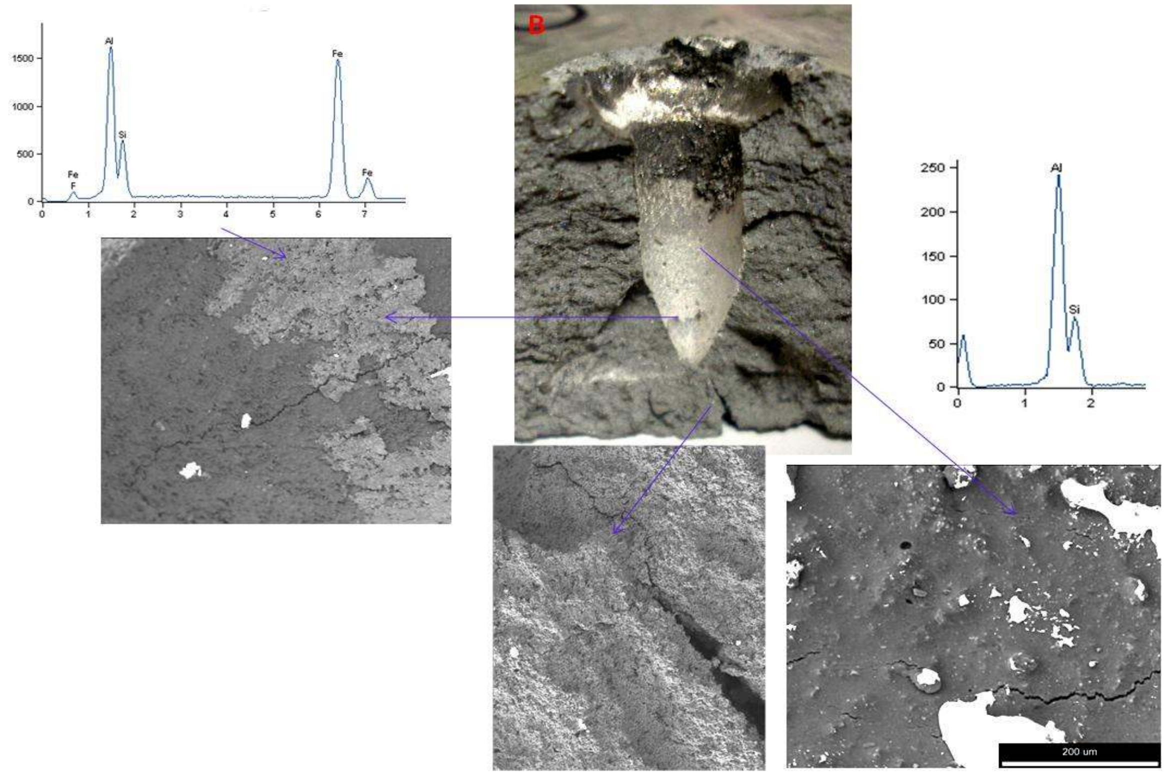

Figure 50. Highlights of SEM analyses of the penetration channel on the sample "B."

Figure 51 presents backscatter electron micrographs and XEDS data near the entrance of sample "B." At the entrance, a mixture of Pb-rich residuals and Al-SiC$_p$ composites were observed. Unlike the sample "A," the mixed region appeared to have formed by cracking in the composite followed by infiltration of molten residuals. Furthermore, unlike the sample "A," cracks along the Al-SiC interface, within SiC and within Al matrix are observed. Along the penetration channel, as shown in Figure 52, a significant amount of break-up and/or de-bonding of SiC particles was observed along with crack propagation through interdendritic regions rich in Si.

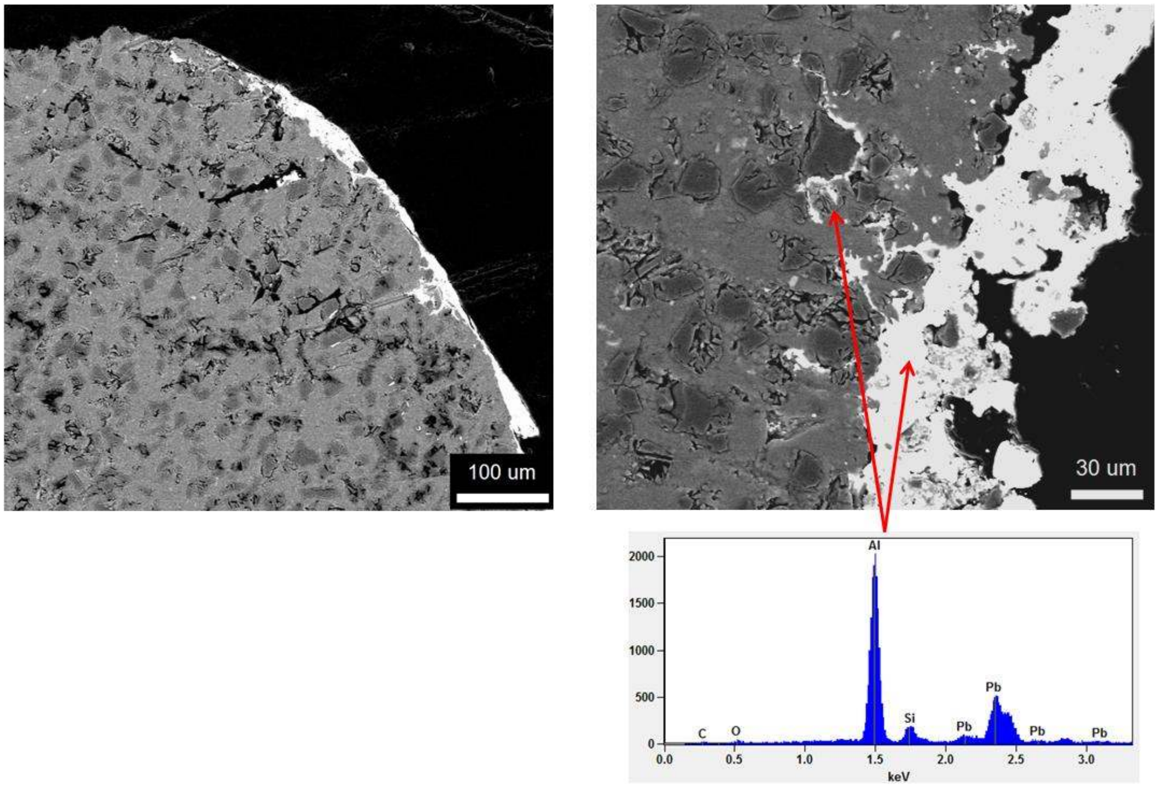

Figure 51. Cross-sectional backscatter electron micrographs and corresponding XEDS data from near the entrance of sample "B."

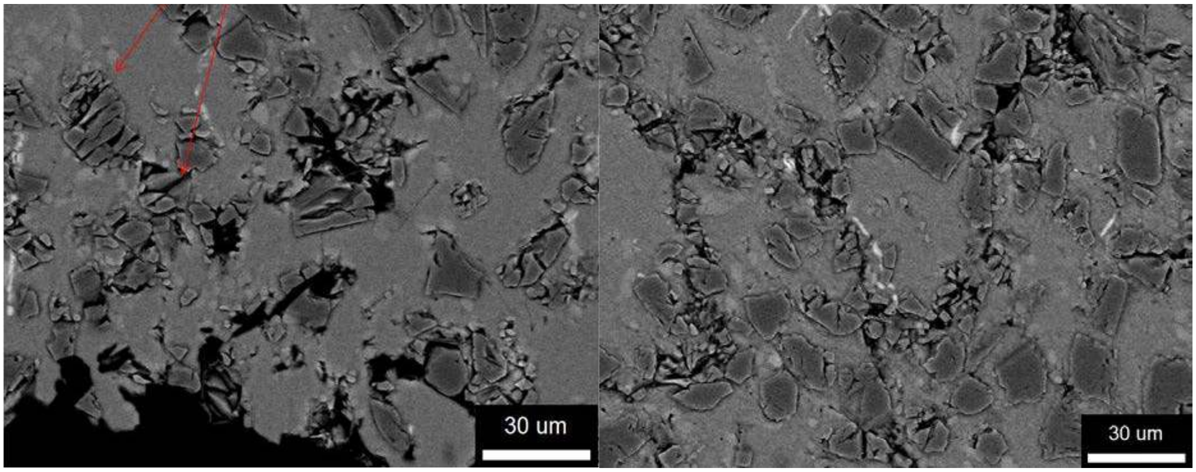

Figure 52. Cross-sectional backscatter electron micrographs from the penetration channel of sample "B."

4.4.3. Sample "C"

Fragmentation failure was observed for sample "C" as presented in Figure 53, similar to sample "A," and schematically illustrated in Figure 42. Fragmentation failure appears in thick plates with enough strength, but are brittle. As with two previous samples, a real fracture surface cannot be obtained due to the residuals of the projectile. However, it is clearly observed that Cu- and Pb-rich residuals melted and deposited on the composite surface and the penetrated surface of the composite appears to be also melted as presented in Figure 54. And the intermixing due to melting of both constituents occurred more significantly along the penetration channel.

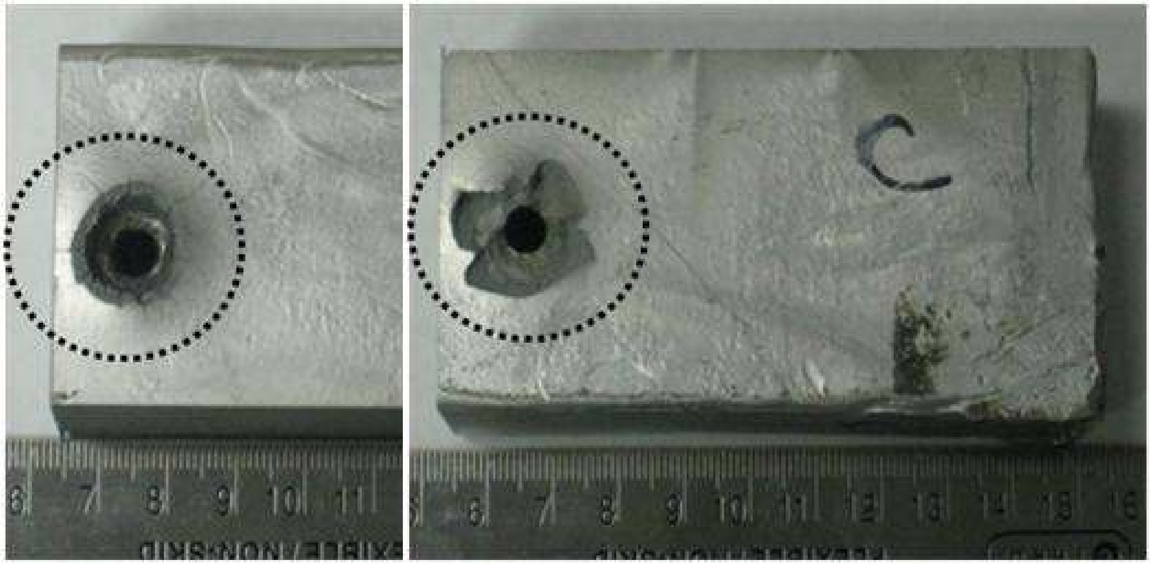

Figure 53. Photograph of the failed sample “C” after high strain rate impact: (left) entrance and (right) exit.

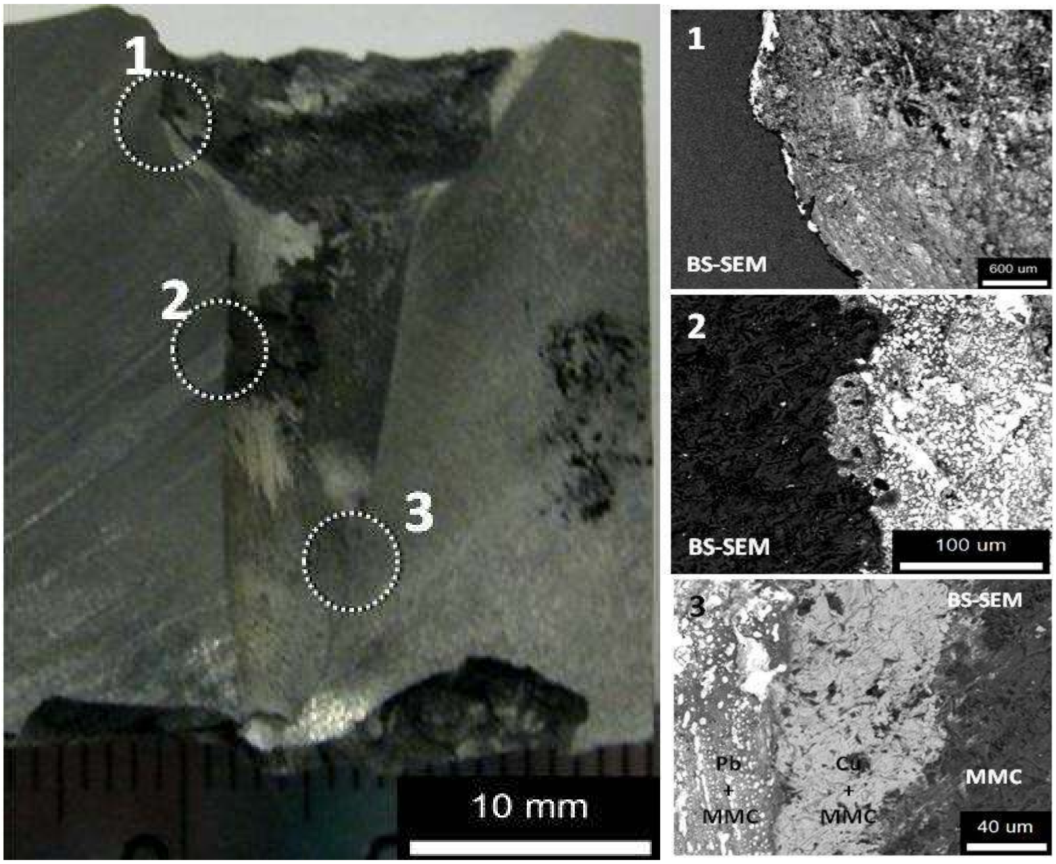

Figure 54. Optical and backscatter electron micrographs of entrance and penetration channel of composite sample “C.”

On the exit region, a significant intermixing of constituents was observed. Some features suggested that the composite constituents were melted and “dragged” or “splashed” by the projectile near to the exit as presented in Figure 55.

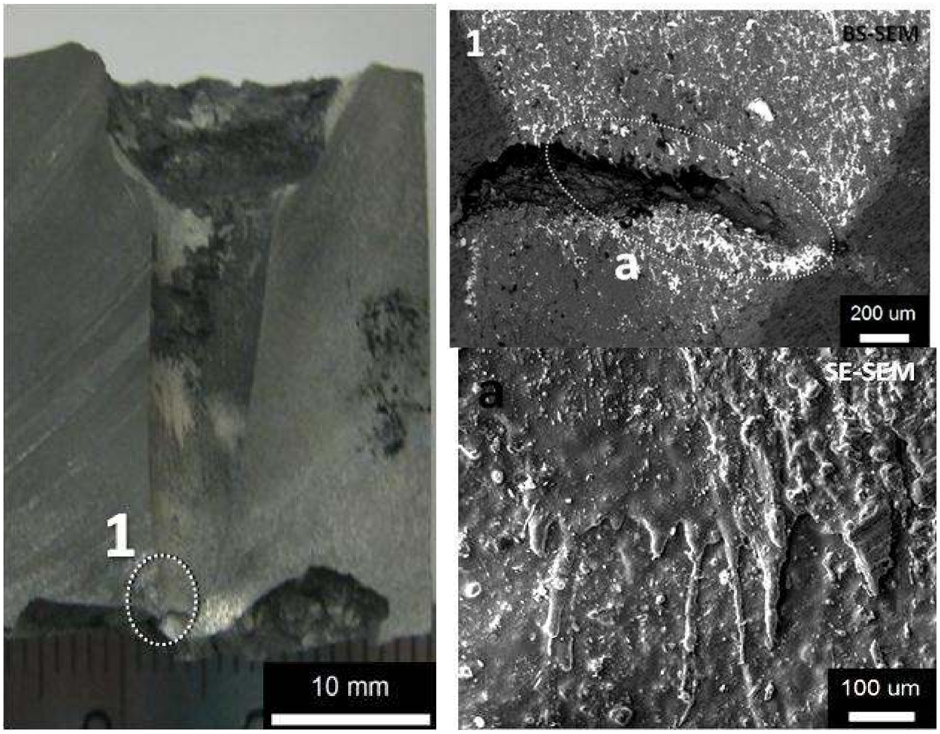

Figure 55. Optical and backscatter electron micrographs of exit region in composite sample "C."

Detailed microstructural analyses on cross-sections, after metallographic preparation was further carried out for the composite sample "C." The composite consisted of Al matrix (lighter gray), SiC particles (darker gray) and spheroidized Silicon phase (white) as presented in Figure 56.

On the entrance, several sub-cracks propagating through the eutectic Si and Al-SiC particles were observed as shown in Figure 57. Near the exit, a significant cracking was observed approximately at 45° angle (i.e., maximum shear stress) as shown in Figure 58. No sub-cracking was observed throughout the penetration channel. Pb-rich residuals were quite predominant at the entry region. A clear indication of melting and intermixing of all constituents were observed significantly through the penetration channel, although the intermixing is not so significant at the entry region. At the exit region, the composite appears to have cracked due to maximum shear stress (suggested by the 45° angle cracks). Some of these sub-cracks were filled with projectiles such as Fe- and Pb-rich residuals as presented in Figure 58. Some intermixing with residuals, Al matrix and SiC particles were observed in these residual-filled sub-cracked regions.

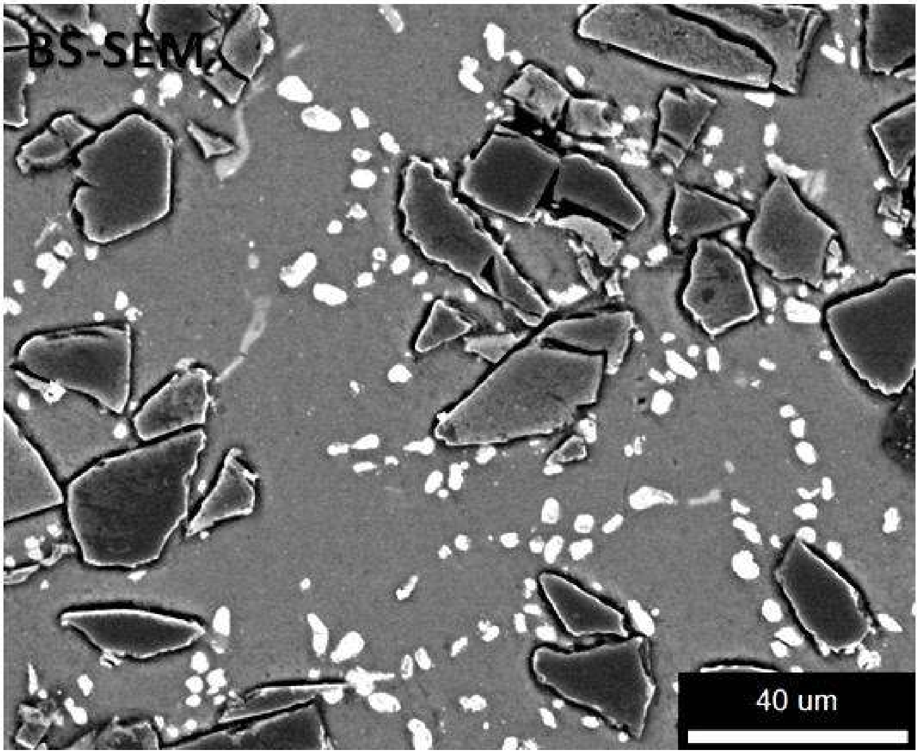

Figure 56. Backscatter electron micrograph from composite sample "C."

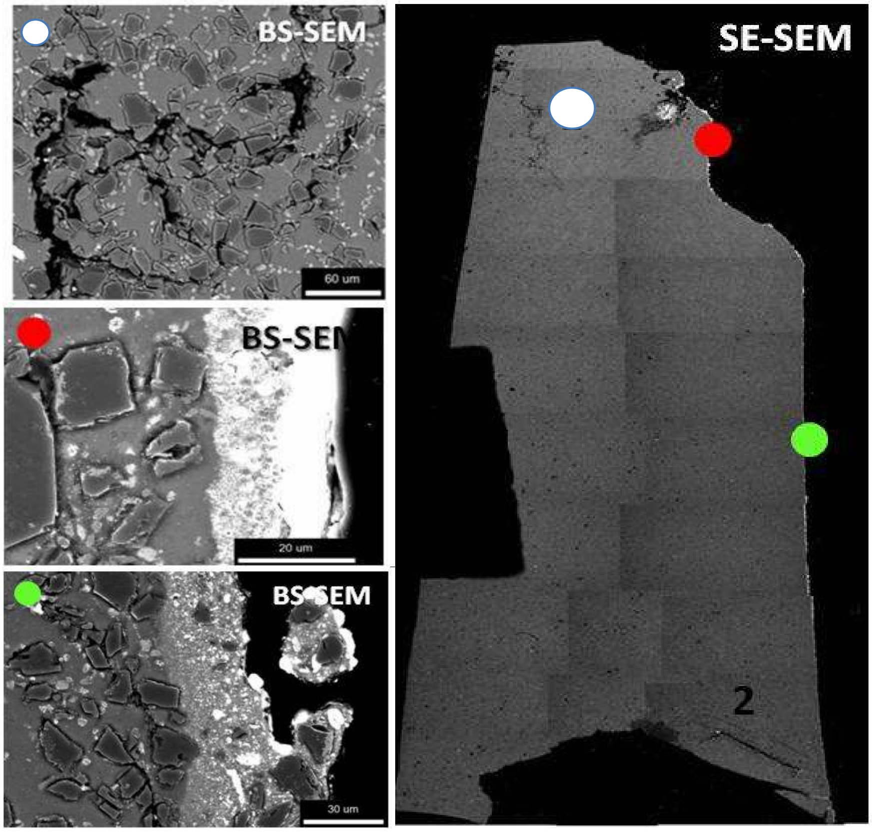

Figure 57. Cross-sectional microstructural features from entrance and penetration channel composite sample “C.”

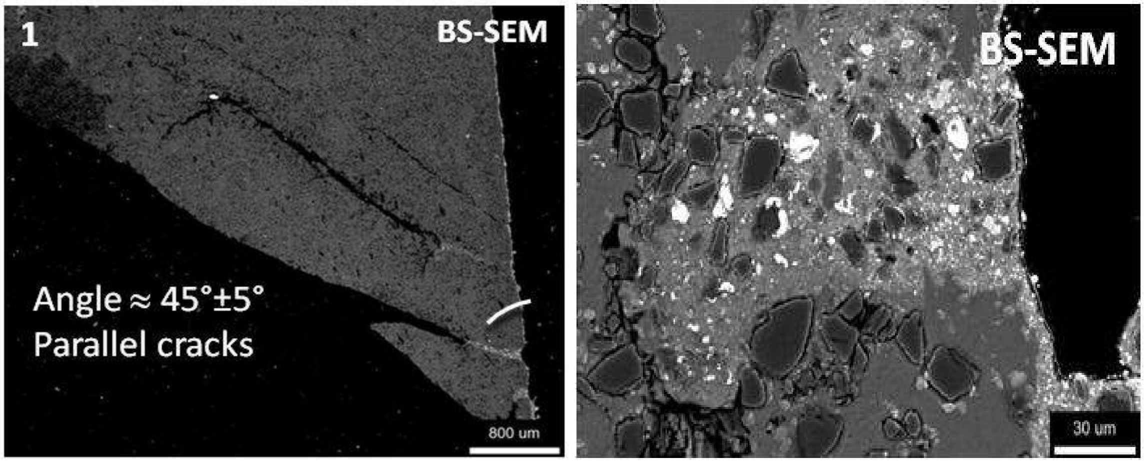

Figure 58. Intermixing of projectile residuals and constituents of the composites in the sub-cracks near the exit region.

4.4.4. Sample “D”

Figure 59 presents photographs of the sample “D.” Petalling failure, schematically illustrated in Figure 60, at the entrance area and fragmentation failure, schematically illustrated in Figure 24, at the exit was observed in the plate D. This suggests a combination of brittle and ductile characteristics. Fragmentation failure appears in thick and strong plate brittleness while petalling failure, observed at the entrance, suggests the presence of ductility in this composite. A significant amount of Copper jacket was found embedded in the composite. Again similar to previous samples, the exposed surface from the entrance, through the penetration channel and at the exit was covered with residuals of projectiles including Copper jacket as shown in Figure 61. Signature of molten and solidified Pb-rich residuals covering the composite is evident, and the molten residual might have “dragged” composite constituents down to the exit region as indicated by red arrow in Figure 61 (region 4).

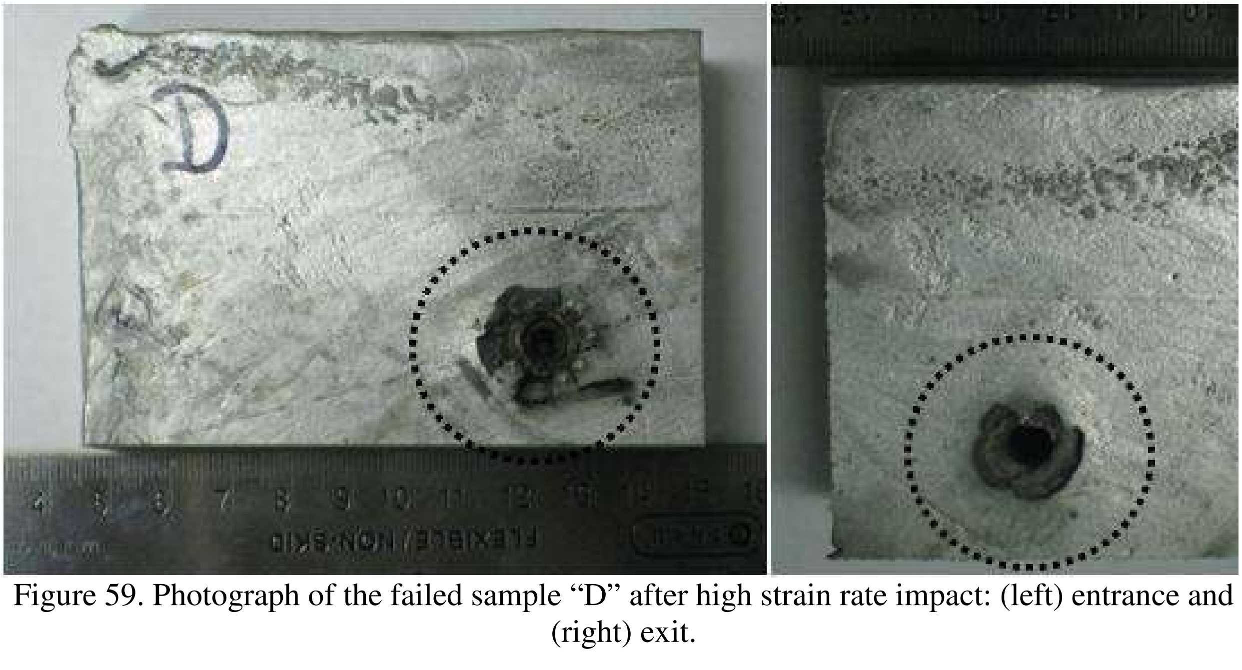

Figure 59. Photograph of the failed sample “D” after high strain rate impact: (left) entrance and (right) exit.

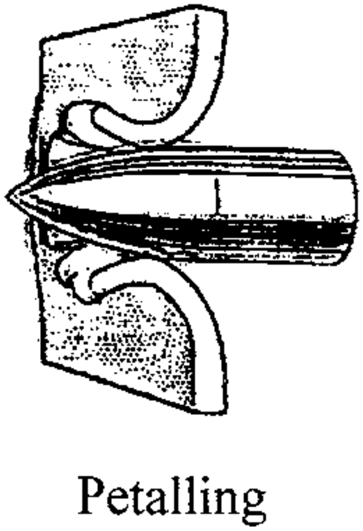

Figure 60. A schematic illustration of petalling failure of materials tested.

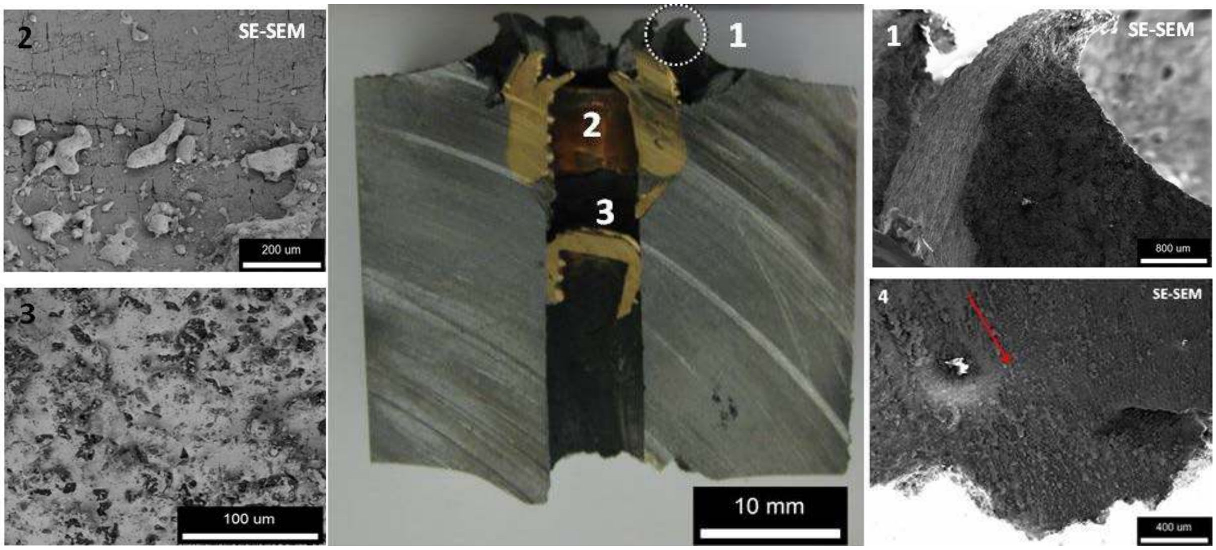

Figure 61. Optical and backscatter electron micrographs of composite sample "D."

The penetration channel of the composite "D" was prepared metallographically as shown in Figure 62. During microstructural study, we have noticed a difference in the phase constituents of the composite, and XRD pattern for this composite was obtained as shown in Figure 63. The constituents in the composite D were identified as Aluminum matrix (light gray), and Al_2O_3 particulate reinforcement (dark gray) as presented by optical micrograph in Figure 64.

This difference in phase constituents of the composite may explain why the failure characteristics appear to be different from other composites.

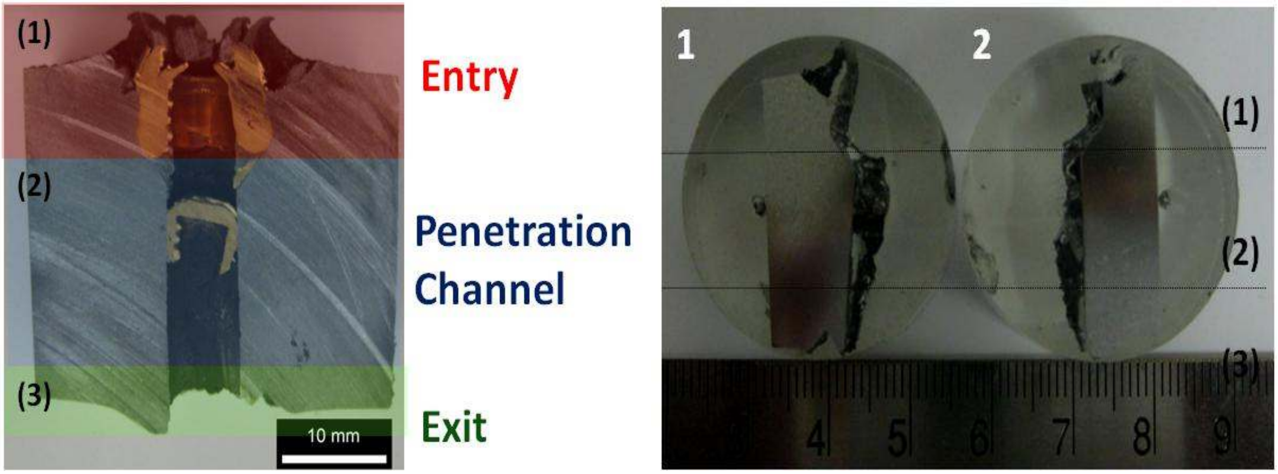

Figure 62. Metallographic preparation of composite “D.”

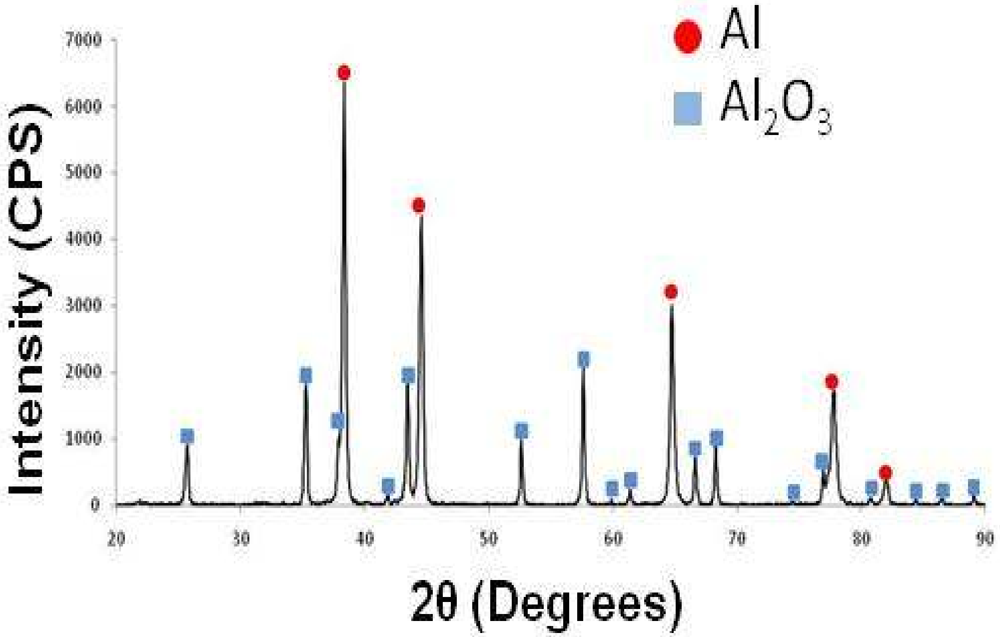

Figure 63. XRD of composite “D.”

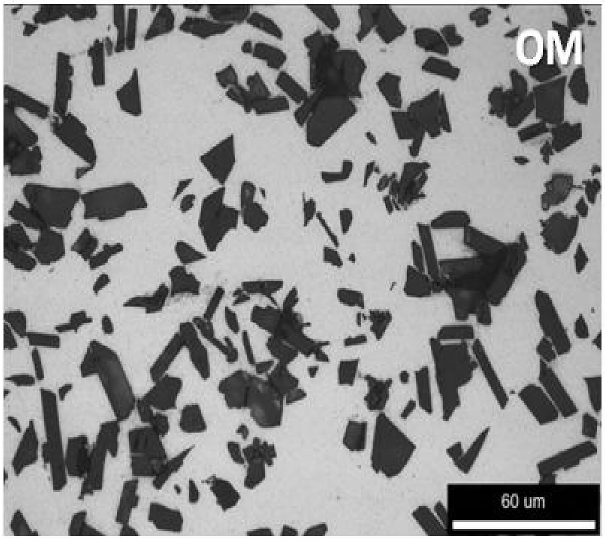

Figure 64. Optical micrograph of composite "D."

Detailed microstructural analysis, however revealed similar trends observed for other composites. There was clearly Pb-rich residuals with a significant intermixing of projectile and composite constituents due to melting. Many sub-cracks were observed, mostly at the entry and exit regions as indicated by white arrows in Figure 65. In particular near the exit region, parallel cracks angled at 30° as shown in Figure 66. These parallel cracks at the exit regions were filled with Cu-, Pb- and Fe-rich residuals, and this is most likely a result of molten residual filling-in of the cracks. In other words, melting of the projectile residuals and composite constituents leads to intermixing occurred after cracks have propagated.

The high speed of the projectile during impact causes melting of the aluminium matrix as well as the projectile material. This is a result of the excess of heat generated by friction at high velocity. The most exceptional feature of this deformation behavior at high strain rate is the apparent instantaneous melting of aluminium matrix and projectile material followed by the distribution of this molten material through the cracking generated in the initial stages of the impact, producing a new solidified microstructure.

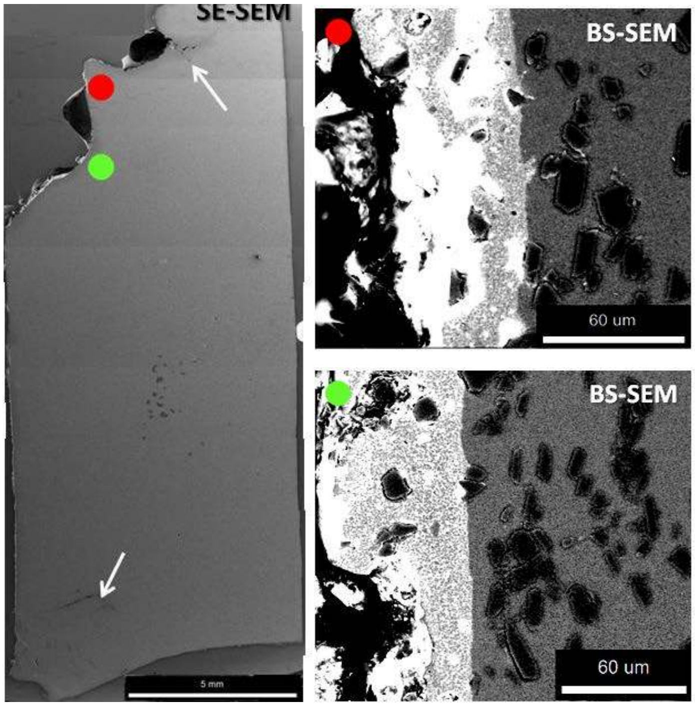

Figure 65. Cross-sectional microstructural features from composite sample “D.”

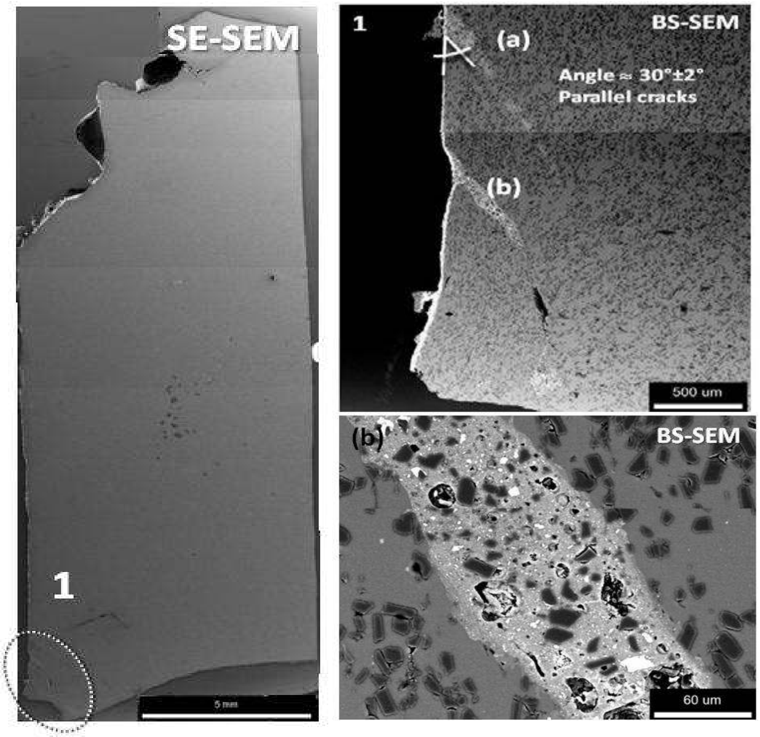

Figure 66. Cross-sectional microstructural features from entrance and penetration channel composite sample “D.” Intermixing of projectile residuals and constituents of the composites in the sub-cracks near the exit region is evident.

.

CHAPTER 5: CONCLUSIONS

This investigation was conducted with the main purpose of understanding how hot rolling and annealing affect the microstructure of Al-A359 / 30 vol.% SiC_P metal matrix composite and how these processes can be used to tailor its performance under high strain rate impact. Findings from this investigation are listed below:

- ✓ Lamellae microstructure (Si-rich phase in Al-Si eutectic) in the as-cast evolved into spherical morphology with isothermal anneal and successive hot-rolling. Si is uniformly distributed within the fcc-Al matrix particularly after successive rolling.
- ✓ Various precipitates and/or dispersoids were observed in the Al/SiC_p, Al/Si interface and within the Al matrix:
    - Mg_2Si, Al_2Cu, and $MnSi_2$.
    - Others containing Al-Fe-Si and Fe-Mg-Al-Si.
    - $MgAl_2O_4$ at the Al-Si interface.
- ✓ Average particle size of SiC_P decreased with the successive hot rolling due to the break-up of SiC_P.
- ✓ Homogenous distribution of SiC particles within the Al matrix is observed after successive rolling.
- ✓ Voids created during casting were closed and welded after successive hot rolling.
- ✓ The last reduction (96% reduction for the 0.038''A and B plates) exhibited the best particle size uniformity and lowest areal fraction of voids.
- ✓ The eutectic Si morphology characteristics of the Al-SiCp composites varied with annealing times and temperatures. The higher degree of spheroidization was obtained by holding the as-cast microstructure at 538°C for 15-30 min during isothermal anneal.

- ✓ Cracks, fractures, petalling and melting were observed after high velocity impact. The fracture mechanism appears to be a combination of interfacial de-bonding, fracture of SiC and Si particles, and *subsequent* melting of the components. The understanding of the behavior of MMCs under high velocity impact is complex due to the large number of parameters involved such as velocity of projectile and target, shape of target, projectile shape and materials, and target material characteristics.

LIST OF REFERENCES

ASM Handbook. (1992). Alloy Phase Diagrams. *ASM International* **3**,321.

Ballufi, R. W., Allen, S. M., and Carter, W. C. (2005). Morphological evolution due to capillary and applied mechanical forces. *Kinetics of materials*, 335-346.

De Sanctis., Evangelista, E., Forcellese, A. and Wang, Y.Z. (1996) Hot Formability Studies on 359/SiC/20p and Their Application in Forging Optimization. *Applied Composite Materials* **3**. 179-198.

Fujikawa, S., Hirano, K and Yoshiaki, F. (1978). Diffusion of Silicon in Aluminum. *Metallurgical Transactions A* **9A**, 1811.

Glicksman, M.E. (2000). Diffusion in Solids: Field Theory, Solid-State Principles and Applications. ISBN 0-471-23972-0, John Wiley & Sons Inc., New York, USA.

Hashim, J., Looney, L., and Hashmi, M.S.J. (2002). Particle Distribution in Cast Metal Matrix Composites-Part I. *Journal of Materials Processing Technology* **123.** 251-257.

Herling, D.R., Grant, G. J. and Hunt, W. (2001). Low-Cost Aluminum: Metal Matrix Composites. *Advanced Materials & Processes*, 37-40.

Kainer, KU. (2006). Basics of Metal Matrix Composites. 1-52.

Karamis, M.B., Nair, F., and Tasdemirci, A. (2004). Analyses of metallurgical behavior of Al–SiCp composites after high strain rate impacts. *Composite Structures* **64**, 219-226.

Karamis, M.B. (2006). An Evaluation of the Macro Damage on Metal Matrix Composites after High Velocity Impact. *Journal of Composite Materials.* 1-10.

Lee, W.M. and Zikry, M.A. (2010). Microstructural Characterization of a High- Strength Aluminium Alloy Subjected to High Strain- Rate Impact. Metallurgical and Materials Transactions A.

Li, Y. and Ramesh, K.T. (1998). Influence of Particle Volume Fraction, Shape, and Aspect Ratio on the Behavior of Particle-Reinforced Metal-Matrix Composites at high Rates of Strain. *Acta Mater* **46**. 5633-5646.

Li, Y., Ramesh, K.T. and Chin, E.S.C. (2007). Plastic Deformation and Failure in A359 Aluminium and an A359-SiCp MMC under Quasistatic and High-Strain-Rate Tension. *Journal of Composite Materials* **41**. 27-40.

Li, Y., Ramesh, K.T. and Chin, E.S.C. (2000). Viscoplastic Deformation and Compressive Damage in an A359/SiCp Metal Matrix Composite. *Acta Mater* **48**. 1563-1573.

Li, Y., Ramesh, K.T. and Chin, E.S.C. (2000). The Compressive Viscoplastic Response of an A359/SiCp Metal-Matrix Composite and of the A359 Aluminium Alloy Matrix. *International Journal of Solids and Structures* **37**. 7547-7562.

Lin, T., Yang, Q., Tan, C., Liu, B., and McDonald, A. (2008). Processing and ballistic performance of lightweight armors based on ultra-fine-grain aluminum composites. *J Mater Sci* ,7344–7348.

Myriounis, D. P., Hasan, S. T., and Matikas, T. E. (2008). Microdeformation behavior of Al-SiC metal matrix composites. *Composite Interfaces* **15**, 49-514.

Myriounis, D. P., Hasan, S. T., and Matikas, T. E. (2008). Influence Of Processing Conditions On The Micro-Mechanical Properties Of Particulate-Reinforced Aluminium Matrix Composites. *Advanced Composites Letters* **17**,75-85.

Myriounis, D. P., Hasan, S. T., Barkoula, N. M., Paipetis, A and Matikas, T. E. (2009). Effects of Heat Treatment on Microstructure and the Fracture Toughness of SiCp/Al Alloy Metal Matrix Composites. *Journal of Advance Materials* **3.** 1-25.

Nieh, T.G. and Karlak, R.F. (1983). Hot-Rolled Silicon Carbide- Aluminium Composites. Journal of Materials Science Letters **2 .** 119-122.

Ogris, E., Wahlen, A., Luchinger, H., and Uggowitzer, P.J. (2002). On the silicon spheroidization in Al–Si alloys. Journal of Light Metals 2, 263–269.

Perez, J.E., Yawny, A., and Gonzales, C. (2003). On the Applicability of Elastic- Plastic Fracture Mechanics to Discontinuously Reinforced Aluminium Composites. *Journal of Composite Materials* **37**. 2001-2010.

Rabiei, A., Vendra, L. and Kishi, T. (2007). Fracture Behavior of Particle Reinforced Metal Matrix Composites. *Composites Part A: Applied Science and Manufacturing* **39**. 294-300.

Rayleigh, Lord. (1978). On the instability of Jets. *Proc. Lond. math. Soc,* 4-12.

Samuel F. H.and Samuel A. M. (1993). Effect of heat treatment on the microstructure, tensile properties, and fracture behavior of permanent mold Al-10 wt pct Si-0.6 wt pct Mg/SiC/10p composite castings, *Metallurgical and Materials Transactions A* **25**, 2247-2263.

Sritharan, T., Chan ,L.S., Tan, L.K., and Hung, N.P. (2001). A Feature of the Reaction Between Al and SiC particles in an MMC. *Materials Characterization* **47**. 75-77.

Stuwe, H.P. and Kolednik. O. (1988). Shape Instability of Thin Cylinders. *Acta Metall.* **36,** 1705-1708.

Surappa, M K. (2003). Aluminium Matrix Composites: Challenges and Opportunities. *Sadhana* **28**, 319–334.

Swindlehurts, S. J. and Hall, I.W. Thermal Treatment Effects in SiC/Al Metal Matrix Composites. (1994). *Journal of Materials Science* **29.** 1075-1082.

Taha, M.A., El-Mahallawy, N.A and El-Sabbagh, A. M. (2003). Behavior of Stir-Cast Al-Alloy Particulate-Reinforced Metal-Matrix Composites under Successive Hot Rolling. *Advanced Engineering Materials* **5**, 805-812.

Tanaka, M., Ono, S., and Tsuneno, M. (1986). Factors Contributing to Crushing of Voids during Forging. *Journal of JSTP* **27,** 927-934.

Tekmen, C., Ozdemir, I., Cocen, U., and Onel, K. (2003). The mechanical response of Al-Si -Mg/SiCp composite: influence of porosity. *Materials Science and Engineering* **A360,** 365-371.

Wang, A., Thomson, P.F., and Hodgson, P.D. (1996). A study of pore closure and welding in hot rolling process. *Journal of Materials Processing Technology* **60,** 95-102.

Wang, N.,Wang Z., Weatherly.,G. (1991). Formation of Magnesium Aluminate (Spinel) in Cast SiC Particulate-Reinforced Al(A356) Metal Matrix Composites. *Metallurgical Transactions A* **23A.** 1423-1430.

Warmuzek , M. (2004). Aluminum-Silicon Casting Alloys: Atlas of Microfractographs. *ASM International,* 1-8.

Werner, E. (1990). Thermal Shape Instabilities of Lamellar Structures. *Z. Metallkunde* **81**, 790-798.

Zhou, W. and Xu, Z.M. (1997). Casting of SiC Reinforced Metal Matrix Composites. *Journal of Materials Processing Technology* **63.** 358-363.